BRNO UNIVERSITY OF TECHNOLOGY
VYSOKÉ UČENÍ TECHNICKÉ V BRNĚ

CENTRAL EUROPEAN INSTITUTE OF TECHNOLOGY BUT
STŘEDOEVROPSKÝ TECHNOLOGICKÝ INSTITUT VUT

MAGNETO OPTICAL STUDIES OF SOLID STATES MATERIALS
MAGNETO-OPTICKÉ STUDIE PEVNÝCH LÁTEK

DOCTORAL THESIS - EXTENDED VERSION
DIZERTAČNÍ PRÁCE - ROZŠÍŘENÁ VERZE

AUTHOR — MSc. Artur Solodovnyk
AUTOR PRÁCE

SUPERVISOR — doc. Dr. Ing. Petr Neugebauer
ŠKOLITEL

CO-SUPERVISOR — Dr. Oleksii Laguta
ŠKOLITEL SPECIALISTA

BRNO 2022

Abstract
Electrically detected magnetic resonance (EDMR) is a sensitive and powerful technique for the determination of fundamental intrinsic properties of semiconductive solid-state materials. This work describes the fundamental theory of electron paramagnetic resonance and EDMR spectroscopy, in particular, several models of spin-dependent recombination are reviewed. The instrumental and software parts are presented, as well as the development of a new sample holder specific for EDMR. We intend to bring EDMR investigations to a new level, by developing a setup, which will operate at frequencies up to 1.1 THz and external magnetic field up to 16 T. Taking into account the possibilities of a home-built THz Frequency-Domain Rapid Scan (THz FraScan) spectrometer located in CEITEC BUT, samples will be characterized using both magnetic field and frequency sweeps. Thus, compared to the conventional continuous wave (CW) EDMR, this will allow obtaining not only the dependence of the voltage change on the external magnetic field at a given microwave frequency but also measuring frequency-field maps.

Abstrakt
Elektricky detekovaná magnetická resonance (EDMR) je citlivá a užitečná technika pro výzkum základních vlastností polovodičů a pevných látek. Tato práce popisuje teorii elektronové paramagnetické resonance a spektroskopie EDMR v jejímž rámci je nastíněno několik modelů spinově závislé rekombinace. Instrumentační a softwarové části jsou představeny spolu s vývojem nového držáku vzorku přímo pro EDMR. Plánujeme pozvednout výzkum na poli EDMR na vyšší úroveň pomocí vývoje zařízení, které bude pracovat při frekvencích až do 1.1 THz a externím magnetickém poli do 16 T. Vezmeme-li v potaz možnosti námi postaveného THz Frequency-Domain Rapid Scan (THz FraScan) spektrometru nacházejícího se na CEITEC VUT, vzorky budeme charakterizovat pomocí obou měřicích módu, tedy zvyšování magnetického pole nebo frekvence. V porovnání s konvenční kontinuální vlnou (CW) EDMR nám tato měření umožní získat nejen závislost změny napětí na externím magnetické poli při dané frekvenci, ale také akvizici map znázorňující závislost frekvence na magnetickém poli.

Keywords
Electron paramagnetic resonance, electrically detected magnetic resonance, spectroscopy, THz, SiC

Klíčová slova
Elektronová paramagnetická rezonance, elektricky detekovaná magnetická rezonance, spektroskopie, THz, SiC

SOLODOVNYK, Artur. *Magneto Optical Studies of Solid States Materials*. Brno, 2022. 95 p. Doctoral thesis - extended version. Brno University of Technology. Central European Institute of Technology BUT. Supervisor: Petr NEUGEBAUER.

I hereby declare that I have written my doctoral thesis topic on the theme of *Magneto Optical Studies of Solid States Materials* independently, under the guidance of the thesis supervisor, doc. Dr. Ing. Petr Neugebauer, and using literature and other sources of information which are all properly quoted in the thesis and detailed in the list of literature at the end of the thesis.

MSc. Artur Solodovnyk

I would like to thank my family for their unconditional support during my PhD studies, as well as my friends for being there when I needed it the most. Next, I would like to thank Prof. Patrick Lenahan's entire research group, particularly himself, Dr. Fedor Sharov, Dr. Elias Frantz, Dr. Steve Moxim, and Dr. Kenneth Myers, for fruitful scientific conversation during thesis preparation. I would also like to thank Dr. Boris Naydenov for all his support and Michele Segantini for reference EDMR measurements. Furthermore, I am grateful to all members of the CEITEC MOTeS research group, particularly my supervisor, Dr. Ing. Petr Neugebauer, my friend and co-supervisor, Dr. Oleksii Laguta, for answering on any of my questions and putting up with me during my studies, and Dr. Vinicius Santana for theoretical discussions. Finally, I would want to express my gratitude to DrSc. Dariya Savchenko for providing the samples used in this thesis, as well as great assistance with EDMR theory and general magnetic resonance theory consulting. The work was supported by the European Research Council (ERC) through the European Union's Horizon 2020 Research and Innovation Program under Grant 714850, and by Internal Grant Agency, CEITEC VUT-J-19-6070, Czech Republic. Also, CzechNanoLab project LM2018110 funded by MEYS CR is gratefully acknowledged for the financial support of the samples preparation at CEITEC Nano Research Infrastructure.

MSc. Artur Solodovnyk

Contents

1. Introduction **1**

2. Aims of thesis **9**

3. Theoretical background **11**
3.1. Electron Paramagnetic Resonance . . . 11
3.1.1. Fundamentals . . . 11
3.1.2. Magnetic resonance phenomenon . . . 14
3.1.3. Hyperfine structure . . . 17
3.1.4. g-factor anisotropy . . . 19
3.2. Electrically Detected Magnetic Resonance (EDMR) . . . 23
3.2.1. Fundamentals . . . 23
3.2.2. The Lepine Model . . . 24
3.2.3. The model of Kaplan, Solomon and Mott . . . 25
3.2.4. The Shockley-Read-Hall Model . . . 26
3.2.5. Other EDMR Models . . . 27
3.3. Summary . . . 30

4. Instrumentation **31**
4.1. Review . . . 31
4.2. Summary . . . 38

5. THz EDMR Setup **41**
5.1. General overview of THz FraScan Spectrometer . . . 41
5.2. Experimental Setup . . . 43
5.3. THz EDMR Sample Holder . . . 45
5.3.1. Sample preparation . . . 47
5.3.2. Light beam alignment determination . . . 48
5.3.3. Microwave losses . . . 50
5.3.4. Homebuilt optical fiber feedthrough . . . 51
5.4. EDMR Experiment . . . 52
5.5. Summary . . . 53

6. Results obtained **57**
6.1. Silicon Carbide . . . 57
6.2. Multifrequency EDMR studies on 15R SiC . . . 59
6.3. Summary . . . 66

7. Conclusions **69**

8. References **73**

9. Author publications and outputs **87**

List of abbreviations **89**

Appendices **93**

1. Introduction

We cannot imagine our lives without electronic devices in the present day. Everything that surrounds us is merely the result of generations of technological advancement. Since Hertz experimentally confirmed the possibility of transmitting electromagnetic waves through the air, confirming Maxwell's theory of electromagnetism [1], there has been a 'base' for the development of what we now refer to as radio [2]. Concerning the impact of development, television [3], radar [4], mobile communications [5], Wi-Fi [6], etc. follow the invention of radio broadcasting [Fig. 1.1]. Since the establishment of the term 'electron' [7] and the invention of the first vacuum tube [8], a new branch of physics known as 'electronics' has emerged to study the emission of electrons, their behavior, and their effects. Since the invention of the transistor in the 1940s [9], solid-state electronics have nearly overtaken 'vacuum electronics' as the dominant form of electronics [10]. The volume of transistors was decreased, resulting in the creation of integrated circuit models, replacing the enormous, initially 'first generation' vacuum tube computers with printed circuit boards [11]. To date, the smallest transistor has been created based on silicon nanotubes and molybdenum disulfide, where the gate length is only 1 nm [12].

The study of defects and impurities is an important aspect of solid state physics. Doping one material with another allows to change its properties such as color, mechanical, electrical, optical, and others characteristics [15, 16]. Thus, scientists have been able to improve solid state materials over time by changing their properties to produce more advanced devices and changing their composition to improve performance in a specific area of their application. In solar cells, for instance, the most important parameter is the energy conversion factor, which depends on the device's total current management [17]. In the simplest case, a Si-based p-i-n solar cell with an a-Si:H layer in between μc-Si:H p-type and n-type layers functions as a 'charge carrier relaxation relay' [18]. Due to its abundance of dangling bond defects, the a-Si:H layer 'controls' the recombination rate, so the charge carrier does not relax to the lower energy level instantly, but rather by utilizing 'defect islands' in the bandgap. In this situation, the control and oversight of the defects in a-Si:H layer play a crucial role, with the outcome dependent on the device's overall current management.

Some defects may be introduced on intent, while others may result from a poorly prepared growth process or accidental material contamination. *Crystallographic defect* is any stable interruption of the translational periodicity of the crystal lattice [Fig. 1.2]. Defects can be classified as planar, bulk, linear, or point, depending on their multidimensionality

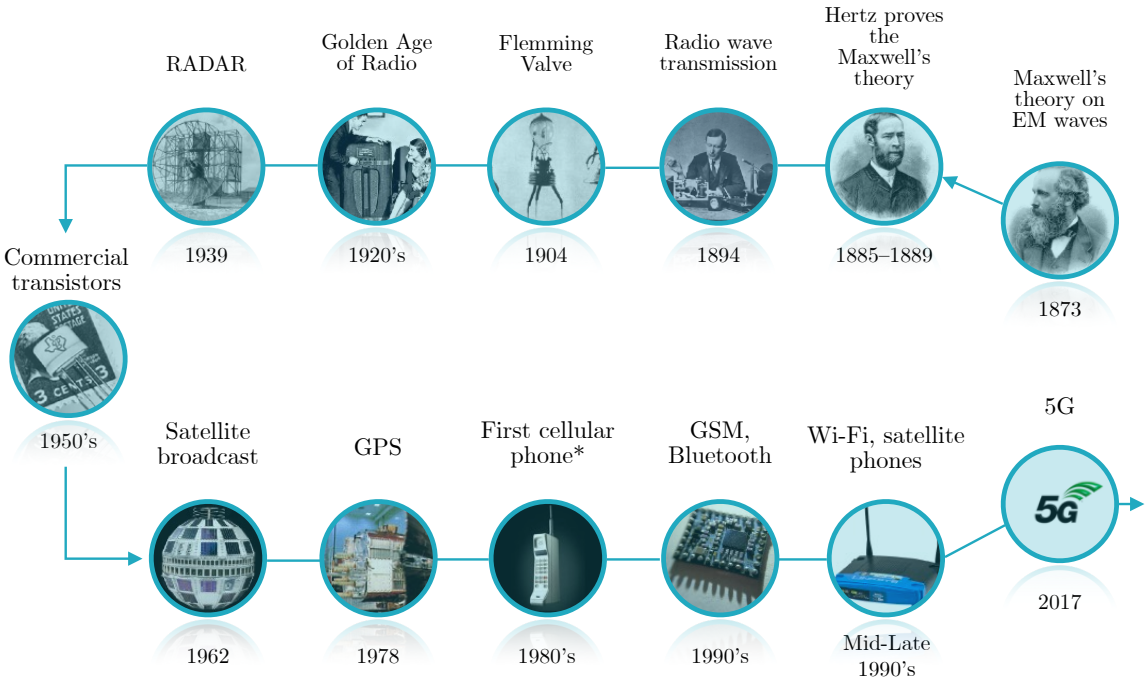

Figure 1.1: The timeline of the development of electromagnetic waves progress from Maxwell's theory on electromagnetic (EM) waves [1] to the 5G standard for broadband cellular networks [13]. (*) - First cellular phone which is commercially available.

[19] (per the number of dimensions in which the defect dimensions exceed the interatomic distance by a significant margin). On one hand, the presence of these defects can dramatically alter the properties of a device, enhancing its performance, while on the other hand, it can lead to its disintegration. Determining the amount of defects after the sample has been prepared or the cause from which the defects originated is, therefore, essential knowledge. Additionally, it should be noted that as the area of active devices continues to shrink, the number of defects in this area is also decreasing. There are numerous techniques and research methods for determining defects and electrical properties of semiconductors, but few of them are able to deal with such minute quantities of defects on the atomic scale as the electrically detected magnetic resonance (EDMR).

The EDMR is a powerful and effective spectroscopic technique for investigating the atomic-level characterization of charge carriers, defect structures, and impurities in semiconductive solid state materials. One of the earliest implementations of this technique dates back to 1966, when Schmidt and Solomon described spin-dependent recombination of free carriers in phosphorus-doped silicon [20]. Electron paramagnetic resonance (EPR), a well-known non-invasive method for determining the structures of defects, serves as the foundation for this technique. EPR is a widely-used, powerful technique with numerous applications in physics, chemistry, biology, medicine, and other fields. The most influential applications of EPR are the identification of free radicals in gaseous, liquid, and solid state materials [21]; the research of proteins using spin labels [22]; the determination of food quality [23–25]; the characterization of materials in geology and archeology [26,

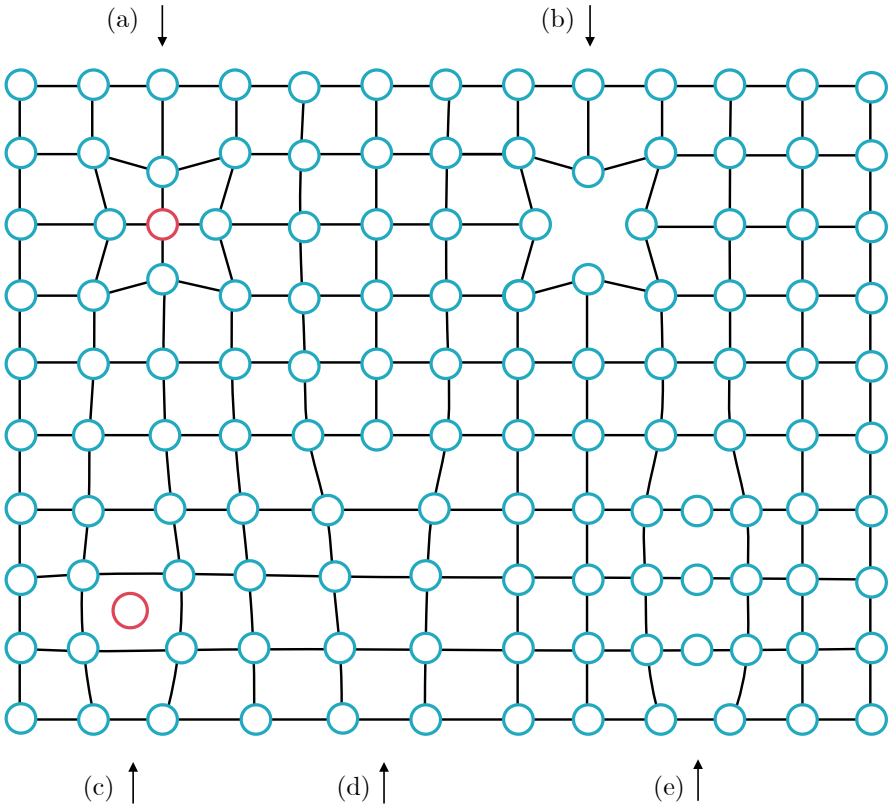

Figure 1.2: Various types of crystal defects are depicted in a primitive cubic lattice. (a) – substitutional impurity atom (red), (b) – vacancy, (c) – interstitial impurity atom, (d) – edge dislocation, (e) – interstitial type dislocation loop. Partially adapted from [14].

27]; and the study of qubits in the quantum computing field [28–30], among others. The essential distinction between EPR and EDMR stands in the detection scheme. In EPR, the spectrum is obtained as a result of the sample's microwave absorption under resonance conditions; in EDMR, the spectrum is acquired under the resonance same conditions, but as a result of a change in the sample's current or voltage. This enables the investigation of the behavior of the current in certain semiconductive devices[1] under the resonance conditions in order to study the essential spin-dependent mechanisms. In comparision, EPR is insensitive to these processes, whereas EDMR can investigate these transport mechanisms, considering that they are based on spin selection rules. The importance of point defects and impurities in semiconductive devices, the concentration of which is decreasing in modern devices, is the motivation for employing detection of electrical conductivity rather than microwave absorption. The important part here is the spin sensitivity. EDMR is 10^7 times more sensitive than EPR [31]. While in EPR the minimum requirement for the defect amount is 10^{11} [32], in EDMR in can be even down to 1000 [31], or even, in some cases, to a single electron [33]. Among the numerous EDMR research applications, we can highlight:

[1] which possess a system with unpaired electrons

- solar cells research [18, 34, 35];
- MOSFET, nano-scale transistors, device reliability research (irradiation damage, high electric field stressing) [36–40];
- quantum computing, electronic spin storage, write / readout [33, 41–43];
- organic LEDs [44, 45].

Therefore, taking into account the described above regarding this spectroscopic technique, research in the field of detecting defects and impurities in the nanoscale is of great importance in the development of nowadays electronics and directly contributes to the improvement of the electrical and magneto-optical characteristics of the materials and devices under study.

To summarize the studied phenomena at various frequencies and length scales, we can refer to Fig. 1.3, upper part of which depicts the *electromagnetic spectrum*. It also shows physical phenomena being studied in addition to magnetic resonance applications, from the longest radio waves to gamma-rays electromagnetic region [46]. Well-known spectroscopic techniques, such as NMR and MRI, operate in the region of short radio waves ($\nu \leq 800\,\mathrm{MHz}$), whereas EPR and EDMR operate in the region of microwaves ($\nu = = 10-1100\,\mathrm{GHz}$ and $\nu \leq 500\,\mathrm{MHz}$). Note that the magnetic resonance application regions for some techniques are given for common, widely used applications.

As depicted in Fig. 1.3, the specialized frequency ranges of EDMR are essentially equal to those of EPR despite the low-frequency range solutions. Matching EPR and EDMR frequencies can be explained by the fact that the majority of EDMR research is undertaken with EPR spectrometers modified for EDMR detection. As indicated previously, the EDMR is directly dependent on EPR, but the detection approach is distinct. With the development of homemade solutions, in contrast to commercially standardized ones (X-, Q-, and W-band spectrometers), it became possible to push the boundaries of different research areas [47]. For instance, the frequency sweep option is not available in any commercial EPR solution, and the deployment of this method (where the magnetic field remains constant and the frequency is swept) opens up new paths for magnetic resonance study. Perhaps, rapid scan EPR is the most suitable example here. It is a quasi continuous wave mode technique that partially covers the pulse-based method. At the present state, rapid scan EPR is able to determine the spin-spin relaxation time T_2 [48, 49]. Pulse mode spectrometers use a different approach than continuous wave (CW) spectrometers, and the pricing can be significantly higher due to the use of more complicated electronics [50]. The benefits of frequency scanning are not exclusive to rapid scan EPR alone. For instance, the frequency domain (FD) measurement mode provides the acquisition of the zero-field splitting (ZFS). In the combination of fast FD and slow magnetic domain (MD), we can acquire the frequency-field map [51] as shown in Fig. 1.4. These maps can be used to track a frequency-dependent sample behavior, uniquely define the spin Hamiltonian

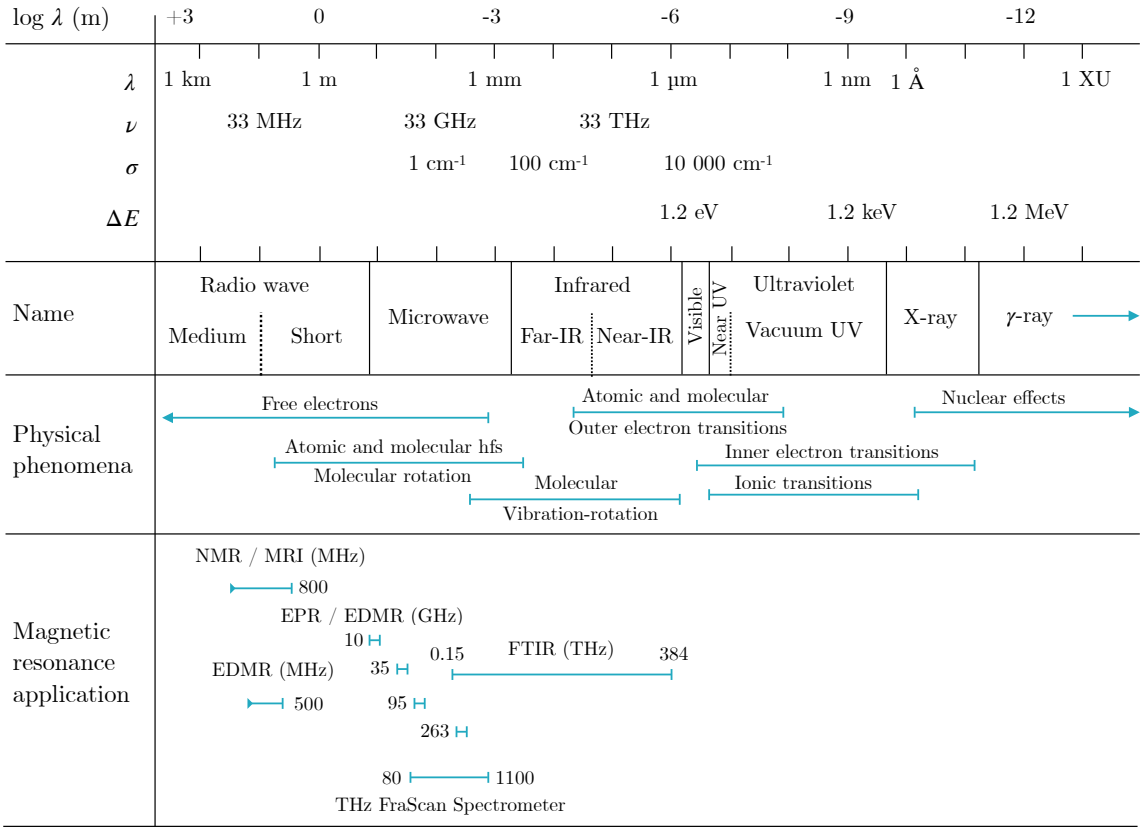

Figure 1.3: The electromagnetic spectrum. It incorporates the longest radio waves ($\lambda > 1\,\mathrm{km}$), medium and short radio waves ($\lambda > 1\,\mathrm{m}$), microwaves ($\lambda \sim 1\,\mathrm{mm} - 1\,\mathrm{m}$), the infrared region ($\lambda \sim 750\,\mathrm{nm} - 1\,\mathrm{mm}$), the visible spectrum ($\lambda \sim 400 - 750\,\mathrm{nm}$), ultraviolet ($\lambda \sim 10\,\mathrm{nm} - 400\,\mathrm{nm}$) as well as x-rays ($\lambda \sim 0.01\,\mathrm{nm} - 10\,\mathrm{nm}$), and gamma rays ($\lambda < 0.01\,\mathrm{nm}$). The wavelength ($\lambda$) is written in meters (and sub-units: angstrom (Å) and X-units, where $1\,\mathrm{XU} = 10^{-3}\,\text{Å}$), the frequency ($\nu$) is written in Hz, the wavenumber (σ) is written in reversed centimeters (cm^{-1}), and the energy difference between two stationary states ($\Delta E = h\nu$, where h is Planck's constant), is written in eV [46]. The THz FraScan spectrometer is located in CEITEC Brno University of Technology (Czech Republic) [see chapter 5].

parameters [52], or qualitatively visualize the recorded data in the designated frequency-field range. As depicted in Fig. 1.3, the frequency range of the THz FraScan spectrometer is significantly greater than the frequency range of the majority of dedicated EPR bands combined, and it covers the sweepable frequencies from 80 GHz to 1.1 THz with a magnetic field of 0–16 T. The urge to perform magnetic resonance research at higher frequencies and magnetic fields is manifold. The acquisition of higher spin polarization, higher g-factor resolution, larger zero-field splitting, and other benefits, including more precise and high-resolution data became possible [18, 51–53]. As stated previously, in general, EDMR is 10^7 times more sensitive than EPR and can analyze spin-dependent processes as hopping, tunneling, charge-pumping, etc., for which EPR is insensitive. The majority

of this field's research has relied on commercial EPR spectrometers, which have significant limits regarding the sample size, metallic sample connections (cavity tuning issues), and other drawbacks. Thus, we have the capability to build an EDMR setup based on the parameters of the THz FraScan spectrometer and advance EDMR research.

This dissertation describes the effective implementation of the EDMR approach in the THz FraScan spectrometer, as well as the proof-of-concept results obtained on highly N-doped 15R SiC monocrystals, and also the first frequency-field EDMR map acquired.

The first chapter named 'Theoretical background' (3) describes the fundamental principles of magnetic resonance phenomena as well as the magnetic moment of an electron and its interaction with an external magnetic field and microwaves, in addition to electron paramagnetic resonance and electrically detected magnetic resonance. A brief overview of a few models that are essential for determining the origin of the spin-dependent mechanism is provided.

The 'Instrumentation' chapter (4) provides an introduction to EDMR instrumentation, an explanation of the EDMR measurement principle, an analysis of existing EDMR solutions, and a comparison of the parameters of existing EDMR research instrumentation. Identifying the limitations of existing EDMR configurations based on sample size and frequency range expansion.

The 'THz EDMR Setup' chapter (5) describes the THz FraScan setup in general and provides a detailed description of the development of the THz EDMR setup based on the THz FraScan spectrometer as a first objective of the thesis, as well as the fabrication of the THz EDMR sample holder, detection scheme, and additional solutions required to conduct the EDMR experiment. Advantages and limitations of such homebuilt setups are highlighted and discussed.

The 'Results obtained' chapter (6) describes the results acquired using the EDMR setup as a proof-of-concept measurements utilizing every possible at that moment approaches to expand the EDMR research in general as a second objective of the thesis. The multifrequency measurements were done on highly nitrogen-doped 15R polytype SiC monocrystal, which revealed the EPR and EDMR single line at $< 15\,\mathrm{K}$ due to nitrogen donors exchange interactions. The ability to perform the frequency domain EDMR is presented and demonstrated the first frequency-field EDMR map.

The last chapter 'Conclusions' (7) presents the summary of the thesis, including a detailed description of the fulfilled tasks and projects as well as an outlook for the future development of the THz EDMR setup.

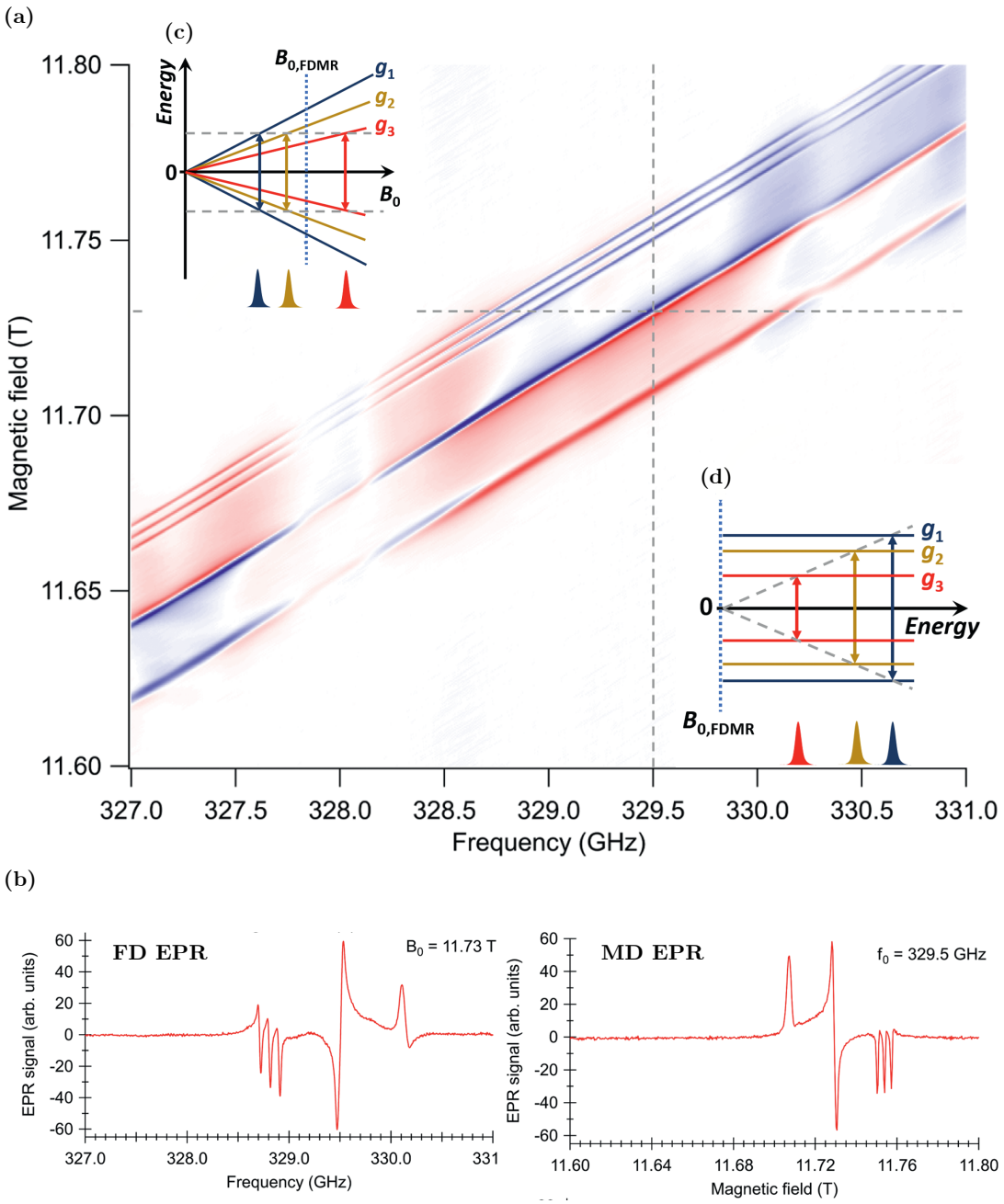

Figure 1.4: (a) – the frequency-field EPR map of ^{14}N-TEMPOL ($S = \frac{1}{2}, I_N = 1$) dissolved in polystyrene, with an outcome of 2.5 mg film with $\approx 10^{16}$ spins. The resolution of the map is 10 000 (frequency) x 1 000 (magnetic field) points. (b) – The extracted data of a frequency (FD EPR) and magnetic field sweep (MD EPR) point indicated via dashed line in (a). (c) – Illustration of the MD EPR and (d) – FD EPR experiments at fixed frequency (MD) and fixed magnetic field (FD) respectively. Taken from [52].

2. Aims of thesis

In this doctoral thesis, the outcomes of two main deliverables are presented:

- A. To implement the EDMR technique in the THz FraScan Spectrometer by developing the specific sample holder, creating the circuitry for EDMR detection, and adjusting the software for the signal acquisition.
- B. To perform the multifrequency investigation on a test sample in order to create a proof-of-concept of a functioning THz EDMR setup making use of nearly all possible capabilities of the system.

The first deliverable required research towards the instrumentation of both commercial EPR/EDMR solutions and custom-built systems, as well as understanding the EDMR detection, comparing its capabilities to those of the existing setup, and preparing for its implementation within our newly built THz FraScan spectrometer. The development of a specific sample holder was required to overcome the issues of sample contact, sample illumination, magnetic field modulation, and proper m.w. propagation, as well as the problems associated with this process (such as optical fiber feedthrough, printed circuit boards, shielded signal extension boxes, etc.).

For the second goal, the entire EDMR system must be calibrated. It requires measurements of m.w. losses, light beam alignment calibration, cryogenic temperature withstand of materials used in development and experiments, and EDMR signal amplification and acquisition, among others.

As the initial sample for the complex EDMR measurements in our system, a highly N-doped ($(N_D - N_A) \approx 5 \cdot 10^{18}\,\mathrm{cm}^{-3}$) 15R polytype SiC monocrystal was used. The following measurements of this sample were conducted in parallel and perpendicular (to the c-axis) orientations: frequency dependence (85 – 120 GHz, 328 GHz); temperature dependence (7.5 K – 12 K); m.w. power dependence (5 – 125 mW); light dependence (403 – 636.7 nm diode lasers); acquisition of the frequency domain EDMR (102 – 104 GHz at 3.5768 T); and recording of the first frequency-field EDMR map (on frequency of 100.2 – 102 GHz; magnetic field of 3.58 – 3.65 T; at the 7.5 K).

3. Theoretical background

This chapter offers a concise theoretical introduction to the fundamentals of magnetic resonance and describes multiple models of EDMR. This chapter's material was adapted in accordance with the material from [32, 54–56].

3.1. Electron Paramagnetic Resonance

In general, the *magnetic resonance* is a phenomenon of resonant absorption of the energy of oscillating electromagnetic field by a system that has a non-zero magnetic moment. If a magnetic field is applied to such a system, then the magnetic moment will precess about the field with a certain angular velocity absorbing the electromagnetic waves with the same frequency. When the magnetic moment is created by protons and neutrons in a nucleus, the resonance absorption is called nuclear magnetic resonance (NMR) [57], and if by the electrons - the electron paramagnetic resonance (EPR) [54]. It was discovered in 1944 by E. Zavoisky [58] and it has become popular spectroscopy technique nowadays. EPR is a widely-used, powerful technique with numerous applications in physics, chemistry, biology, medicine, and other fields [59–62].

3.1.1. Fundamentals

The basis of magnetism is found in electron orbital and spin motions, as well as how electrons interact with one another [63, 64]. The best method to explain the several types of magnetism is to refer to Fig. 3.1. The primary distinction is that some materials have no group interaction of atomic magnetic moments, whereas others have a very strong interaction between atomic moments. Ferromagnetism (a) can occur only when atoms are organized in a lattice and their magnetic moments interact to align parallel to each other. Antiferromagnetic (b) materials are very similar to ferromagnetic materials, but the exchange contact between neighboring atoms causes anti-parallel alignment of the atomic magnetic moments. Within ferrimagnetic (c) materials, exchange interactions cause atoms to align parallel in some crystal sites and anti-parallel in others. When there is no applied field, the atoms in a diamagnetic (e) substance have no net magnetic moment. EPR is dealing with paramagnetic materials (c) in which magnetic moments are randomly oriented. A substance can be called *paramagnetic* if it does not have a macroscopic resultant magnetic moment, but acquires one in an external magnetic field B [Fig. 3.2]. There is a class

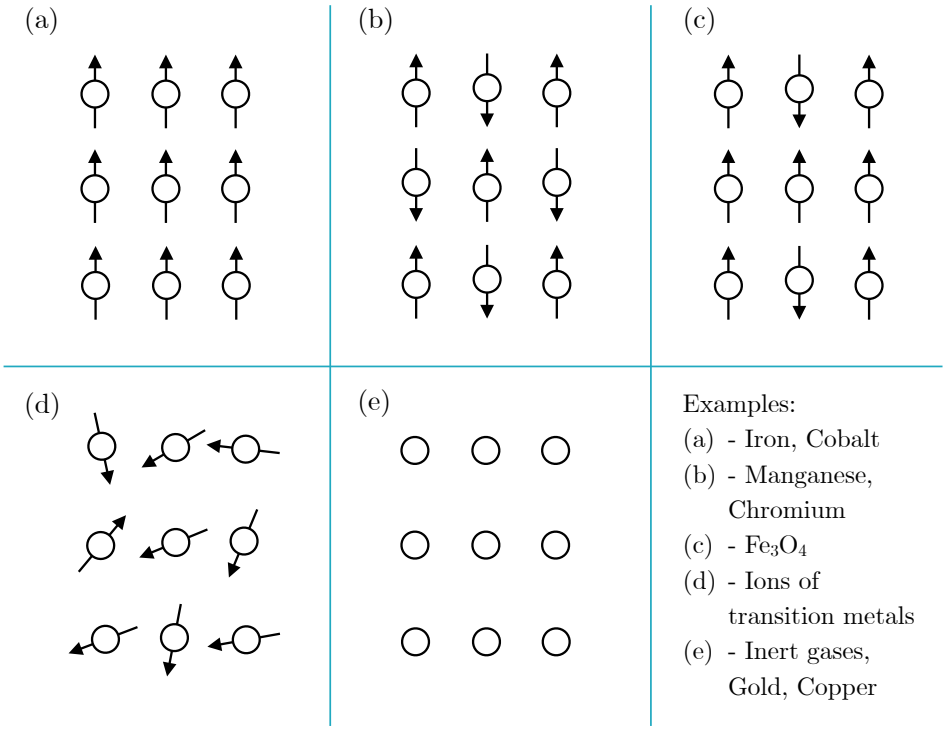

Figure 3.1: The behavior of the magnetic moments of the electron in different materials. The alignment of (a) represents ferromagnetism, where the substance's magnetic moments are aligned in parallel. The orientation of (b) exhibits antiferromagnetism with antiparallel magnetic moments. (c) represents ferrimagnetism, where magnetic moment alignment is both parallel and antiparallel. Case (d) represents paramagnetism, in which the orientation of magnetic moments is random. The final (c) indicates diamagnetism, which occurs when a substance has no magnetic moment.

of paramagnetic substances, whose atoms or ions have permanent magnetic moments of electronic origin.

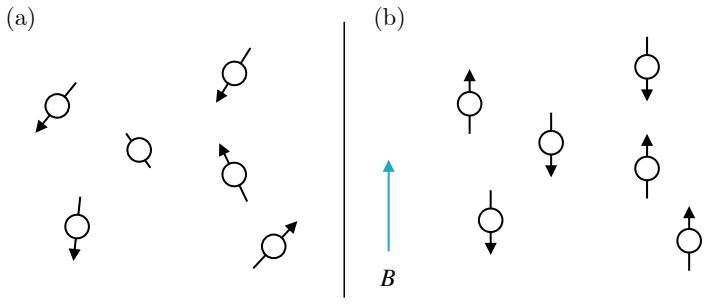

Figure 3.2: The alignment of the magnetic moments of the electron in the absence (a) and presence (b) of an external magnetic field B.

When the external field is absent, their magnetic dipoles are arranged randomly. However, a magnetic field can distribute their orientation in such a way that a substance can acquire a net magnetic moment. An atom has a permanent magnetic moment $\boldsymbol{\mu}$, only

possessing a resultant angular moment $\boldsymbol{L}$. These two quantities are connected by the formula:

$$\boldsymbol{\mu} = \gamma \boldsymbol{L}, \tag{3.1}$$

where γ is the gyromagnetic ratio and $\boldsymbol{L}$ is the angular momentum (an integral or the half-integral multiple of $h/2\pi = \hbar$, where h is Plank's constant). The equation of motion for a dipole on which acts a magnetic field $\boldsymbol{B}$ can be written as:

$$\frac{d\boldsymbol{L}}{dt} = \boldsymbol{\mu} \times \boldsymbol{B}. \tag{3.2}$$

If the magnetic field $\boldsymbol{B}$ is directed along the z axis of the Cartesian coordinate system, then the solution of this equation can be written as:

$$L_x = L \sin\alpha \cos(\omega_L t + \varepsilon), \tag{3.3a}$$

$$L_y = L \sin\alpha \sin(\omega_L t + \varepsilon), \tag{3.3b}$$

$$L_z = L \cos\alpha. \tag{3.3c}$$

where α defines an angle between $\boldsymbol{L}$ and $\boldsymbol{B}$, ε is a phase, ω_L is the Larmor frequency (3.4).

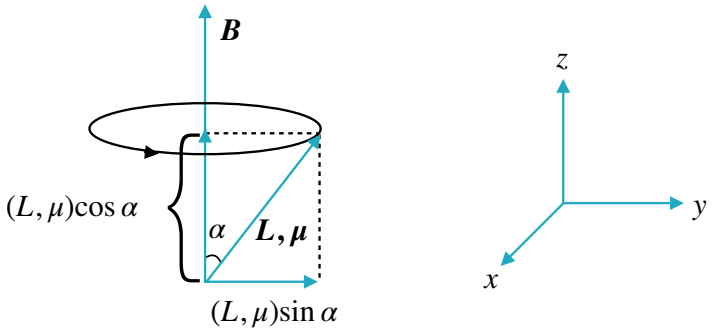

Figure 3.3: Precession of the magnetic moment $\boldsymbol{\mu}$ or angular momentum $\boldsymbol{L}$ around the external magnetic field $\boldsymbol{B}$

Similar solutions can be obtained for the vector component $\boldsymbol{\mu}$. The motion of the vectors $\boldsymbol{L}$ and $\boldsymbol{\mu}$ is a uniform precession in the field $\boldsymbol{B}$ with an angular velocity

$$\omega_L = -\gamma \boldsymbol{B}. \tag{3.4}$$

The minus sign in this case says that the precession occurs in the direction of the left screw moving along $\boldsymbol{B}$, if the value γ is positive, and in the opposite direction, if γ is negative. The components of $\boldsymbol{L}$ and $\boldsymbol{\mu}$ along the magnetic field $\boldsymbol{B}$ are constant in magnitude, so the dipole energy (Zeeman energy)

$$W = -\boldsymbol{\mu} \cdot \boldsymbol{B} \tag{3.5}$$

is an integral of motion.

If the electronic structure of a free atom or ion has a resultant angular moment, it will have a permanent magnetic dipole moment. A gyromagnetic ratio in this case will be:

$$\gamma = -g\frac{e}{2mc}, \tag{3.6}$$

where e and m are charge and mass of electron respectively, c is the speed of light (written in the centimetre–gram–second (CGS) system). Value g is a number of the order of unity, the value of which depends on the relative contributions of the orbital and spin moments to the total angular momentum. For most experiments $g \simeq 2$.

3.1.2. Magnetic resonance phenomenon

We considered that a magnetic dipole $\boldsymbol{\mu} = \gamma \boldsymbol{L}$ (3.1) placed in a magnetic field $\boldsymbol{B}$ precesses around it with an angular velocity $\omega_L = -\gamma \boldsymbol{B}$ (3.4). This precession creates an oscillating magnetic moment in any direction perpendicular to the field $\boldsymbol{B}$, which can interact with an oscillating magnetic field $B_1 \cos \omega t$, also perpendicular to $\boldsymbol{B}$. Interaction affects the motion of the dipole only when the frequency ω is close to the Larmor frequency ω_L. Thus, we are dealing with a *resonant phenomenon*. When the resonance condition $\omega = \omega_L$ is satisfied, component of the dipole $\mu \cos \alpha$, directed along the constant field $\boldsymbol{B}$, can change significantly even under the action of an oscillating field whose amplitude is $B_1 \ll B$. This effect is called *magnetic resonance*.

Corresponding to the equation (3.5) a change in the $\mu \cos \alpha$ component means a change in the energy of the dipole $W = -\mu B \cos \alpha$, which can be rewritten as:

$$W = -\gamma L B \cos \alpha, \tag{3.7}$$

According to quantum mechanics, the stationary values of the component $L \cos \alpha$ of an angular moment are limited to the values of $\hbar M$, $\hbar(M-1)$ ... $-\hbar(M-1)$, $-\hbar M$, where the magnetic quantum number M takes a number of integer or half-integer values. There is a selection rule $\Delta M = \pm 1$ for allowed transitions, and therefore, for their excitation, a radiation with energy

$$\hbar\omega = W_M - W_{M-1} = -\gamma \hbar B, \tag{3.8}$$

or with a frequency

$$\omega = -\gamma B = \omega_L, \tag{3.9}$$

is required. It is simple to determine the numerical value of the resonance frequency. For the electronic dipole in CGS electromagnetic units (e.m.u.) $\gamma = -g(\frac{e}{2m})$, therefore using the value $\frac{e}{m} = 1.758796(17) \cdot 10^7$ e.m.u./g we get:

$$\nu = \nu_L = \frac{g(e/2m)B}{2\pi} = 1.3996 \cdot 10^6 (gB). \tag{3.10}$$

The value of g may thus be simply calculated from field and frequency measurements, since

$$g = 0.71557 \times 10^{-6}(\frac{\nu}{B}), \tag{3.11}$$

where ν is in Hz and B is in G. If the measurements were carried out in the centimeter wave range, the value of g can be expressed in terms of the wavenumber $\tilde{\nu} = \frac{1}{\lambda}(cm^{-1})$ or the wavelength λ (cm) and B (here, in kG):

$$g = 21.4198(\frac{\tilde{\nu}}{B}) = 21.4198(\lambda B)^{-1}. \tag{3.12}$$

In the case of $g = 2$ and $B = 10.7\,\mathrm{kG}$ (in CGS, or $1.07\,\mathrm{T}$ in SI units, further B notation is in T), resonance requires radiation with a wavelength of 1 cm. X-band range ($\nu \approx 10\,\mathrm{GHz}$, $B \approx 357\,\mathrm{mT}$) radiation has a wavelength of approximately 3 cm, and for Q-band ($\nu \approx 40\,\mathrm{GHz}$, $B \approx 1428\,\mathrm{mT}$) range wavelength is around 0.8 cm.

If a free atom possesses both orbital and spin angular magnetic moments, the value of g is determined by the coupling between these moments. In the case of LS-coupling (where $\mathbf{L}$ represents the total orbital moment quantum number, and $\mathbf{S}$ represents the total spin magnetic moment quantum number), the resultant angular momentum can be described by the quantum number $\mathbf{J} = \mathbf{L} + \mathbf{S}$ and the corresponding g value:

$$g_J = \frac{3}{2} - \frac{L(+1) - S(S+1)}{2J(J+1)}. \tag{3.13}$$

For a free atom with an electron dipole moment $\mu_J = -g_J\beta J$, the Hamiltonian of the Zeeman interaction in the field $\boldsymbol{B}$ has the form

$$\hat{\mathcal{H}} = -(\hat{\mu}_J \cdot \boldsymbol{B}) = g_J\beta(\boldsymbol{B} \cdot \hat{J}), \tag{3.14}$$

where $\beta = \frac{e\hbar}{2mc}$ is the Bohr's magneton. The energy of the stationary state characterized by the quantum number M and the corresponding component of the angular momentum $\hbar M$ in the direction of the field B is equal to

$$W_M = g_J\beta BM. \tag{3.15}$$

Thus, for the excitation of transitions allowed by the selection rule $\Delta M = \pm 1$, requires quanta with the energy

$$h\nu = g_J\beta B. \tag{3.16}$$

This simple form of the Zeeman interaction is valid when the level J is $(2J+1)$-times degenerated at $B = 0$, is well separated from other levels, that is, the Zeeman energy $g_J\beta B \ll \Delta$, where Δ is the levels separation [Fig. 3.4].

In electron paramagnetic resonance, we deal with transitions between levels, the distance between which is only a few inverse centimeters. Therefore, only groups of levels that are degenerate in a zero magnetic field are of interest. Consequently, a convenient

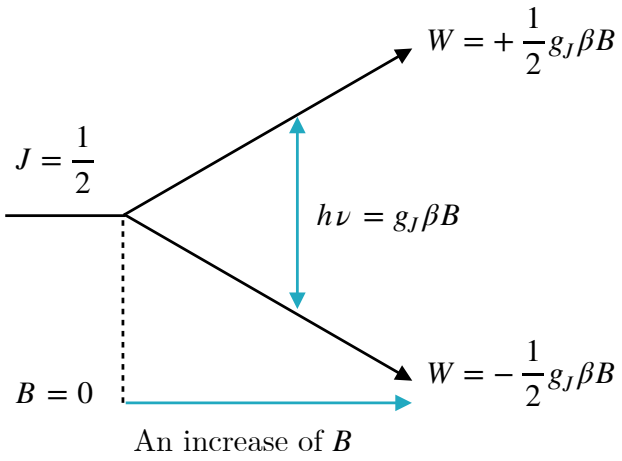

Figure 3.4: Energy levels splitting of a system with $J = \frac{1}{2}$ Zeeman effect in the magnetic field $\boldsymbol{B}$.

method is needed to describe a group of levels when a magnetic field is applied to the system. This method is well developed. It uses the concept of an *effective spin* $\tilde{S}$, which is a fictitious angular momentum, such that the degeneration of the group of interest is equal to $(2\tilde{S} + 1)$.

The spectrum of electron paramagnetic resonance consists of lines caused by different electronic transitions, each of which, in turn, can be divided into a number of lines, e.g. due to interaction with nuclear magnetic moment. Measuring the spectrum at different frequencies and orientations of the magnetic field and crystal fields gives a huge amount of data that does not make much sense until a simple interpretation is found. The solution to this problem is to use a spin Hamiltonian, the form of which can be guessed based on the consideration of the crystal's symmetry, if it cannot be obtained from the theory. According to equation (3.14), we considered the spin Hamiltonian only in term of the Zeeman interaction for a free atom in the field B. The most common form of the spin Hamiltonian contains a large number of terms and can be written as:

$$\hat{\mathcal{H}} = \hat{\mathcal{H}}_{EZ} + \hat{\mathcal{H}}_{FS} + \hat{\mathcal{H}}_{HF} + \hat{\mathcal{H}}_{NZ} + \hat{\mathcal{H}}_{Q}, \tag{3.17}$$

where:

- $\hat{\mathcal{H}}_{EZ} = \beta \boldsymbol{S} \cdot \tilde{g} \cdot \boldsymbol{B}$ - electron Zeeman interaction,
- $\hat{\mathcal{H}}_{FS} = \boldsymbol{S} \cdot \tilde{D} \cdot \boldsymbol{S}$ - fine structure interaction,
- $\hat{\mathcal{H}}_{HF} = \boldsymbol{I} \cdot \tilde{A} \cdot \boldsymbol{S}$ - hyperfine interaction,
- $\hat{\mathcal{H}}_{NZ} = g_n \mu_n \boldsymbol{I} \cdot \boldsymbol{B}$ - nuclear Zeeman interaction,
- $\hat{\mathcal{H}}_{Q} = \boldsymbol{I} \cdot \tilde{Q} \cdot \boldsymbol{I}$ - nuclear quadrupole interaction,

where $\tilde{g}$, $\tilde{D}$ and $\tilde{A}$ are symmetrical tensors in three-dimensional space. They can be transformed into their principal axes systems, and are then diagonal.

For instance, one possible way to write the electronic Zeeman interaction is

$$\beta \boldsymbol{B} \cdot \boldsymbol{g} \cdot \boldsymbol{S} = \beta(g_{xx}B_xS_x + g_{yy}B_yS_y + g_{xy}B_xS_y + g_{yx}B_yS_x + g_{yz}B_yS_z + g_{zx}B_zS_x + g_{xz}B_xS_z), \tag{3.18}$$

however if we decide for a system in which the (x, y, and z) axes serve as the primary axes, this simplifies to the following form:

$$\beta(g_xB_xS_x + g_yB_yS_y + g_zB_zS_z), \tag{3.19}$$

where the g_{xx} and others can be written in the form of g_x for the brevity.

It is necessary to note that EPR experiments are carried out not only in the centimeter wavelength range. Today the measurements are carried out both in the millimeter and submillimeter wavelengths. Usually, the intensity increases with increasing the frequency. The power absorbed by the spin system during the transition between levels α and β is determined by the formula

$$\frac{dW}{dt} = w_e(h\nu)(n_\alpha - n_\beta), \tag{3.20}$$

where w_e is the rate of electronic transitions per one ion induced by an oscillating field, $h\nu$ is the quantum involved and n_α, n_β are the instantaneous lower and upper state populations. If $h\nu \ll kT$, then the approximate equality $n_\alpha - n_\beta \approx n_\alpha(h\nu/kT)$ is fulfilled and it follows from the equation (3.20) that dW/dt increases in proportion to the square of the frequency, since w_e does not depend on frequency.

3.1.3. Hyperfine structure

An electron moves not only in an external field $\boldsymbol{B}$, but also in local magnetic fields created by atomic nuclei's magnetic moments. As a result, the total energy is directed to:

$$E = g\beta BS - g_I\beta_I BI + aIS. \tag{3.21}$$

The underlying Hamiltonian is

$$\hat{\mathcal{H}} = g\beta B\hat{S} - g_I\beta_I B\hat{I} + a\hat{I}\hat{S}. \tag{3.22}$$

Here, a, $\hat{I}$, $\hat{S}$, g_I, β_I are the isotropic hyperfine coupling constants, the nuclei and an electron spin operator, the nuclei g-factor, and the nuclear magneton. The hyperfine structure (HFS) interaction for resonance field strength is in the 1-10 mT range, whereas the range of resonance field strength of conventional spectrometers in the X-band with a frequency of roughly 9.5 GHz is often much smaller than the Zeeman interaction. As a result,

perturbation theories may be used to account for the splitting of energy levels. Following rules apply in the undistorted case:

$$\hat{\mathcal{H}}^0 = g\beta B_Z \hat{S}_Z - g_I \beta_I B_Z \hat{I}_Z. \tag{3.23}$$

For hyperfine coupling, the operator $\hat{\mathcal{H}}$ is

$$\hat{\mathcal{H}}' = a\hat{S}\hat{I} = (\hat{S}_x\hat{I}_x + \hat{S}_y\hat{I}_y + \hat{S}_z\hat{I}_z). \tag{3.24}$$

The following eigenvalues of energy are given as solutions for the general case:

$$E_{m_s,m_I} = g\beta B_Z m_S - g_I\beta_I B_Z m_I + a m_s m_i, \tag{3.25}$$

where m_S, m_I are the magnetic electron and nuclear spin quantum numbers. For the case of the spin system, $S = \frac{1}{2}$, $I = \frac{1}{2}$, shown in Fig. 3.5, four eigenvalues are obtained:

$$\varepsilon_1 = E_{1/2,-1/2} = \frac{1}{2}g\beta B_Z + \frac{1}{2}g_I\beta_I B_Z - a/4, \tag{3.26}$$

$$\varepsilon_2 = E_{1/2,1/2} = \frac{1}{2}g\beta B_Z - \frac{1}{2}g_I\beta_I B_Z + a/4, \tag{3.27}$$

$$\varepsilon_3 = E_{-1/2,-1/2} = -\frac{1}{2}g\beta B_Z + \frac{1}{2}g_I\beta_I B_Z + a/4, \tag{3.28}$$

$$\varepsilon_4 = E_{-1/2,+1/2} = -\frac{1}{2}g\beta B_Z - \frac{1}{2}g_I\beta_I B_Z - a/4. \tag{3.29}$$

The selection rules for EPR transitions are $\Delta m_S = \pm 1$ and $\Delta m_I = 0$. As a result, for the case of a spin system $S = \frac{1}{2}$, $I = \frac{1}{2}$ shown in Fig. 3.5, the energy differences of the two transitions are given

$$\Delta E_{12} = \varepsilon_2 - \varepsilon_1 = g\beta B_Z + \frac{1}{2}a, \tag{3.30}$$

$$\Delta E_{34} = \varepsilon_4 - \varepsilon_3 = g\beta B_Z - \frac{1}{2}a. \tag{3.31}$$

When only the two Zeeman interactions are considered, two distinct transitions occur, but because $\Delta m_I = 0$, they are energetically equivalent [Fig. 3.5 (c)]. Thus, only one line is produced. Only the addition of the hyperfine interaction results in the predicted splitting to the two EPR resonances [Fig. 3.5 (c)]. Usually there are several nuclei in a radical that can interact with the electron. The EPR spectra can thus be very rich in lines.

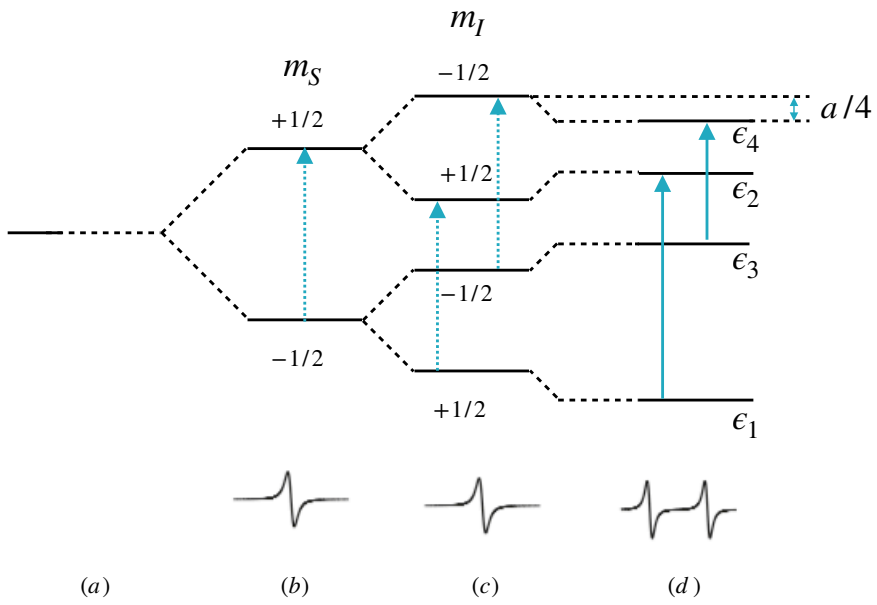

Figure 3.5: The scheme of energy levels, according to the (*b*) – electron Zeeman, (*c*) – nuclear Zeeman and (*d*) interaction of the hyperfine structure.

3.1.4. g-factor anisotropy

To explain the behavior of a resonance spectrum when anisotropy is present, we must first analyze the scenario of an ion with an anisotropic g-factor and no initial splitting of the energy levels or hyperfine structure. Consequently, the spin Hamiltonian consists just of the elements provided in equation (3.19). If the field $\boldsymbol{B}$ is oriented so that it possesses direction cosines (l,m,n) relative to the primary axes (x,y,z) of the g-tensor, then the Hamiltonian is:

$$\hat{\mathcal{H}} = \beta B(lg_x S_x + mg_y S_y + ng_x S_x). \tag{3.32}$$

If g were isotropic, we could use a new set of axes (x_e,y_e,z_e) with the z_e parallel to B, and the Hamiltonian would simplify (primes are used to relate $\boldsymbol{S}$ to the new axes) to:

$$\hat{\mathcal{H}} = g\beta B(lS_x + mS_y + nS_x) = g\beta BS'_z \tag{3.33}$$

where $g = g_x = g_y = g_z$. Clearly, the energy levels are a set of $(2S + 1)$ levels that are evenly separated in energy by $g\beta B$, and the transitions that are allowed are those in which the component S'_z changes by one unit, which means that they need a quantum

$$h\nu = g\beta B. \tag{3.34}$$

When anisotropy is present, the components off-diagonal in the energy matrix cannot be eliminated by switching to axis where z_e is parallel to $\boldsymbol{B}$. Nevertheless, it is clear that our Hamiltonian may be represented in the form

$$\hat{\mathcal{H}} = g\beta B(l'S_x + m'S_y + n'S_z), \tag{3.35}$$

where $gl' = g_x l$ and so on. If we now establish $(l'^2 + m'^2 + n'^2) = 1$, the Hamiltonian is identical to the ion one with g-factor, in the field $\boldsymbol{B}$ with the direction cosines (l',m',n'). Consequently, the energy levels will be the same as previously described, and the resonance condition will be provided by equation (3.34), where, from the normalizing of the apparent direction cosines (l',m',n'), we have:

$$g^2 = l^2 g^2{}_x + m^2 g^2{}_y + n^2 g^2{}_z. \tag{3.36}$$

We have essentially diagonalized the energy matrix by adopting a new set of axes in which the z-axis has direction cosines (l',m',n') with respect to the major axes (x,y,z) of the g-tensor.

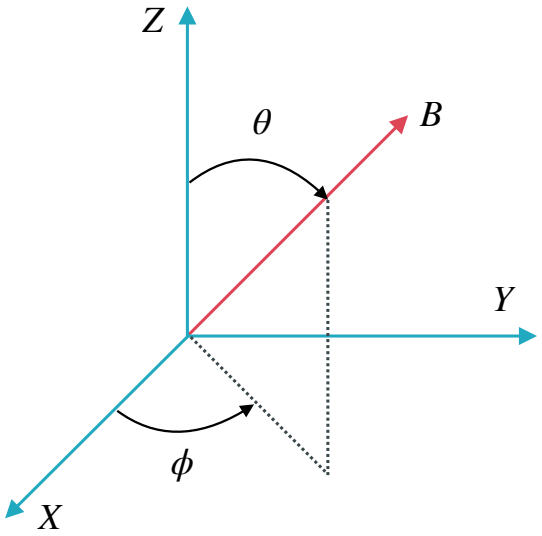

Figure 3.6: The magnetic field's orientation in relation to the X, Y, and Z primary axis system of the g-tensor.

The frequency necessary for the EPR transition, according to the fundamental EPR resonance eq. (3.34), entirely depends on B and β since the g value in this equation is isotropic. To account for this angular dependency, equation (3.34) must be adjusted. The EPR spectrum in the solid state will rely on the relative direction of the applied B with regard to the paramagnetic particles in the powder:

$$h\nu = \beta g(\vartheta,\varphi)B, \tag{3.37}$$

where ϑ and φ are the polar angles of the applied B inside the molecular g tensor primary axis system [Fig. 3.6].

It is enough to remark here that the effective g value may eventually be represented in a way that includes the angular terms from equation (3.37), as follows:

$$g(\vartheta,\varphi) = \sqrt{\sin^2\vartheta \cdot \cos^2\varphi \cdot g_1^2 + \sin^2\vartheta \cdot \sin^2\varphi \cdot g_2^2 + \cos^2\varphi \cdot g_3^2}. \tag{3.38}$$

Different g values can be seen in the EPR spectrum as a result of these angular variability.

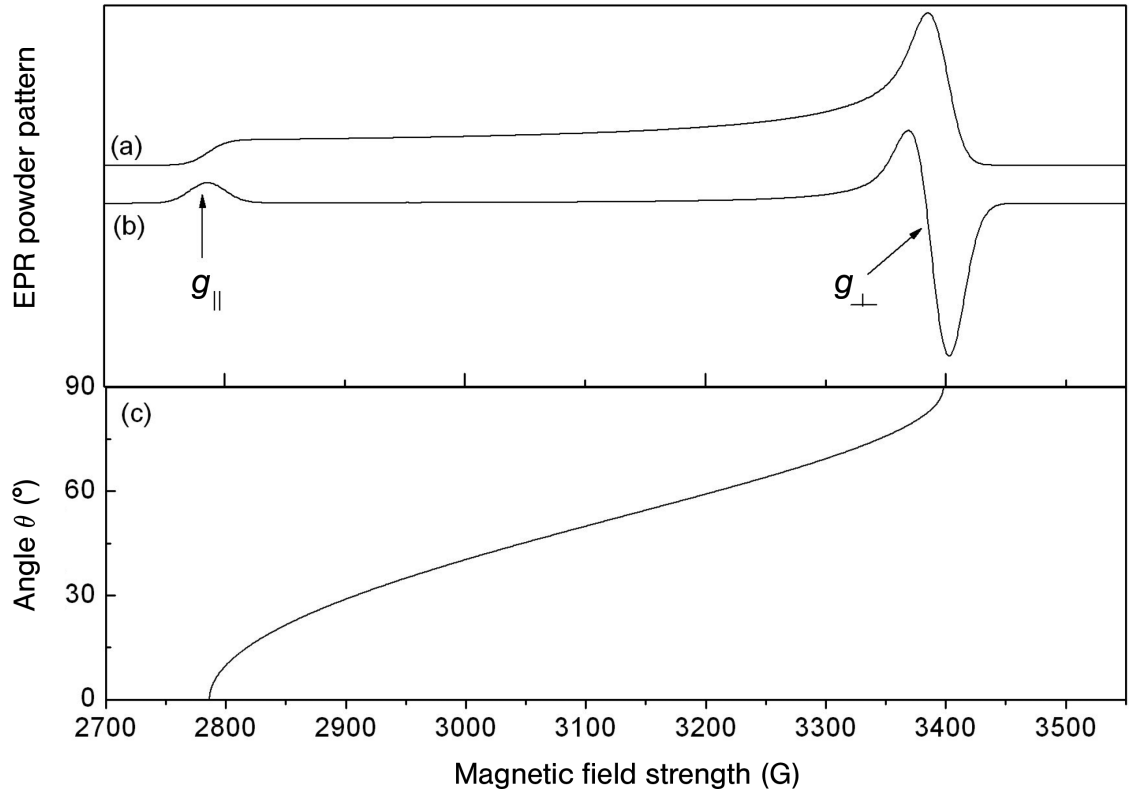

Figure 3.7: Absorption and first derivative EPR lineshape for an axially symmetric $S = = \frac{1}{2}$ spin system (randomly oriented) are shown in (a) and (b), respectively. The angular dependence curve is depicted in (c). Taken from [56].

Lower than isotropic symmetry, including such axial ($g_{xx} = g_{yy} \neq g_{zz}$ and $A_{xx} = = A_{yy} \neq A_{zz}$), rhombic ($g_{xx} \neq g_{yy} \neq g_{zz}$ and $A_{xx} \neq A_{yy} \neq A_{zz}$), monoclinic, or triclinic symmetry, is more frequently observed in the paramagnetic centers examined in metal oxides. Consider a fundamental paramagnetic component ($S = \frac{1}{2}$), for instance, which has uniaxial symmetry without hyperfine interaction. This system may be described by the two primary axis g values $g_{||}$ and $g_{\perp}$, respectively. The variation in the g value will simply rely on the angle ϑ between B and the x, y, or z axis, as was highlighted in equation (3.38) for the general case when $x = y = z$. Equation (3.38) may be simplified for uniaxial symmetry, where $x = y \neq z$:

$$B(\vartheta) = \frac{h\nu}{\beta}(\sqrt{g_{||}^2 \cos^2\vartheta + g_{\perp}^2 \sin^2\vartheta})^{-1}. \tag{3.39}$$

The range of B over which absorption occurs is thus determined by the values of $g_{||}$ and $g_{\perp}$, and two peaks will arise at the field coordinates $B_{||}$ and $B_{\perp}$. For those paramagnets whose field is oriented along the symmetry axis, which corresponds to an angle of $\vartheta = 0°$, absorption occurs when the field is aligned along the special axis ($B_{||}$). Only a few spins contribute to the pattern at this orientation, and the spectrum intensity has a minimum at 2800 G [Fig. 3.7]. More spins enter resonance as the field progresses from $B_{||}$ to $B_{\perp}$, increasing the strength of the absorption line as a result. Since there is now a significant plane of orientations with the field perpendicular to the symmetry axis, the absorption peaks at $B_{\perp}$. Although the first derivative of the absorption is always recorded in the continuous wave (CW) EPR spectra [Fig. 3.7 (b)], it is still feasible to determine the values of $g_{||}$ and $g_{\perp}$ from the powder spectrum. Fig. 3.7 (c) depicts the variation in the resonance absorption (equivalent to the variation in g) as a function of angle ϑ as a smooth curve with two distinct resonances at $B_{||}(g_{||})$ and $B_{\perp}(g_{\perp})$. It is crucial to understand that because the total signal strength is distributed between the field points $B_{||}$ and $B_{\perp}$, it can occasionally be challenging to precisely identify $g_{||}$ and $g_{\perp}$ in powder spectra with several sites or various paramagnetic species.

3.2. Electrically Detected Magnetic Resonance (EDMR)

3.2.1. Fundamentals

The magnetic resonance technique – electrically detected magnetic resonance (EDMR) has been proven a sensitive (about 10^7 times greater than electron paramagnetic resonance (EPR) [31]) and powerful method for characterization of charge carriers, defects and impurities in a variety of semiconductive solids by providing insights into fundamental physical phenomena of magnetic resonance and aid in-situ studies for further reliable devices development [65–67]. EDMR is derived from EPR, but its detection scheme is distinct: spin-dependent processes are monitored via the change in the device's current or voltage under microwave excitation. In EPR, the transitions between electron spin energy levels [see Fig. 3.8 (a), (b)] are measured as a microwave absorption, when the following resonance condition is fulfilled (for the simplest case of a system with the spin $S = \frac{1}{2}$):

$$h\nu = g\beta B, \tag{3.40}$$

where h is the Planck constant, ν – microwave frequency, β – Bohr magneton, g – g-factor and B – magnetic field. The splitting of these energy levels in the presence of the magnetic field is called Zeeman effect [see Fig. 3.8 (a)].

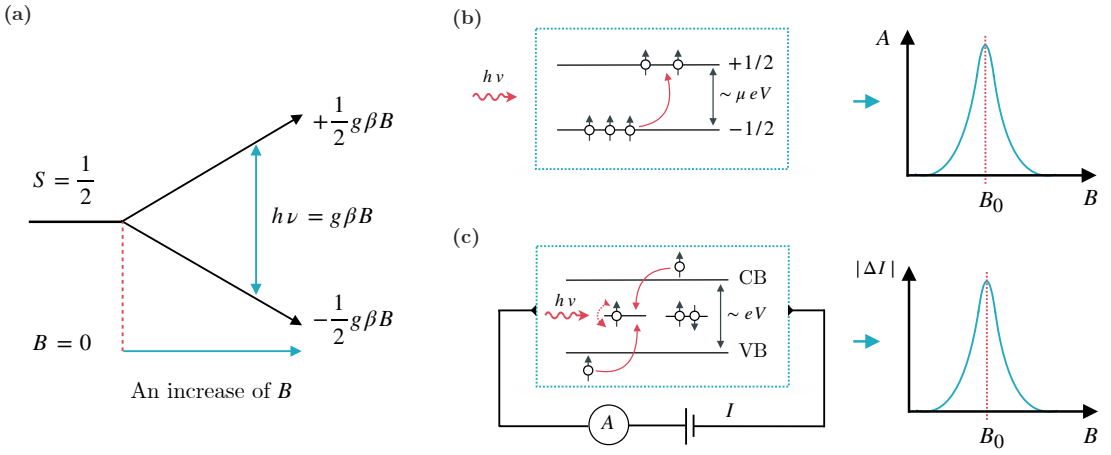

Figure 3.8: (a) – a diagram of the Zeeman effect for a system with spin S $= \frac{1}{2}$ placed in the magnetic field B; h is the Planck constant, ν – microwave frequency, β – Bohr magneton, g – g-factor. (b) – The basic principle of EPR detection. The EPR transition in the sample due to the resonance condition (3.40) is observed as the microwave absorption of the sample. (c) – The principle of EDMR detection. Microwave irradiation flips the spin of the unpaired electron in the defect center (recombination center) and the spin-dependent process happens. As a result, one observes a change in the sample current under the resonance condition (3.40). Note, that a common Zeeman energy splitting is in a range of μeV, whereas the bandgap in semiconductor is in eV.

In EDMR, these transitions are observed as a change in the electrical conductivity of the sample [Fig. 3.8 (a)–(c)]. The reasons for causing this change are spin-dependent processes such as recombination, tunneling, or hopping [68, 69]. In contrast to the EPR, which is insensitive to these processes, the EDMR can examine these transport mechanisms, as they are based on spin selection rules. As a result of the significance of point defects and impurities in semiconductor devices, detection of electrical conductivity is preferred over detection of microwave absorption. Defects concentration in modern devices is insufficient for conventional EPR, which requires a minimum of 10^{11} paramagnetic centers, but EDMR can detect defects, in general, as small as 10^6 [32, 70], or even a single electron [33].

This method's history begins in 1960's. One of the first EDMR observations was in 1966, where Schmidt and Solomon [20] described spin-dependent recombination of free carriers, investigated in phosphorus-doped silicon. In 1972, Lepine proposed that the capture of the conduction electron by the recombination center depends on their relative spin orientation [71]. Problems developed when this model was unable to account for the signals observed in later measurements made by other researchers. There were several prior theoretical attempts to explain the EDMR signal before Kaplan, Solomon, and Mott [72] turned to Pauli's permutation-symmetry model based on the Pauli blockade in 1978. According to the description, charge carriers in localized electronic states first form an 'exceptional pair' during a 'readjustment time' before a recombination transition happens. A more thorough explanation of EDMR, as well as a detailed description of several spin-dependent models, can be found elsewhere [68, 69].

3.2.2. The Lepine Model

In accordance with the *Pauli's exclusion principle* (two or more identical particles with half-integer spins cannot simultaneously occupy the same quantum state within a quantum system), if the recombination center is paramagnetic (has an unpaired spin), then it can capture an electron from the conduction band only if the two spins are antiparallel to each other. In other words, the capture cross section is much higher if the spin of an electron of the recombination center is antiparallel to the spin of an electron in the conduction band.

Since the spins tend to orient themselves parallel in a magnetic field B, the capture cross section is small. However, if we apply microwaves with the resonance frequency, it will start to flip the spins of the recombination centers resulting in the increase of the recombination rate. The magnitude of this effect is proportional to the microwave power, and reaches its maximum value when the EPR transition becomes saturated, i.e when the number of parallel spins is equal to the number of antiparallel spins within the ensemble of recombination centers. Dependence of the conductivity's change on the polarization of the conduction electrons p_e and the polarization of the paramagnetic recombination center P_r can be characterized as:

$$\Delta\sigma \propto p_e P_r. \tag{3.41}$$

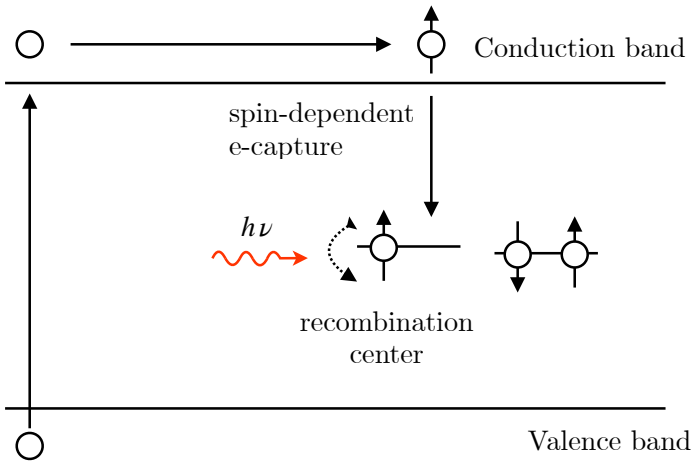

Figure 3.9: Spin-dependent recombination mechanism after Lepine.

Here, according to equation (3.41) was expected a temperature and a field dependence of the change of conductivity $\frac{\Delta\sigma}{\sigma}$ to be proportional to $(\frac{B_0}{T})^2$. However, it was not verified in experiment [73] where the low (X-band) frequency EDMR experiments are described.

3.2.3. The model of Kaplan, Solomon and Mott

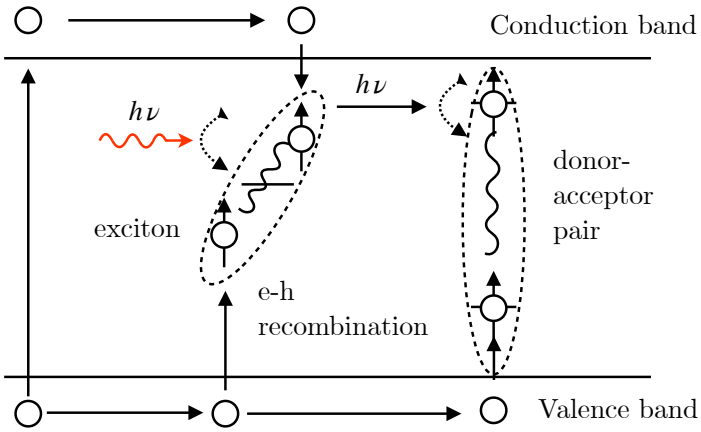

Figure 3.10: Mechanism of spin-dependent recombination according to the KSM model. Recombination probability depends on the spins orientations of the charge carriers within electron-hole pairs.

Compared to the Lepine model, *Kaplan, Solomon and Mott* (KSM model) assume that electrons and holes are captured by recombination centers irrespective of their spin orientation, and that they form electron-hole pairs [72]. In this model, the electron-hole pairs can form at some defect, which will then lead to the recombination of excitons. Spin-dependence of the recombination rate arises due to the formation of an intermediate spin pair, which is formed before the actual recombination process. In this model only the spin correlation effect of electrons and holes influences the rate of recombination. Consequently,

there is no influence of an external magnetic field or the polarization of electrons or holes on the rate of recombination, which is exactly what was observed in the experiment.

Also, if there is no correlation between the recombination mechanism and the magnetic properties of the recombination center, electron-hole pairs must be formed at separate but weakly (or more strongly) coupled donors and acceptors.

3.2.4. The Shockley-Read-Hall Model

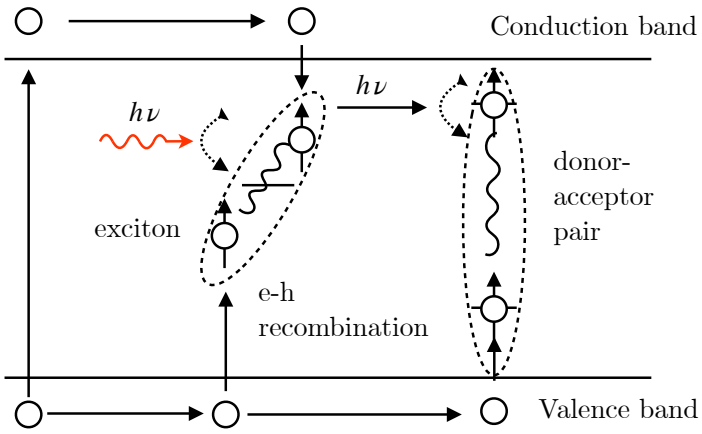

Figure 3.11: Mechanism of spin-dependent recombination after [74]. An electron is captured into excited state of the paramagnetic recombination center, according to which the readjustment time depends on the spin orientation of both carriers.

This spin-dependent SRH model was originally proposed by Rong [74]. The key idea of this model is so-called 'readjustment time', during which the charge carriers form an exclusive pair before an actual recombination happens. Rong assumed that the electron which was captured from the conduction band goes to an excited state in the recombination center before it relaxes to the ground state of the recombination center (see Fig. 3.11). The readjustment time leads to the fact that the captured electron with a spin parallel to the electron in a paramagnetic center cannot relax to the ground state of the recombination center, thus the recombination cannot happen and it goes back to the conduction band.

The EPR transition in the paramagnetic recombination center forces the spin to flip, and the captured electron relaxes from the excited state to the ground state of the recombination center. After this process, it can finally recombine with a hole.

Numerous models have been proposed by researchers associated with electrically detected magnetic resonance in different types of samples, investigating wide range of defects and impurities. However, each of the models could help in the analysis of the EDMR spectrum only in certain cases created for it. There are no 'versatile' models for describing most of effects, but there are parameters by which one can determine which of the models fall under a certain mechanism [3.12] of spin-dependent processes [32, 68].

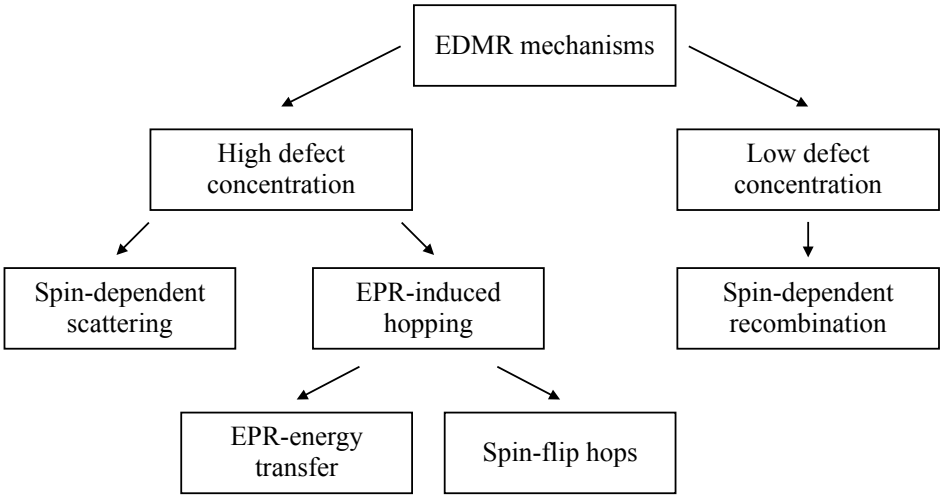

Figure 3.12: EDMR mechanisms described in [32]. Adapted from [32].

3.2.5. Other EDMR Models

As shown by reference [32], the EPR-induced hopping process, including EPR-energy transfer and spin-flip hops models, is the primary mechanism responsible for the low-temperature EDMR signal in highly-doped n-type SiC monocrystals with N donor concentrations close to but below N_{crit} for Mott metal-insulator transition.

Based on the EPR-energy transfer model [75], the localized electron at site α is first excited to the upper Zeeman level by absorption of m.w. energy, then the localized electron at the Fermi level moves from site β to site k via exchange interaction with the electron at site α [Fig. 3.13]. In this condition, the spin-orbit interaction must be considered because the exchange interaction conserves the total spin of two electrons.

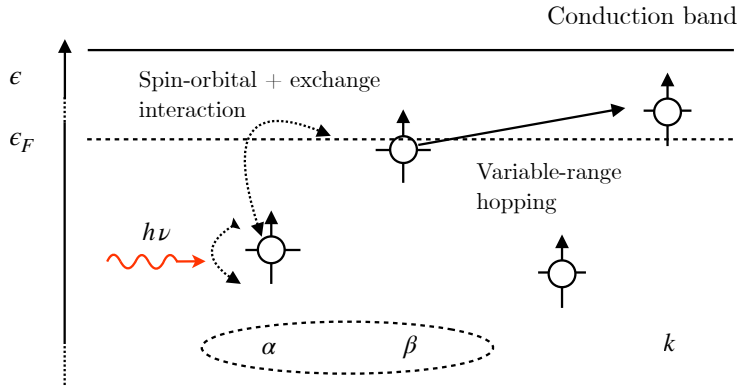

Figure 3.13: EPR-energy transfer model. ε_F – Fermi level. Adapted from [32].

The spin-flip hops model [76] explains hopping between occupied states, which is spin-dependent, as an electron can only hop to sites occupied by an electron with antiparallel spin orientation. The probability of discovering sites with antiparallel spin orientations increases as a result of spin flips enhancing the hopping process. In this situation, the

hopping time must be significantly shorter than the spin-lattice relaxation time. First, the electron at site α absorbs a m.w. phonon, which excites it to the upper Zeeman level [Fig. 3.14]. There are two contributing processes to spin relaxation. The first corresponds to normal spin-lattice relaxation, in which the electron returns to the lower Zeeman level and emits a phonon with the energy $h\nu_{phonon} = h\nu_{m.w.}$. The second process occurs when an electron hops to a nearby ionized donor, reverses its spin, and emits an energetic phonon $h\nu_{m.w.} - \Delta\varepsilon$ ($\Delta\varepsilon$ – difference in the potential energy of the donors α and β). Further mechanism can make a non-negligible contribution to conductivity: the electron at site α is excited to the upper Zeeman level, followed by a hop to site β' accompanied by a spin-flip as the required energy decreases (occurs when the potential energy difference between α and β' ($\Delta\varepsilon'$) is comparable to the EPR energy $h\nu_{m.w.}$).

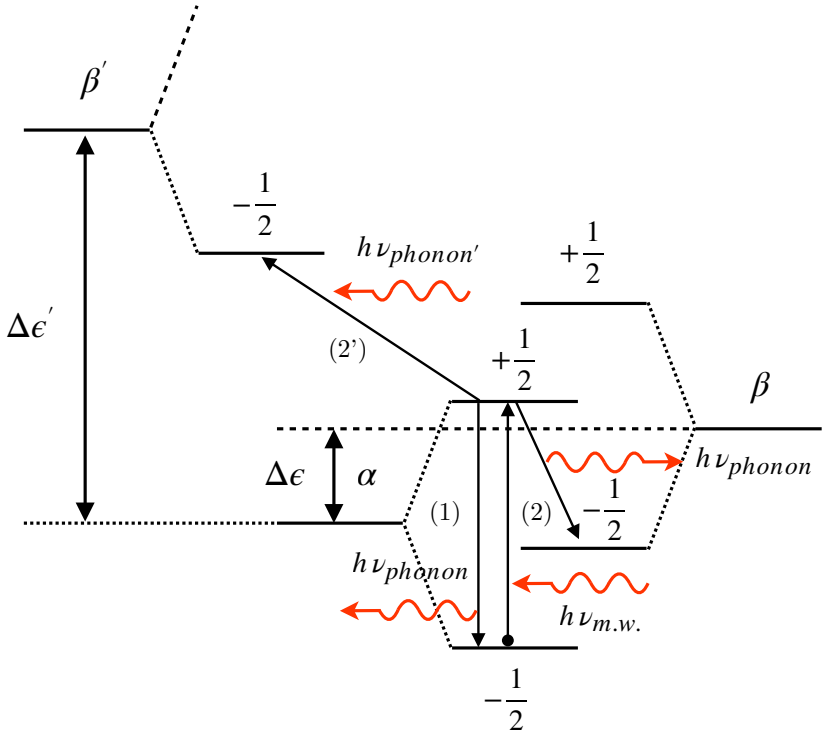

Figure 3.14: The spin-flip hops model. (1) – the normal spin-lattice relaxation process, (2) – the process of electron hops to a neighboring ionized donor reversing its spin and emitting a phonon of energy $h\nu_{m.w.} - \Delta\varepsilon$. (2') – the electron at site α is excited to the upper Zeeman level and then the hop to site β' accompanied by a spin-flip since the energy needed has diminished. Adapted from [32].

One more mechanism that results in additional hopping has been described for 6H SiC [32] – resonant m.w. absorption at very low temperatures in the variable-range hopping (VRH) mode [Fig. 3.15]. In this model, an electron at site α can jump to the vacant site β by absorbing a m.w. photon, resulting in an energy separation between the two sites equal to the energy of the photon. For this $\varepsilon_{\alpha\beta}$ value, there exists a definite number of N

donor pairs consisting of one ionized donor and one neutral donor with an approximate energy difference of m.w..

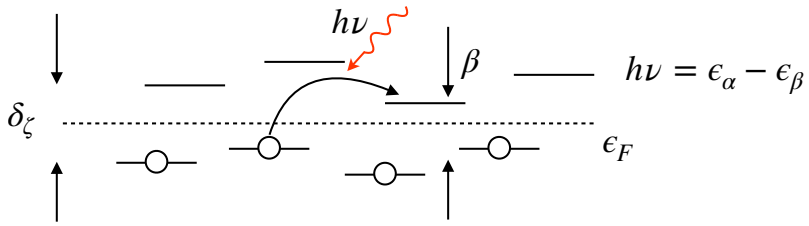

Figure 3.15: The resonant m.w. absorption process.

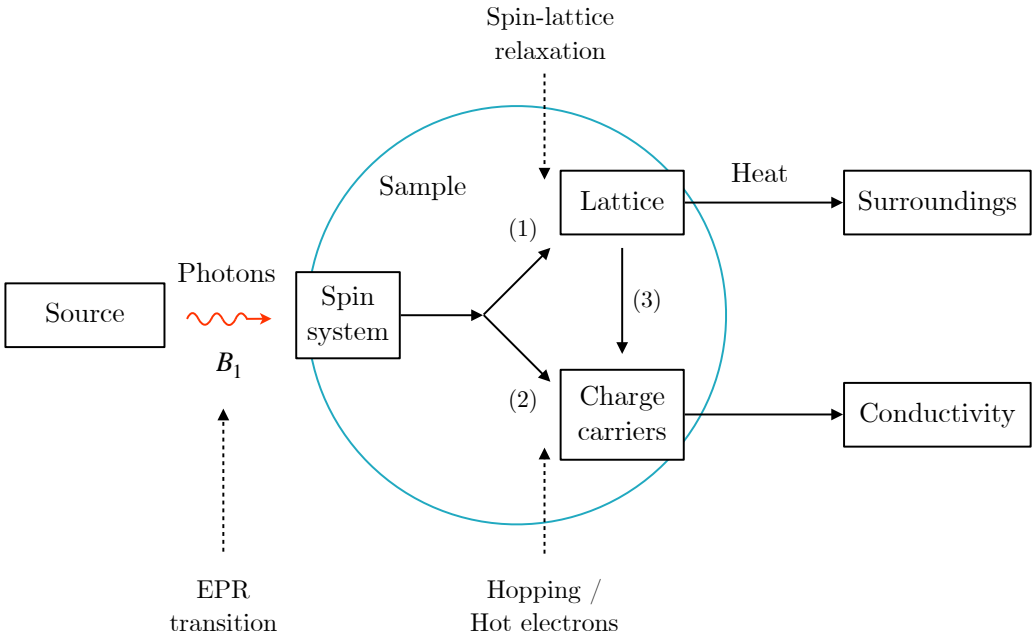

Figure 3.16: EPR-induced temperature increase mechanism responsible for appearance of low-temperature EDMR signal in VRH regime in 6H SiC [32].

The appearance of the EDMR signal in the VRH regime in highly N-doped 6H SiC monocrystals is attributed to the EPR-induced temperature increase mechanism, according to [32]. This process's corresponding model is depicted in Fig. 3.16. First, the spin system absorbs the photon energy and then loses it via diffusion to the lattice (spin-lattice relaxation), allowing photon absorption to continue. The m.w. source transfers energy to the investigated sample, which then transfers energy to the environment. Conductivity increases with sample temperature in the absence of heat removal mechanisms. In addition, spins can lose m.w. energy directly at the Fermi level (hopping), resulting in an increase in conductivity.

3.3. Summary

This chapter reviewed the fundamental concepts of the phenomenon of paramagnetic resonance, explaining the determination of the magnetic moment of the electron and its behavior in the presence of an external magnetic field and microwaves. In addition, we demonstrated that electrically detected magnetic resonance depends directly on electron paramagnetic resonance. Furthermore, we investigated the spin-dependent recombination mechanisms that are integral to electrically detected magnetic resonance. Several models were considered in order to characterize the spin-dependence mechanisms. The future chapter presents a review of existing instrumentation for EDMR, as well as a comparison of existing setups and methodologies.

4. Instrumentation

This chapter provides an introduction to EDMR instrumentation, an explanation of the EDMR measurement principle, an examination of existing EDMR solutions, and a comparison of the parameters of existing EDMR research instrumentation. Determining the constraints of existing EDMR setups based on sample size and frequency increase.

4.1. Review

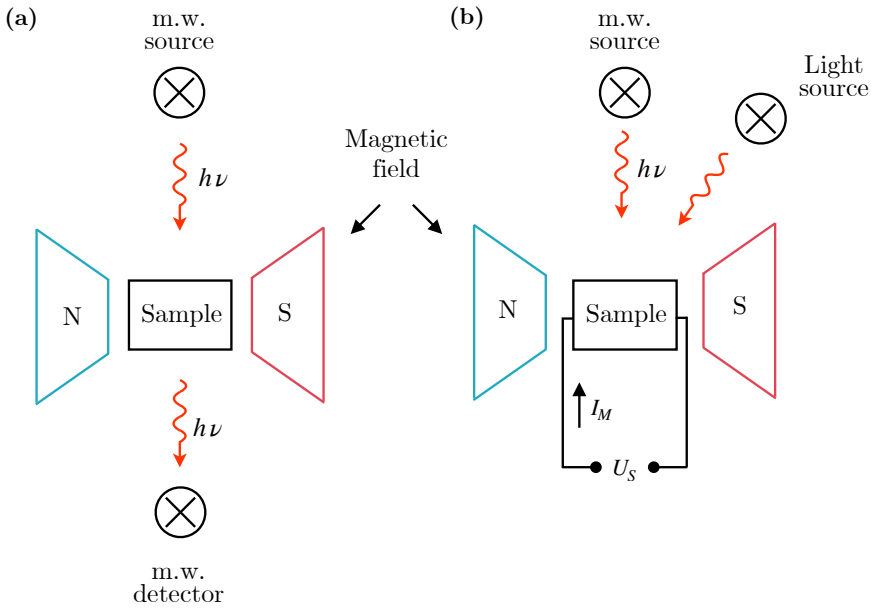

Figure 4.1: Simplified scheme of difference between (a) EPR experiment – detection of absorbed energy by the sample and (b) EDMR – detection of change of a current I_M by applying voltage U_S.

Standard continuous wave (CW) EPR utilizes microwave sources to irradiate the sample inside the m.w. resonator, which is located in an external magnetic field B. A common way to significantly improve the signal-to-noise ratio is to modulate the external field and to use the phase sensitive detection. As a rule of thumb, the modulation amplitude should not exceed the width of the EPR line in order not to distort the line shape. While sweep-

ing the B value over the resonance range with matching m.w. absorption, the spectrum is recorded. The change in m.w. power is recorded at the frequency of the field modulation.

An EPR spectrometer must meet five key technical requirements:

(1) A powerful, uniform, and steady magnetic field is required;

(2) There must be low-noise microwave sources;

(3) Low-loss m.w. transmission line should be configured;

(4) The resonator must have as high Q-factor as possible;

(5) The noise floor of the m.w. detector should be less than EPR-caused changes in m.w. power reflected in the resonator.

As previously stated, EDMR is engaged in the detection of changes in a material's conductivity under the resonance condition in the paramagnetic centers, which are attributable to spin-dependent processes. As a result, we are not interested in m.w. absorption in EDMR, and the aforementioned key requirement (5) can be ignored; however, condition (4) must be partially met in terms of resonator coupling to ensure the proper m.w. power transfer from waveguide to the cavity. The crucial difference between EPR and EDMR is the detection system [Fig. 4.1]. In the case of EPR, we observe the polarization of the spin ensemble, and in EDMR we measure the change of the current or voltage in the sample. As a result, we can add three additional key requirements for the EDMR spectrometer: (1) a stable voltage source, (2) a low-noise current preamplifier, and (3) reliable sample connectivity. The first two can be combined in one device (e.g., Stanford Research Systems SR570). The reliable current preamplifier is necessary since, in EDMR, the current change under the resonance condition is usually in the pA range, making often it challenging to discern the EDMR signal over the background noise brought on by simple interference with lab equipment.

Measurement results in EPR and EDMR match only by the Landé factor of detected spins. In this thesis, the dynamics of spin systems and pulse methods for their determination will not be addressed. However, the pulsed EDMR technique as well as a description of the setups can be found elsewhere [18, 77–81] Instead, we will focus on CW EDMR, which means that the sample is exposed to a continuous wave m.w. irradiation at a fixed m.w. frequency while the magnetic field is swept and vice versa - frequency domain EDMR (FD EDMR).

Before 2000's, there were no commercial solutions for EDMR. In general, the EDMR method was implemented directly on the EPR spectrometer with the modification and refinement of some modules. Quite recently, commercial systems were manufactured for EDMR as well, which are shown in [Fig. 4.2]: a Blue Spin (Blue Spin LLC, USA) low-frequency EDMR spectrometer and a JEOL EDMR (JEOL, Japan) control unit [82].

Blue Spin LLC is an industry leader in the development and manufacture of zero-field and low-field EDMR spectrometers. These spectrometers make it possible to identify

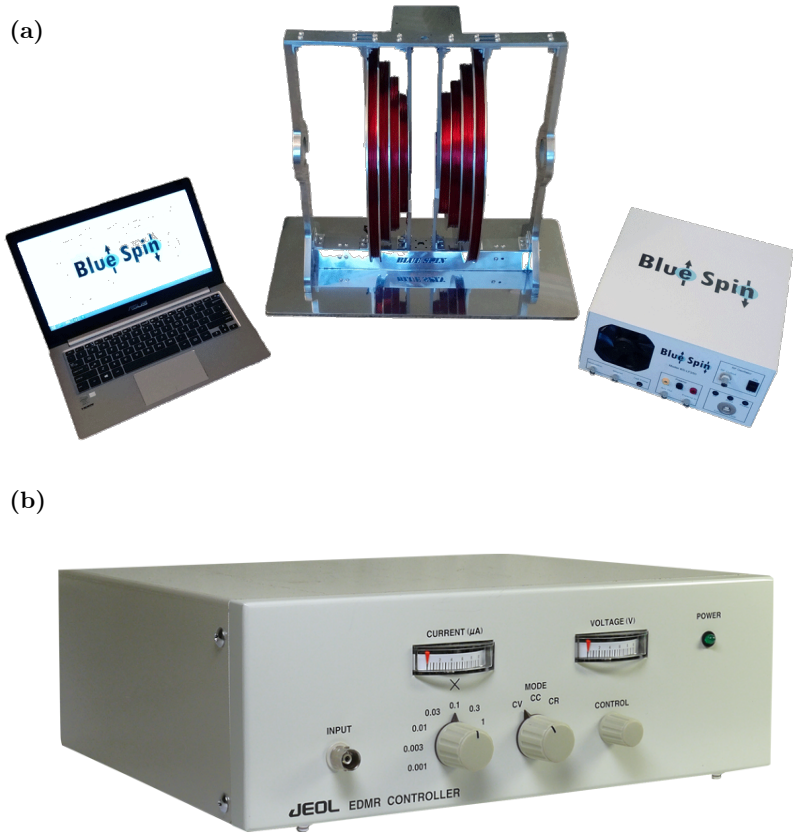

Figure 4.2: (a) – The photo of the Blue Spin low-frequency EDMR setup (Blue Spin LLC, USA) and (b) – JEOL EDMR controller (JEOL, Japan).

atomic-scale defects in nano- and microelectronics that have been fully processed. The company was founded in 2013. Spectrometers from BlueSpin are used extensively to improve the reliability of studied devices and for the research of spin-dependent mechanisms in electronics. Also, they are roughly 10^7 times more sensitive than conventional EPR spectrometers. In addition, they are significantly less expensive, require less power to operate, and occupy a much smaller space. Also, they are able to detect defects in a variety of devices, including MOSFETs, bipolar transistors, diodes, solar cells, and thin-film dielectrics. Defect detection is also possible in numerous material systems, including silicon, silicon dioxide, silicon carbide, gallium nitride, organic semiconductors, etc [83–86]. Most of other setups are based on bench-top or stationary X-band EPR spectrometers, which are limited in the magnetic field range, frequency and / or temperature control. In bench-top spectrometers, pumping of liquid nitrogen is mainly used, which allows (at best) to cool the sample to $\approx 80\,\mathrm{K}$, which in principle limits the range of research. The maximum magnetic field in these spectrometers is around $0.5\,\mathrm{T}$, obviously limited to the dedicated spectrometer's band range. Refer to Table 4.1 for a comparison of typical microwave bands and their corresponding frequency ranges.

In a truly diverse EDMR setup [Fig. 4.3], the magnetic resonance technique is incorporated into the wafer probing station. The magnetic field B is implemented by mounting

Table 4.1: Common microwave bands and their corresponding frequency ranges given by Bruker Corporation with the magnetic field values for a sample with $g = 2$.

Waveband designator	**Frequency range (GHz)**	**EPR frequency (GHz)**	**Resonance field (mT)**
L	1-2	1	35
S	2-4	4	142
X	8-12	9.6	349
Q	33-50	34	1213
W	75-110	94	3354
mm	110-300	263	9400

an axially magnetised annular neodymium permanent magnet (grade = N52) on a vertical translation stage above the wafer chuck. The non-resonant probe has the ability to generate B_1 field (microwave magnetic-field component) in a small region that is at least several orders of magnitude higher than a typical TE_{102} cavity. In light of this, the non-resonant microwave probe ought to have a higher degree of sensitivity in comparison to a conventional EDMR resonator in terms of these relatively inconspicuous regions of excitation. In spite of the fact that the B_1 field is not uniform in larger devices, modern ones have an active area that is less than 2 microns, and as a result, it is uniform under the kind of dimensions that are being considered here. Astounding as it may sound, the probing station itself is able to perform B_1 field spatial profiling on a device that is continually operating. In this configuration, the spectra are obtained by varying the frequency of the microwave source [36].

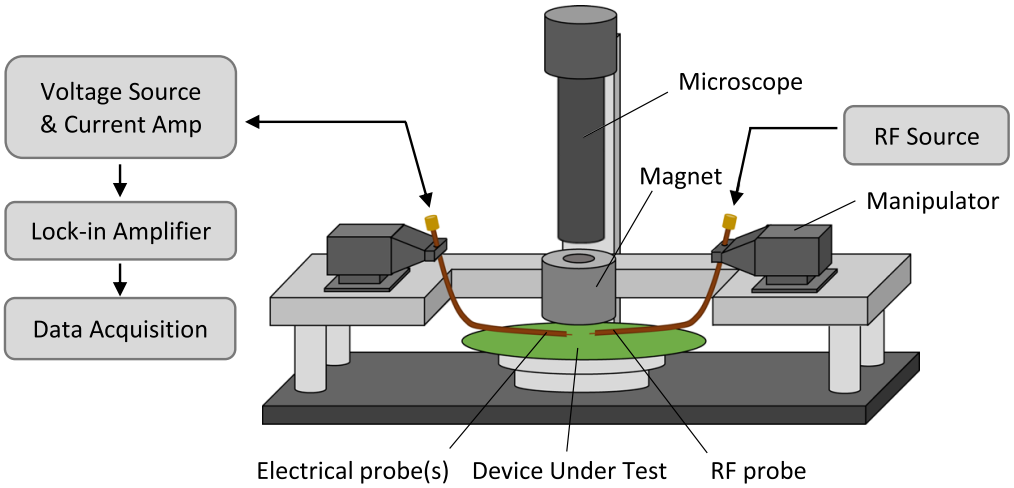

Figure 4.3: An illustration of the key components for the wafer-level EDMR spectrometer. Taken from [36].

Numerous EDMR studies employed commercial EPR spectrometers with minor modifications to the detection method [18, 87, 88]. Consequently, the microwave frequency and the magnetic field range are defined by the vendor in EPR spectrometers for their

particular application (e.g., commercially standardized X-band in CW and pulse modes, see Table 4.2). Thereby, the EDMR capabilities directly depend on the EPR setup itself.

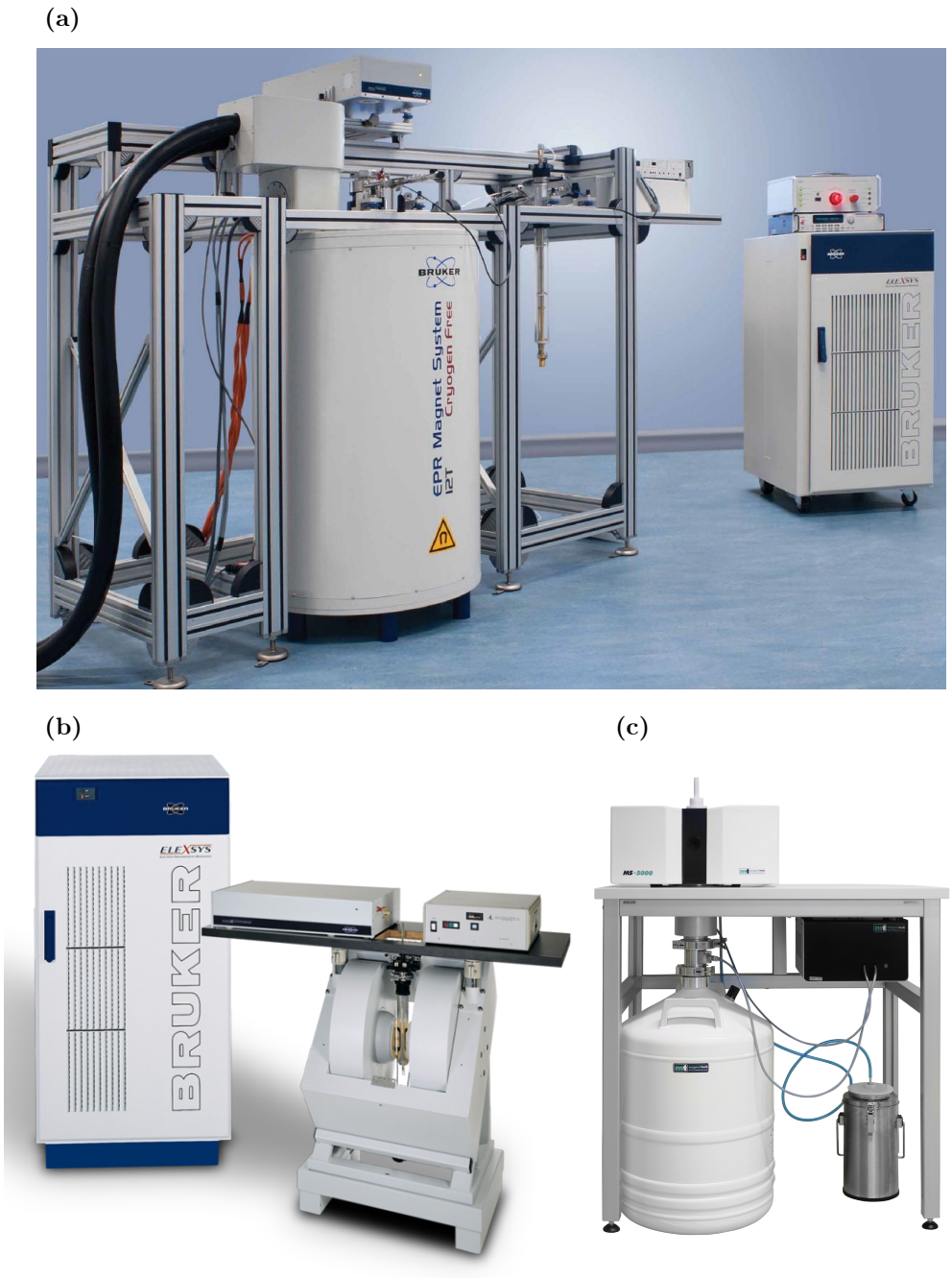

Figure 4.4: (a) – The photo of the Bruker ELEXSYS E780 spectrometer, (b) – Bruker ELEXSYS-II E580 (Bruker Corporation, USA) and (c) – Magnettech ESR5000 (Bruker Corporation, USA).

In the most basic form of approximation (not taking into account transistors and functioning electronic devices), one of the various methods for contacting the sample for EDMR measurements consists of two connections coming from the sample to which a specified voltage (depending on the sample itself) is applied and the current is being read. The

Table 4.2: A short comparison of existing EDMR research setups. MD – magnetic field domain (magnetic field sweep, constant frequency), FD – frequency domain (frequency sweep, constant magnetic field), CW – continuous wave.

Research field	**Methods used**	**Setup type**	**Frequency range (GHz) / Magnetic field max (T)**	**References**
Solar cells	Conventional CW and pulse modes	Commercial X-, Q-band and 263 GHz	10, 35, 263 / 1.2, 9	[18]
Wafer-based devices	CW and Rapid Scan	Homebuilt low frequency ($<$ 500 MHz), X-Band wafer-probing station	$<$ 0.5, 10 / 0.1, 1	[36, 38, 89, 90]
Quantum computing	CW and pulse	Commercial X-band	10 / 1	[33, 41–43]
Hybrid	CW MD and FD Rapid Scan	Homebuilt THz FraScan spectrometer	80-1100 / 16	[52, 91]

stability of the voltage source here plays an important role for measurement accuracy. For such measurements, current changes occur in the range of nano and microamps. Fig. 4.5 shows one of the possible current detection schemes, which may differ depending on certain spectrometer [92]. In [93], the current-to-voltage converter includes a constant voltage source for applying a constant voltage to the sample. In the transimpedance amplifier, the current signal is transformed to a voltage, which is then filtered by a bandpass with a lower cutoff frequency of 1 Hz in order to eliminate the DC-component of the current. Adjusting the upper cut-off frequency one controls the time resolution of the detection configuration. The signal is subsequently amplified to an appropriate level for the transient recorder of the Bruker spectrometer (Bruker SpecJet).

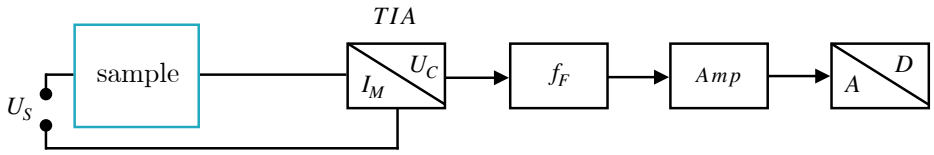

Figure 4.5: One of possible EDMR current detection scheme, (U_S) – voltage applied, (I_M) – measured current, (U_C) – converted voltage, (TIA) – transimpedance amplifier, (f_F)-bandpass filter, (Amp) - amplifier, (A/D) – digitizer. Adapted from [92].

Nowadays, there are a sufficient number of companies manufacturing EPR spectrometers. The world's leaders are Magnettech (Magnettech GmbH, Berlin, Germany)[1], Jeol (JEOL Ltd., Tokyo, Japan) and Bruker (Bruker Corporation, Massachusetts, U.S.) [Fig. 4.4]. The latter one is the most popular among EPR spectroscopy. The three main models which can be highlighted are X-Band Elexsys-II E500, Q-Band /W-band E580 and mm-wave Elexsys E780. For many decades, spectrometers of this company were held in high

[1]Magnettech's EPR business acquisition by Bruker Corporation was announced in 2019.

esteem because of their stability and reliability. All of them are designed for a wide range of studies of different materials. In our case, we will focus on semiconductor solid state materials. One of the main criteria, in addition to the value of frequency and a magnetic field in EPR spectrometers, is also the dedicated space for the sample. It depends on the size of the resonator, e.g., for the X-band – this is a tolerance of about 5 mm in diameter for the sample loading space, the Q-band is no more than 2 mm, the W-band has about half a millimeter. Consequently, it becomes highly difficult to place a device or a sample of working dimensions as frequency increases. To solve this problem at higher frequencies (> W-band), scientists developed another method – a non-resonant cavity-free probe using quasi-optics for m.w. propagation [94–97].

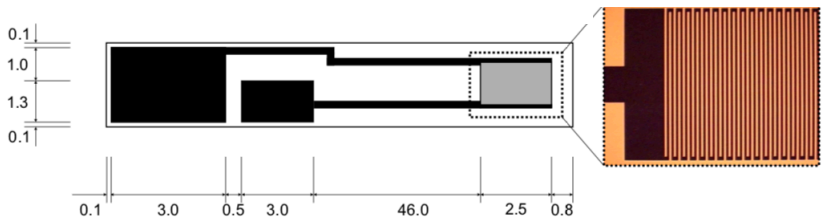

Figure 4.6: An example of contact-pad with IDE-contacts for solar cell measurements in X-band resonator. Taken from [93].

Important to consider is the method of sample contact. All further justification is contingent on the specific sample. As stated previously, the sample size is constrained by the size of the resonator, which is dependent on the spectrometer's operating frequency. Taking into account only X, Q, and W-band standardized resonators, modern systems have standard quartz tubes for sample loading, thereby reducing sample size. Under conventional measurement conditions, the quartz tube must be sealed (or closed), and there must be a certain amount of pressure and refrigerant vapor between the tube and the resonator. As shown in Fig. 4.6, for instance, the grey rectangle on the right side determines the position of the sample, assuming it is in the aforementioned quartz tube, which is located in the center of the resonator. The most suitable dimension for X-band is a 2.5 x 2.0 x 1.0 mm, taking into account the mounting of the sample on a specialized holder. However, with the increasing of m.w. frequency, it is possible to enlarge the space for placing the sample as, for example, this is done in [18] using non-resonant probehead, which is depicted in Fig. 4.7. This sample holder provides the space maximum of 5 mm in diameter for the sample. But also, in addition to the non-resonant probehead, the Elexsys E780 mm-wave EPR spectrometer can use a TE_{011} m.w. resonator [18].

To summarise the limitations of EDMR setups based on a common EPR spectrometer, we can note:

- Frequency range and magnetic field are typically set to the specified band (X-, Q-, W-, etc.).

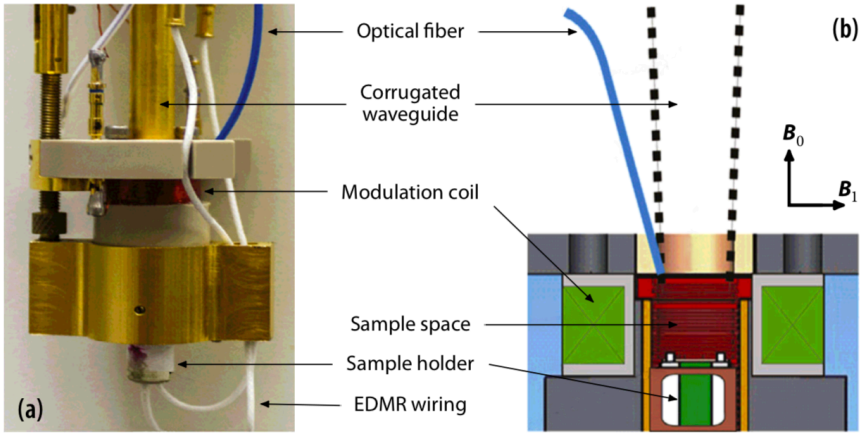

Figure 4.7: Photograph (a) and schematic section (b) of the 263GHz EDMR non-resonant probe head. Taken from [18].

- The sample size is determined by the dimensions of a particular resonator (and sample space decreases at higher frequencies).
- To achieve high sensitivity in CW EDMR without the need for high m.w. power, the resonator should have Q-factor as high as possible and it must be critically coupled to the m.w. transmission line. Conductive components and metallic contacts of the sample, which are unavoidable in EDMR samples, are typically a hindrance to achieving high Q values. While this is a small issue for some low-temperature experiments at X-band, it becomes a significant one at higher m.w. frequencies (Q-band and higher).

Consequently, an increasing number of custom-built solutions are being developed for a variety of particular samples and detection methods in EDMR described in this chapter.

4.2. Summary

To understand why different frequencies and magnetic fields are required, consider the theory stated in the previous chapter. We would want to obtain an EPR spectrum in which the components of the spin Hamiltonian are visible even from a cursory look of the spectrum's properties. Each component of the spin Hamiltonian is responsible for essential sample-specific information. The Landé factor value can provide information about paramagnetic particles, such as their electronic state and symmetry. Nuclear superhyperfine interactions provide us with the number and distance to the nuclei surrounding. Some characteristics, such as line width and anisotropy, may cover some of the features we want to understand. Higher magnetic fields, for example, make the Zeeman splitting component more dominant, overcoming second-order effects. However, by using different frequencies for EPR measurements, we can operate with different magnetic fields to fulfill

the resonance condition, emphasizing the influence of the spin Hamiltonian components that are dependent or independent of the magnetic field, and we can obtain precise values of the spin Hamiltonian parameters.

High Field / High Frequency EPR has been shown to be effective for studying high-spin ions, spin clusters, and single molecule magnets (SMMs) with magnetic interactions and anisotropy in the THz frequency range [51, 98–100]. The electrical characteristics, flaws, and structure of carbon-related nanomaterials have been studied using high-field / high-frequency EPR [101, 102]. Performing EDMR at higher (mm range) frequencies and fields can yield more accurate data with high resolution [53], and it can also allow examination of materials for which conventional setups cannot supply enough information for various technical reasons.

As we mentioned earlier, the EDMR technique can be used for the spectroscopic characterization of renewable energy elements, such as a photovoltaic devices on a nanoscale [18], study of the important recombination centers [103], silicon field-effect transistors [104], MEH-PPV-based diodes [105], organic light-emitting diodes (OLED) [44] and others.

Regarding the development of differentiated hardware approaches, for example, with the development of EDMR wafer probing stations [36], it becomes possible to analyze semiconductor devices in-situ on top of the wafer and spatially distribute the application of the B_1 field.

For a more conventional method, we may refer to the Bruker E-780 spectrometer, which operates at 263 GHz with a magnetic field of 12 T. This configuration employs a non-resonant probe system with a quasi-optical front-end. The sample diameter can be as large as 5 mm.

In conclusion, taking into account the above described limitations of the modern EDMR spectroscopy, we developed THz EDMR setup based on the THz FraScan spectrometer. The following section contains the general description of the THz FraScan spectrometer, its possibilities and limitations, as well as its EDMR implementation.

5. THz EDMR Setup

This chapter describes the development of an EDMR setup based on the THz FraScan EPR spectrometer (located in CEITEC, Brno, Czech Republic) which works within the frequency range of 80–1100 GHz and in magnetic fields up to 16 T [91] along with the detailed description on the EDMR sample holder, EDMR detection scheme and sample preparation.

5.1. General overview of THz FraScan Spectrometer

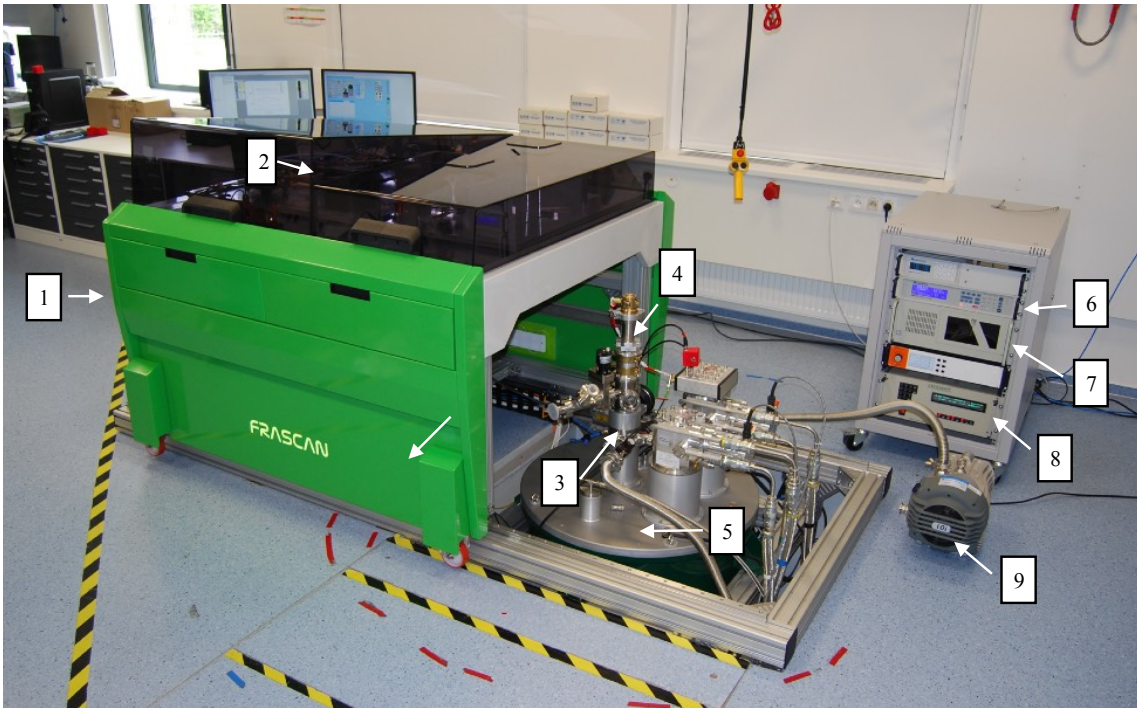

Figure 5.1: The photo of THz FraScan spectrometer located in CEITEC, Brno University of Technology, Czech Republic. The photo was taken with 'open' moving table (1). (2) – QO components under the protecting shield. (3) – Home-built airlock system as a part of variable temperature insert (VTI) of the superconductive cryogen-free magnet (5). (4) – The EPR probe loaded into VTI. (9) – The VTI pump. The spectrometer's rack on the right side of the photo is consist of temperature control unit (6), spectrometer's PC (7) and the magnet power supply (8).

Fig. 5.1 provides a general overview of the THz FraScan spectrometer located in the research group 'Magneto-optical and THz Spectroscopy' at the Central European Institute of Technology (CEITEC), Brno University of Technology, Brno, Czech Republic. The spectrometer consist of moving table (1), which slides into operational mode via the magnet frame rails. (Note, that the photo was taken when the spectrometer is in the 'open state'). On top of the table the quasi-optical (QO) components along with the m.w. sources and the m.w. detectors are hidden under the Plexiglas protection cover. The magnet frame for the operational mode moves (according to the photo – on the right side) to the certain point until the EPR probe (4) with the m.w. window is coupled with the QO table. The EPR probe is inserted in the variable temperature insert (VTI) of the superconductive cryogen-free magnet (5) through the home-built airlock system (3) which prevents the air contamination of the pure He environment. A dry scroll pump (9) creates a constant He flow in the close-cycle VTI with the pressure of $\approx 10\,\mathrm{mbar}$ in the sample space. To the right of the magnet frame is the spectrometer's rack, which contains a PC (7) that controls the spectrometer as a whole, the temperature control unit (6), the magnet power supply (8), and other equipment.

Fig. 5.2 depicts a schematic illustration of the EPR probe. The probe consists of either a 430 GHz or 100 GHz corrugated waveguide (Thomas Keating Ltd., UK) and is made of German silver. It is approximately 1 meter in length. The probe head is equipped with three separate signal connectors (Fischer Connectors SA, Saint-Prex, Switzerland) and a home-built optical fiber feedthrough (described in the next sections). Each of the signal connectors serves a particular function; with one, the signal from the sample is measured, with another, the temperature and magnetic field, and with the third, the modulation coil is being powered. The m.w. window is made of 70 microns thick of Mylar foil. The probe is positioned in the center of the non-magnetic stainless steel shield tube and surrounded by thermal shields. During the measurement mode, the EPR probe is loaded into the VTI space of the cryogen-free superconductive magnet until a certain point (when the sample is in the center of the magnetic field) and the necessary connectors are attached. After the EPR probe has been loaded, the moving table [Fig. 5.1 (1)] will be moved to a specific position so that the m.w. window of the EPR probe can be coupled with the m.w. output of the QO table. Depending on the dedicated frequency range, the spectrometer can be finely tuned to specific requirements (in the available frequency of 80 GHz to 1.1 THz). The sets of m.w. sources, m.w. detectors and QO compomnents (e.g. Faraday rotators) must be changed to the dedicated frequency range as well as EPR probes.

This setup works in various modes for different specific techniques, which involve EPR. However, in this thesis only the EDMR side will be highlighted. Development of the THz FraScan spectrometer began in cc. 2017 and on the photo it is fully operational (June 2020). However, a more complete version of the spectrometer in terms of EPR, RapidScan, and other techniques is available in [91].

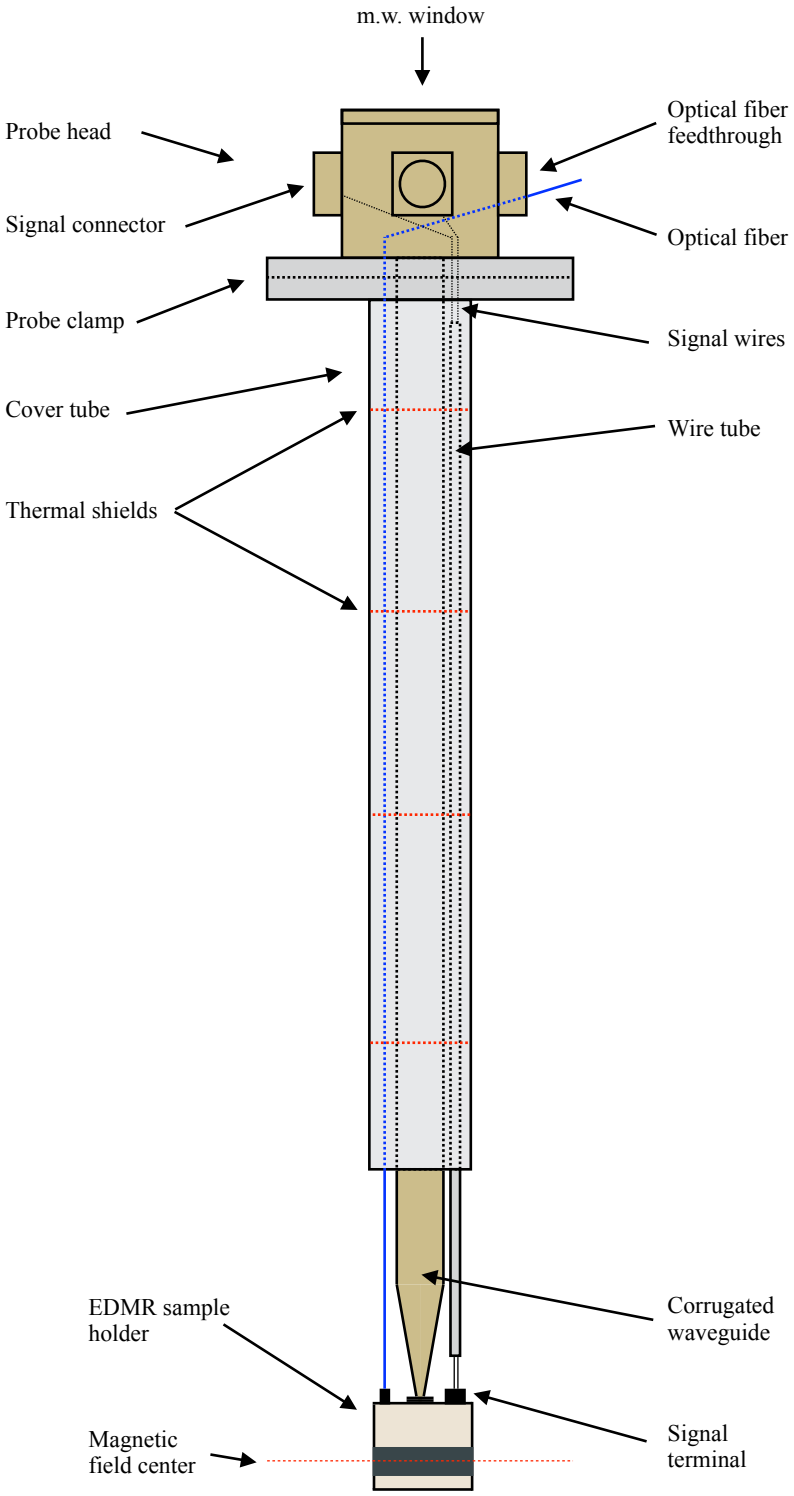

Figure 5.2: The detailed schematic illustration of the EPR probe with attached EDMR sample holder and the optical fiber.

5.2. Experimental Setup

We demonstrate the deployment of the EDMR approach in high magnetic fields and high frequencies using our THz FraScan spectrometer to extend the technique's current research

possibilities. EDMR measurements on strongly nitrogen-doped 15R SiC monocrystals are used to illustrate the setup's functionality in the following chapter. This section discusses the experimental setup and the EDMR detection scheme.

As previously stated, aiming for higher frequencies in EDMR using standard EPR spectrometers is already problematic at Q-band due to the limited volume for the sample in the cavity, which is 2 mm (in diameter) and half a millimeter at W-band. As a result, placing a functioning device or a sample of working dimensions becomes exceedingly challenging with increasing frequency. The non-resonant cavity-free configuration of the THz FraScan spectrometer, on the other hand, eliminates this issue. Apart from the setups that use microwave (m.w.) cavities, higher frequency (> W-band) solutions use quasi-optics (QO) for m.w. propagation. Quasi-optics, in our case, is a set of instrumentation such as elliptical mirrors, absorbers, Faraday rotators, etc. for the free-space propagation of THz-range Gaussian beam [106, 107]. Because the QO supports broadband operation, the frequency sweep option becomes possible. Fig. 5.3 depicts the general layout of the EDMR setup. The quasi-optical m.w. bridge has two operating modes: EPR and EDMR. A series of active and passive multipliers (Virginia Diodes Inc., Charlottesville, USA) allow the gap-less generation of microwaves with the frequencies ranging from 80 GHz to 1.1 THz. The EPR experiment requires both m.w. sources and m.w. detectors, whereas the EDMR measurement simply requires one m.w. source. Microwaves from the QO bridge propagate through the EPR probe's oversized corrugated waveguide and irradiate the sample put in the holder, which is connected to the EPR probe's end. A cryogen-free superconducting magnet system (16 T, Cryogenic Ltd.) houses the EPR probe, so that the sample is located in the middle of the magnetic field. A home-built airlock prevents the system's contamination by air during inserting/extracting of the probe. The magnitude of the magnetic field is read from the magnet's power source for the majority of the experiments. A reference sample with a known g-factor should be used to precisely determine the magnetic field (in this work we used $Cr^{3+}:MgO$ ($g = 1.9797$) standard sample). In the variable temperature insert (VTI) space (5) the temperature can be varied from 300 K to 1.8 K and can be measured precisely via a temperature sensor (3). The EPR probe head has three signal connectors and one optical fiber feedthrough (2), which allows to use different light sources (in this work we used diode lasers with the wavelengths of 403–636.7 nm and the broadband SLS201L lamp (Thorlabs, Inc., Newton, NJ, USA) for the EDMR experiment. Also, it contains a m.w. window made of Mylar foil (thickness of $\approx 70\,\mu$m), which isolates the VTI highly pure He atmosphere from the ambient air.

A common EDMR experiment requires the detection of extremely small changes of electric current in pA range, and for this reason we use SR570 (Stanford Research Systems Inc., Sunnyvale, CA, United States) current preamplifier. Depending on the sample's required bias voltage, the different biasing source can be used. However, to avoid additional noise pickups, we used the SR570's internal circuitry, which provides the biasing voltage of -5…+5 V. Additionally, we use a phase-sensitive detection (PSD) approach to substantially improve the signal-to-noise ratio (SNR) [108]. For the PSD method we use

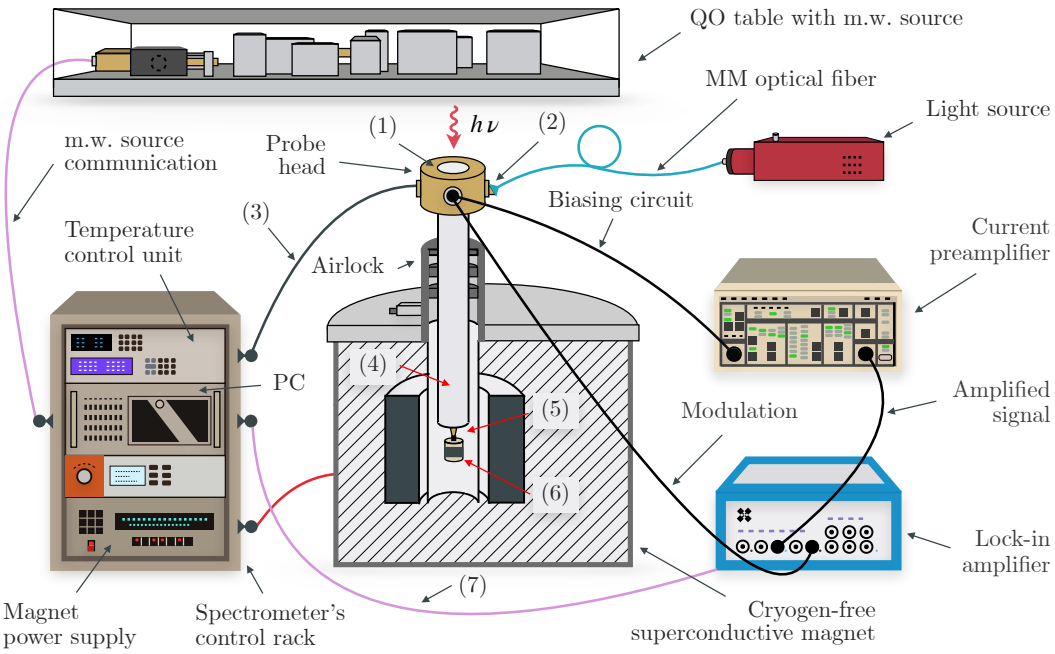

Figure 5.3: General scheme of THz EDMR setup. (1) – Microwave window, (2) – optical fiber feedthrough, (3) – temperature and magnetic field sensors, (4) – EPR probe, (5) – variable temperature insert (VTI) space, (6) – EDMR sample holder, (7) – Lock-in amplifier communication. QO – quasi-optics, MM – multimodal, m.w. – microwave. Data cables are indicated in violet color, signal cables – black, power – red color.

the magnetic field modulation, created by a small coil around the sample, as shown in the following section. The amplified signal from the sample is demodulated via an MFLI-500KHz (Zurich Instruments Ltd., Zurich, Switzerland) lock-in amplifier, a home-written LabView program [see Appendix (9)] controls spectrometer's equipment and acquires the EDMR signal from the lock-in amplifier. To the end of the EPR probe we attach the EDMR sample holder, which is described in the next section.

5.3. THz EDMR Sample Holder

The materials for the sample holder [see Fig. 5.4] were chosen based on the given conditions for a high magnetic field and low-temperature environment. The body of the sample holder and the inner base were made of polyether ether ketone (PEEK), which is a colorless organic thermoplastic polymer in the polyaryletherketone (PAEK) family, widely used in engineering applications. This material is able to withstand such extreme conditions. A commercial optical fiber collimator 300051 (World Precision Instruments Inc., Sarasota, FL, USA) uses a non-magnetic stainless steel shell; the mirror holders were manufactured from a phosphor-bronze sheet (thickness of 0.2 mm). Broadband 5 mm square UV enhanced aluminum coated, $\lambda/10$ mirrors (Edmund Optics Inc., Barrington, NJ, USA) (250–700 nm) (c) in Fig. 5.4 direct a light beam from the collimator to the sample. Dur-

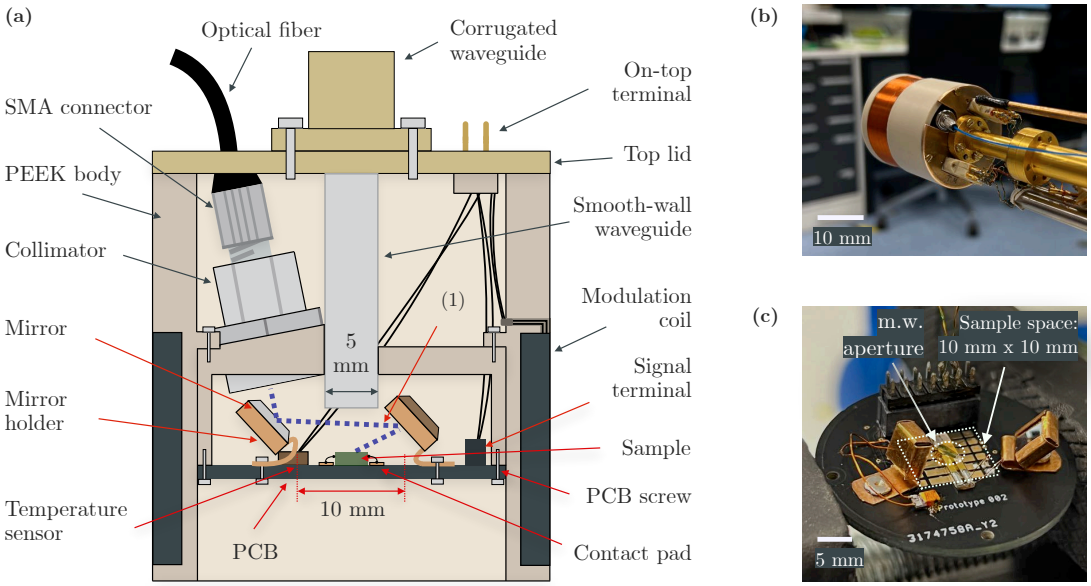

Figure 5.4: (a) – Schematic illustration of the EDMR sample holder. (1) – Collimated light beam. (b) – The sample holder is attached to the corrugated waveguide. (c) – The printed circuit board with mirrors and the sample. The allowed sample dimensions in this configuration are 10 mm x 10 mm x 7 mm (L x W x H), the microwave aperture is 5 mm in diameter.

ing cooldown and warmup of the VTI space the light reflected from the mirrors has no significant sight of deviation [see following subsection]. The sample is placed on a custom printed circuit board (PCB) with gold-plated copper electrical connections and FR-4 insulation (woven glass and epoxy). Using a PCB as a sample plate has the advantage of having reliable electrical connections and also providing mechanical and thermal stability. For instance, in the 'ambient' mode, when the microwave source and the current to the modulation coil are off, the difference in the temperature of VTI space and the sample can be less than 2 K, in the measurement mode m.w. source and the modulation coil produce additional heat and the temperature difference can be up to 5–6 K. In the case of EPR measurements, the end of the smooth-wall waveguide [Fig. 5.4] must be as closest as possible to the sample to avoid losses of scattered reflected waves. Since we are not interested in detecting the EPR signal, and, consequently, in the reflected microwaves, the waveguide is located about 7 mm above the sample, to allow for additional tolerance for the sample height and proper light beam alignment using the mirrors. Nonetheless, the sample holder has the ability to measure EPR with measured losses (-17.8 dB, Fig. 5.10), but enough to locate the EPR signal while calibrating the magnetic field sweep window. The whole space for the sample can be adjusted by manufacturing a PCB (the diameter of PCB is 36 mm), while now the space is limited to 10 mm x 10 mm x 7 mm due to mirrors, temperature sensor and the signal terminal alignment. The height of 7 mm is considered when the light excitation is not used, otherwise the sample height of 2–3 mm is recommended because

of the required space for the light beam propagation. The microwave aperture is 5 mm in diameter. Depending on the sample's size it can be arranged spatially on PCB in the way that the m.w. aperture and the light (spot of which is 2 x 3 mm) covers the dedicated area.

5.3.1. Sample preparation

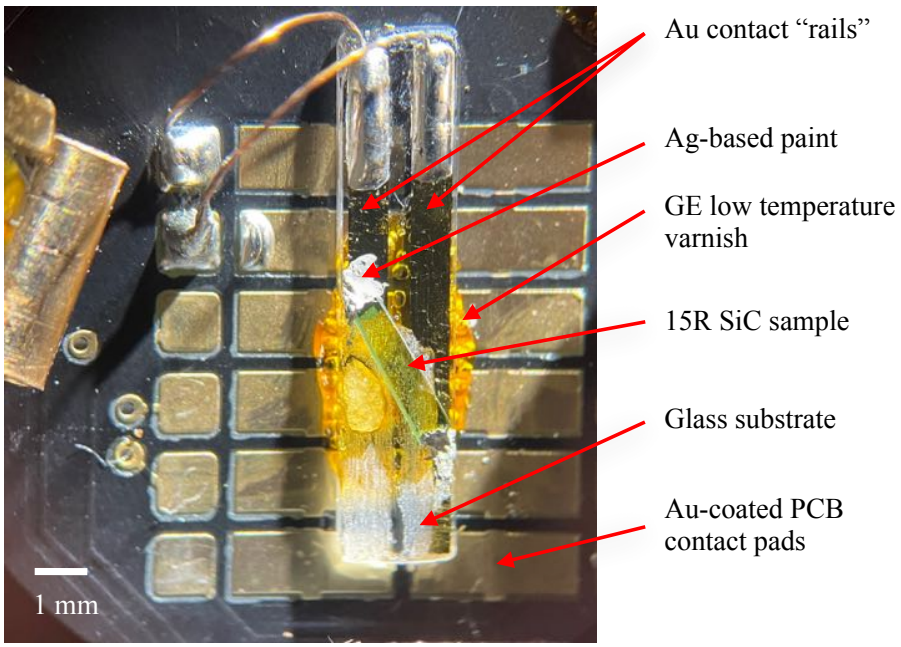

Figure 5.5: The photo of the top view of the prepared sample on the PCB. The width of the glass substrate is 2 mm. The dimensions of the 15R SiC sample is 3.5 mm x 0.8 mm x 0.4 mm.

In our setup we can place the sample directly onto the PCB board or replace it with the custom PCB with exact diameter of 36 mm. In the case of using our PCB board, we can place the sample on the surface with certain kinds of non-conductive adhesives [Fig. 5.5]. Depending on the sample's dimensions, the vacuum grease can be used to hold the light-weight samples on the PCB's surface. If the sample is flat (thin film, etc.) - we can use either the Kapton®Tape (DuPont de Nemours, Inc., Kapton®Tapes, Torrance, CA, U.S.) or the GE Low Temperature Varnish (Von Roll USA, Inc., NY, U.S.).

Concerning the EDMR signal and its stability, it is directly dependent on proper sample contacting when exposed to cryogenic temperatures and high magnetic fields. The choice of contact type must be approached carefully depending on the sample itself, taking into account mentioned above conditions. The best way to contact the sample is wire bonding with Au or Al wire which are 'EPR-silent' materials. When the sample does not have deposited contact pads, one of the best solutions is to use conductive adhesive. We experimented with various conductive adhesives, and some of the carbon-based ones may introduce an unwanted EPR signal. As a result, we used the Ag-based paint, which

demonstrated that it can be used even at liquid helium temperatures and provides excellent contact. In this work the 15R SiC monocrystal was attached via Ag-based paint to the glass plate with spattered gold contact pads, which, in turn, were connected to the PCB board[1]. All signal wires connect to the signal terminal, which also houses contacts for dedicated sensors.

5.3.2. Light beam alignment determination

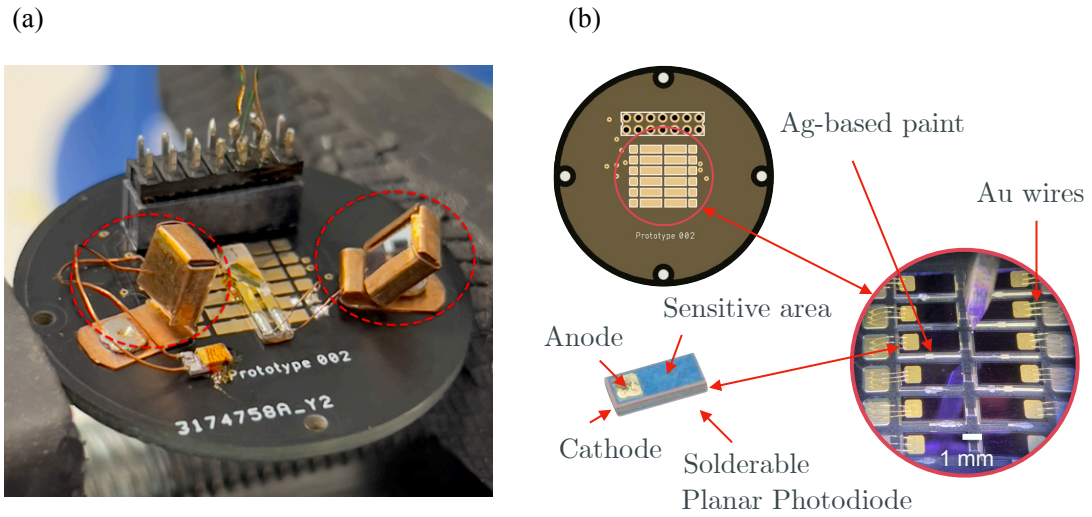

Figure 5.6: (a) – The photo of the attachable PCB board with the sample and the mirrors. Red circles are indicating the bronze mirror holders. (b) – Printed circuit board with attached planar photodiodes as a beam calibration sensor.

To propagate the light beam inside the sample holder, we use a multimodal optical fiber FT400EMT (Thorlabs, Inc., Newton, NJ, USA) that is connected to a collimator 300051 (World Precision Instruments Inc., Sarasota, FL, USA) as it was mentioned earlier. The beam of light from the collimator goes to the 5 mm square UV enhanced aluminum coated, $\lambda/10$ mirrors (Edmund Optics Inc., Barrington, NJ, USA), which, in turn, direct this beam to the sample. The mirror holders [Fig. 5.6 (a)] were made from 200 μm phosphor-bronze sheet and manually adjusted to the point of light reaching the sample. This configuration allows to manually adjust the location of the light spot on the sample based on its height or to illuminate a specific part of the sample.

To make sure the beam does not deviate under extreme conditions (up to $T = 3$ K and $B = 16$ T) after the calibration was done, we have created a specific sensor [Fig. 5.6 (b)] that can allow us to determine the exact position of the beam spot in the working conditions.

[1] As the glass substrate was a part of the sample holder for the X-Band, when EDMR was measured on this sample, it was contacted in this particular manner to ensure the most precise sample position and position of the Ag paint contacts for THz EDMR measurements.

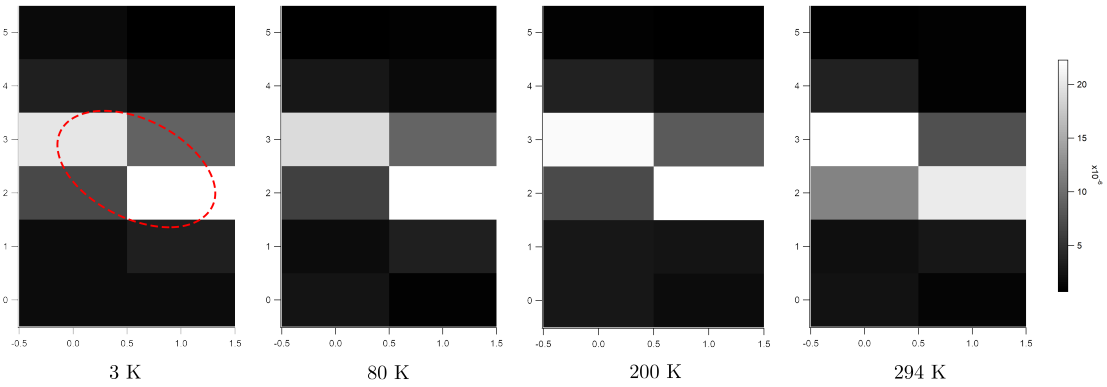

Figure 5.7: Image plots represent the position of the beam shone on photodiode array at different temperatures. White color shows the maximum light intensity. The red circle represents the approximate position of the light spot. The size of the spot is approximately 2 x 3 mm.

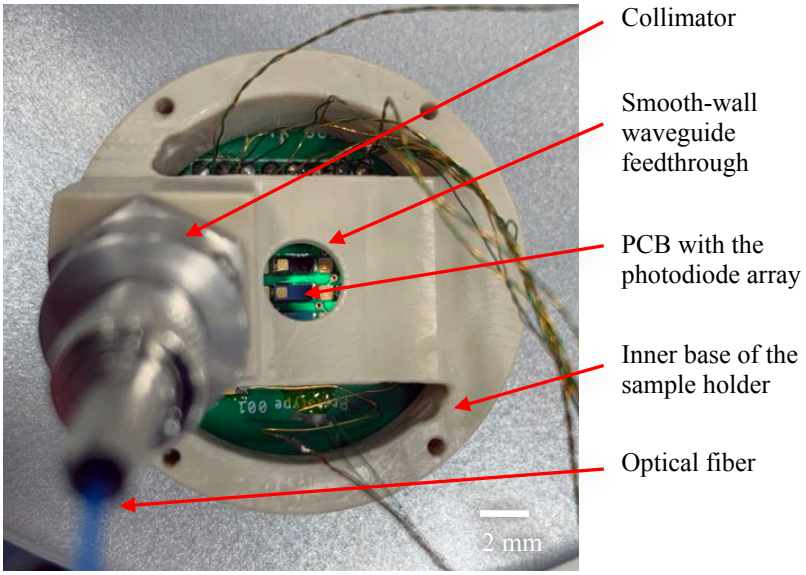

Figure 5.8: The photo of the inner base of the THz EDMR sample holder during the optical system calibration. The first prototype of the planar photodiode array is on the PCB.

The sensor consists of the printed circuit board (PCB) that repeats exact dimensions for a PCB of the sample holder. In the sensor we used SLCD-61N8 soldareble planar photodiodes (Advanced Photonix, Camarillo, CA, USA) arranged in the 6 x 2 array. The cathode side is attached to the PCB via Ag-based paint and the anodes were wirebonded with Au wire.

We created a program in LabView that reads out the current value of each of the photodiodes. In this program, we reproduced the location of the photodiodes in the array, assigning white color as the maximum light intensity and black as the absence of

light. During the cool down and warm up process of the VTI sapce we recorded the representation of the maximum light intensity position on each photodiode, shown on the Fig. 5.7 for four different temperatures.

As we can see from the Fig. 5.7, there is no significant sight of light beam deviation was found. Thus, this configuration can be used down to 3 K.

5.3.3. Microwave losses

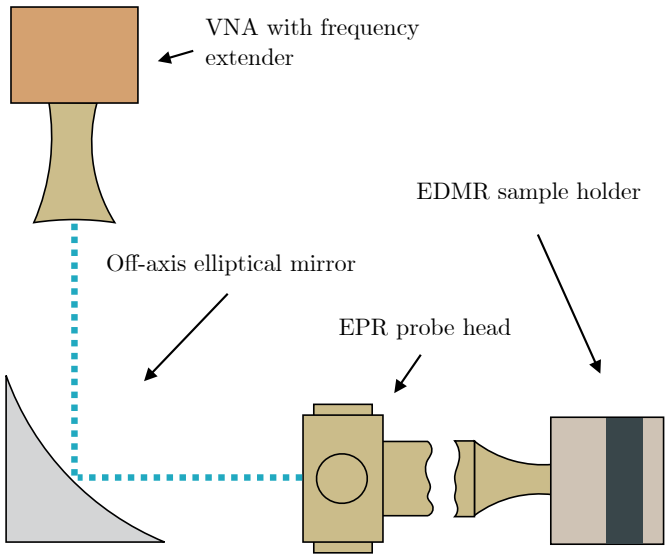

Figure 5.9: Microwave losses measurement scheme layout for the THz EDMR sample holder using 26.5 GHz VNA (R&S®ZNA26, Rohde&Schwarz, Germany) and a 325–500 GHz frequency extender (R&S®ZC500, Rohde&Schwarz, Germany). The dashed line indicates the m.w. beam.

A vector network analyzer (VNA) is a testing tool that characterizes the radio-frequency (RF) performance of microwave devices using network scattering characteristics, also known as S-parameters [109]. We performed the VNA measurements of the reflection parameter S_{11} using a 26.5 GHz Vector Network Analyzer (R&S®ZNA26, Rohde&Schwarz, Germany) with a 325–500 GHz frequency extender (R&S®ZC500, Rohde&Schwarz, Germany) [Fig. 5.9]. The experiment consist of two steps: (1) – measurement of the reference m.w. reflection from the EPR probe terminated with the mirror at the end of the corrugated waveguide, and (2) – measurement of the m.w. reflection from the THz EDMR sample holder attached to the EPR probe. Fig. 5.10 depicts the S_{11} parameter in dB of the THz EDMR sample holder (2) normalized by the reference m.w. reflection.

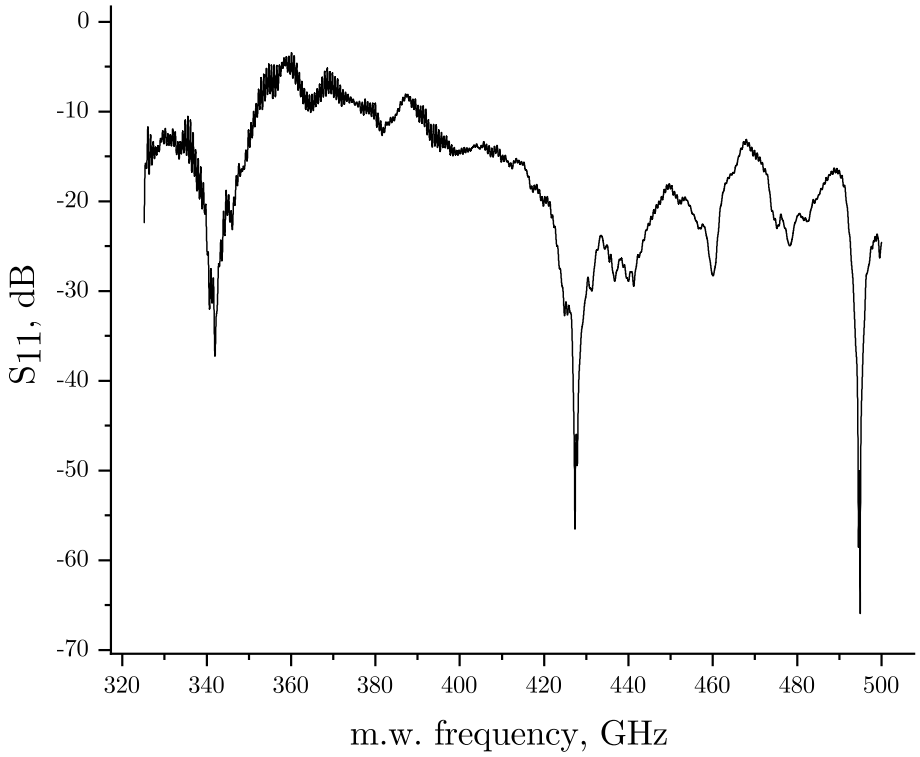

Figure 5.10: Microwave losses in the THz EDMR sample holder measured via 26.5 GHz Vector Network Analyzer (R&S®ZNA26, Rohde&Schwarz, Germany).

5.3.4. Homebuilt optical fiber feedthrough

Exclusively for the EPR probe, that we use in our THz FraScan setup we needed to develop a custom optical fiber feedthrough, that, by required parameters, was not available commercially.

The reason for developing the custom solution is due to the particular design of the EPR probe head. The distance between the corrugated waveguide and the inner wall of the EPR probe head is less than 1 cm, which is less than a common optical fiber 'bent radius' (without armed coating) of 2.5 cm. We came up with the solution to place the optical fiber through the EPR probe head pocket with the tilt of 45° diagonally [Fig. 5.11 (c)], where the optical fiber can helix around the corrugated waveguide without significant bending. The body of the feedthrough was made of bronze. The mechanism of this device is next: the optical fiber is being put through the external screw [Fig. 5.11 - (b)], PTFE sleeve, and the internal screw and the whole system is being attached to the EPR probe. As we mentioned earlier, inside the magnet must remain the low vacuum environment (about 10 mbar) and, thus, all the connections going from the EPR probe must be sealed. Tightening the external screw, the mechanical pressure goes to the PTFE sleeve, which, in turn, squeezes the optical fiber (with the Silica shield, the diameter is around 0.7 mm) and the internal screw remains in the same position. Thereby, the tightened enough external screw provides compressed PTFE sleeve along with the optical fiber and such system

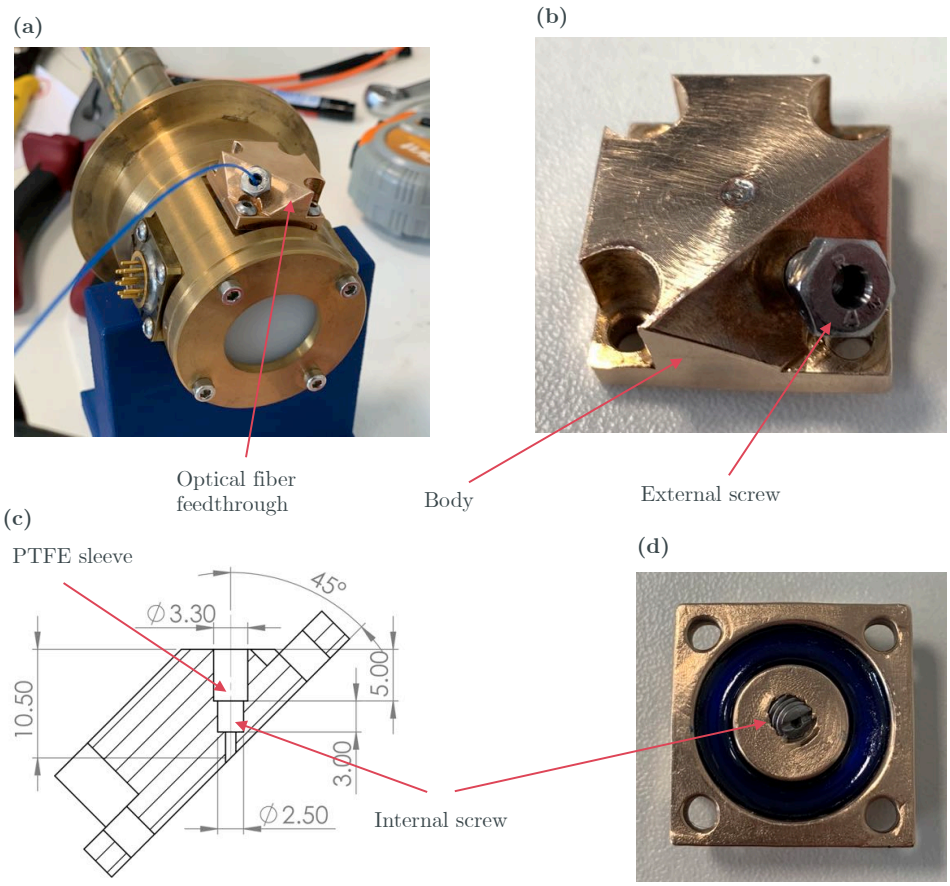

Figure 5.11: A homebuilt optical fiber feedthrough. (a) picture represents the feedthrough attached to the EPR probe. (d) represents the bottom side of the feedthrough.

can support vacuum of at least 10^{-4} mbars, which is more than sufficient for our vacuum environment. Before testing this system with actual EDMR experiment, we performed a leakage test, where the optical fiber was placed inside the optical fiber feedthrough and the external screw is tightened, the EPR probe is loaded inside the airlock. By monitoring the pressure indicator of the pump, which is pumping the air out of the airlock, we found that no trace of the air leakage or the pressure dropping were present.

5.4. EDMR Experiment

In this section, the detailed EDMR experiment using our THz FraScan spectrometer is described. Depending on the sample, we bare in mind the most efficient contacting method in order it to have a robust metal contact pad or a wire, which have to be connected to the PCB board. When the EPR probe is out of the magnet for the attaching sample holder procedure, we check the IV curve of the sample within the dedicated voltage range and make sure that the current corresponds to proper device working conditions. When the sample is placed onto PCB and contacted, the sensors (temperature and magnetic

field) are being attached. Using the attaching PCB screws [see Fig. 5.4], we fix the sample holder from the bottom. If the experiment requires the light excitation, the optical fiber has to be attached to the collimator's SMA thread. In order to be sure that the light covers the dedicated spot, we can power on any light source connected to another side of the optical fiber and monitor the light spot through the top center of the sample holder via smooth-wall waveguide (or prepare it when the inner base of the sample holder is disassembled [Fig. 5.8]). Adjusting the light spot spatially can be done by manual tilting the mirror holders. Once the sample is placed onto the PCB and all the wiring is connected, the sample holder is attached to the EPR probe. The EPR probe is placed inside the home-built airlock system, and to the magnet. In the LabView program we set the dedicated temperature and the magnetic field value.

From the signal terminals on the top of the EPR probe, we take a dedicated signal channel as a double-shielded BNC cable, which has to be connected to SR570 current preamplifier. Depending on the sample itself, the biasing option from the preamplifier can be chosen. The filtering option is used for cutting off unwanted frequency range from our channel and set around the modulation frequency for our signal. It should be noted, that the gain on SR570 is also set to the dedicated frequency region.

The signal output we connect to the MFLI-500 lock-in amplifier. It has an ability to acquire real-time fast Fourier transform (FFT) spectra of the input signal. It is recommended to check it, in order to be sure that the preferred modulation frequency range does not interfere with other equipment. In this work we used $f_{mod} = 771\,\text{Hz}$ with an amplitude of 2.5 G.

The magnetic field sweeping region we set in the LabView program as well as the m.w. frequency value [see Appendix (9)]. In the case of FD EDMR, we set the magnet to the persistent mode at the certain value and choose the dedicated frequency range.

5.5. Summary

As can be inferred from the preceding section, homemade systems can broaden the limits of the electrically detected magnetic resonance research technique. To summarize the EDMR setup parameters that have been demonstrated here and those that are, in principle, achievable in our spectrometer, we can refer to the Table 5.1.

The main advantages are:

- Scanned frequencies. Studies such as zero-field splitting and near-zero field magnetoresistance can be performed. The spectrum accumulation and averaging provides twice higher signal-to-noise ratio compared to measurements in the magnetic field domain for the same total acquisition time [see chapter 'Results obtained' 6] .

- High magnetic fields. With our system, it is possible to observe magnetic resonance at g = 2 up to 445 GHz, when the magnetic field maximum is 16 T.

Table 5.1: The comparison of demonstrated and possible specifications of developed THz EDMR setup.

Specification	**Demonstrated**	**Possible**
m.w. frequency range (GHz)	80 – 328	80 – 1100
Magnetic field range (T)	0 – 11.5	0 – 16
Sample diameter (mm)	3.5	36
Sample height (mm)	2	7
Temperature range (K)	3 – 300	1.8 – 300
Optical illumination (nm)	403 – 636.7	400 – 700
Bias voltage (V)	5	0.01 – 200
Magnetic field modulation amplitude (G)	2.5	0 – 10
Magnetic field modulation source	Single coil	Helmholtz coils, planar coil (on PCB)
Signal modulation type	Magnetic field	Magnetic field, m.w. frequency
Sample type	SiC monocrystals	Monocrystals, solar cells, MOSFETs, etc.
Measurement mode	CW (MD, FD, FFM)	CW (MD, FD, FFM), rapid scan

- Frequency-field maps. The potential to record spectra with magnetic field sweeps up to 16 T and frequencies between 80 and 1100 GHz is possible. Such research aids in the investigation of the frequency-dependent behavior of the sample and provides a comprehensive picture that can be utilized to determine the spin Hamiltonian parameters of high spin systems. Additionally, zero-field splitting acquisition is achievable in frequency domain mode.

- Optical illumination of the sample. In the approach described, light can be delivered on a sample via multimodal optical fiber using either broad-spectrum light sources or lasers with wavelengths ranging from 400 to 700 nm.

- Adjustable sample size up to 36 mm in diameter. By fabricating a dedicated printed circuit board as a sample plate with contact pads, we may place the entire 1 inch wafer with the functioning device on top.

- Temperature range between 1.8 K and 300 K. The advantage of our superconducting magnet system is that it can reach temperatures as low as 1.8 K, which enhances the study of the vital effects occurring at cryogenic temperatures.

Despite the numerous advantages of THz EDMR setup over the conventional existing ones, there are a few challenges remaining. The m.w. power for the source of 80–120 GHz

is 120 mW and the source of 325–330 GHz has an output m.w. power of 70 mW. The other set of m.w. sources range from 350 to 500 GHz and higher have power of several mW. The importance of the m.w. power in terms of EDMR systems using non-resonant probe approach will be discussed in the following chapter ('Results obtained' 6).

6. Results obtained

This chapter presents work based on already submitted article combining EPR and EDMR techniques applied in studies of 15R polytype of SiC highly nitrogen-doped monocrystal and the development of hardware instrumentation of novel THz EDMR setup based on the THz FraScan spectrometer, located in CEITEC BUT. The results herein presented as an extraction from submitted to *IEEE Transactions on Instrumentation and Measurement* manuscript titled 'Multifrequency Electrically Detected Magnetic Resonance Setup based on a sub-THz FraScan Spectrometer'. Additional insights from forthcoming publications are added.

6.1. Silicon Carbide

Natural occurrences of silicon carbide are exceptionally rare. However, the mineral moissanite [110], which contains silicon carbide, has been discovered in certain types of meteorites as well as corundum deposits. Thus, almost all of the silicon carbide on the market is artificially produced. The Lely method stands out among the various types of growth techniques as the one that can result in the production of single crystals of a high quality [111, 112]. Silicon carbide is subject to polytypism, in which the various crystal

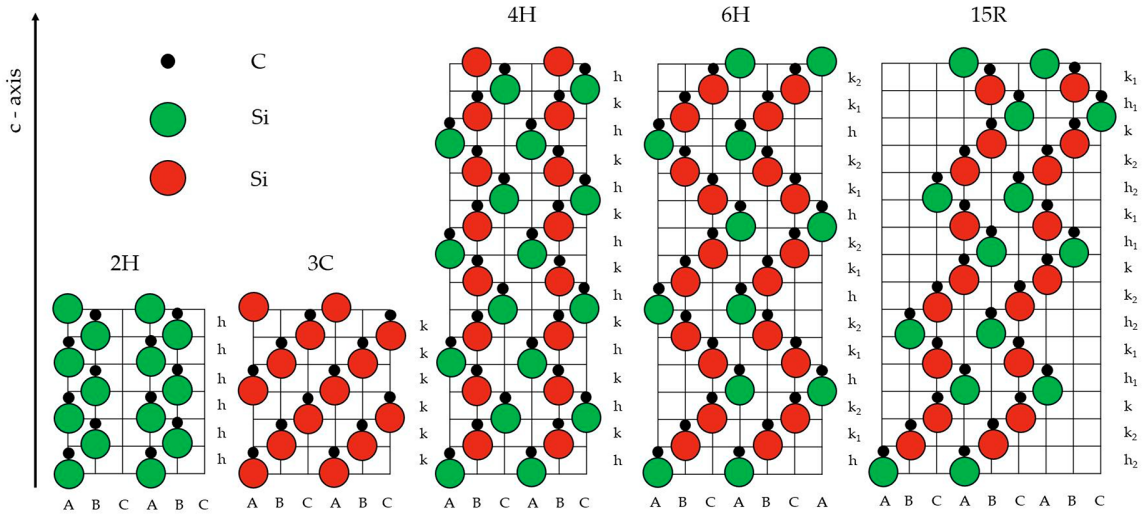

Figure 6.1: Diagram of the primitive cells of significant silicon carbide polytypes. Taken from [113].

structures are distinguished by varying stacking sequences of identical planes along the c-axis [114]. More than 250 distinct types of SiC materials have been discovered so far, however the crystal structures are only three: cubic (C), hexagonal (H) and rhombohedral (R) symmetry. The number 4 in 4H-SiC refers to the four double layers stacking in the primitive unit cell (ABACABAC) as shown in Fig. 6.1. The stacking sequences for different crystal symmetries are:

- 3C-SiC: ABC;
- 4H-SiC: ABAC;
- 6H-SiC: ABCACB;
- 15R-SiC: ABCACBCABACABCB.

More substantial theory on crystallography of SiC structures can be found elsewhere [115].

The properties of different silicon carbide polytypes vary, despite the fact that all of the polytypes have identical atomic composition. The monocrystal of pure silicon carbide is colorless; however, the strong doping with nitrogen (e.g., $(N_D - N_A) \approx 5{\cdot}10^{18}\,\mathrm{cm}^{-3}$) gives it a semi-transparent green-yellowish color. The darker it is, the greater the number of impurities (whether intentionally added or not) that are present. Concerning the electrical properties, in 3C-SiC the bandgap is about 2.3 eV, whereas the 4H-SiC has 3.2 eV. In terms of its mechanical characteristics, SiC has a Mohs hardness of approximately 9–9.5 points out of 10, whereas diamond gets 10. SiC does not melt at any achievable temperature. It cannot be dissolved by most of the acids, but can be etched via alkaline hydroxy bases at certain temperatures (higher than 600° C).

Regarding the applications of SiC, it is widely used and covers a substantial amount of purposes, such as the following:

- electric systems (as a high voltage application in the lightning arresters, preventing the lightning strike hitting the power line)[116–118];
- heating elements (the high temperature application; e.g., melting the glass; heat treatment of metals; production of ceramic components) [119, 120];
- electronic components (high power devices, high voltage MOSFETs (more than 1700 V), Schottky diodes, LEDs, etc.) [121–124].

SiC is also well-known for its employment in the graphene synthesis process, serving as a substrate on which epitaxial graphene can be grown. Moreover, the point defects in SiC can be utilized as a source of a single photons. Thus, this material has an application for the quantum technology [125–127].

6.2. Multifrequency EDMR studies on 15R SiC

In this section the results of 85 – 328.84 GHz EDMR experiments performed with the setup described in the previous chapter are presented. We have performed the low-temperature multi-frequency EPR and EDMR spectroscopy of 15R SiC monocrystal with donor concentration $(N_D - N_A) \approx 5 \cdot 10^{18}\,\mathrm{cm}^{-3}$. The monocrystal was grown by the modified Lely method [128]. Approximate sample dimensions are 3.5 mm x 0.8 mm x 0.4 mm.

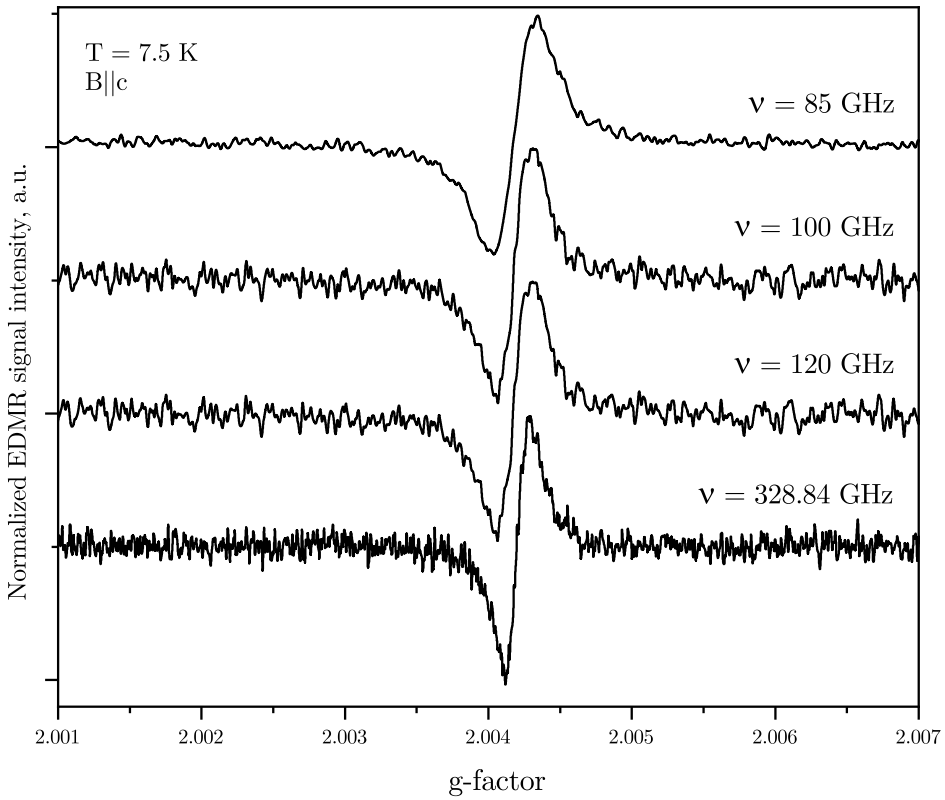

Figure 6.2: The EDMR spectra measured in 15R SiC monocrystal with $(N_D - N_A) \approx 5 \cdot 10^{18}\,\mathrm{cm}^{-3}$ at ν = 85 – 328.84 GHz, $B \| c$. The EDMR spectra were normalized to their maximum intensities.

The results of 85–328.84 GHz EDMR measurements of 15R SiC monocrystal are presented in Fig. 6.2. In this monocrystal with $(N_D - N_A) \approx 5 \cdot 10^{18}\,\mathrm{cm}^{-3}$ the single line (S-line) of the spin system with S = $\frac{1}{2}$ is present. The multifrequency measurements were made with a single spectrometer and two different m.w. sources. The extracted data of the signal-to-noise ratio from the spectra in Fig. 6.2 measured with the m.w. source of 85–120 GHz is about 42, whereas the 328.84 GHz source have 29. We assume, that this noticeable SNR difference is caused by m.w. sources power variation and the EDMR spectra broadening. The output power to frequency dependence varies between m.w. sources. For example, an 80–120 GHz m.w. source has the output power of 120 mW, whereas a 328.84 GHz source has only 70 mW at the measured frequency.

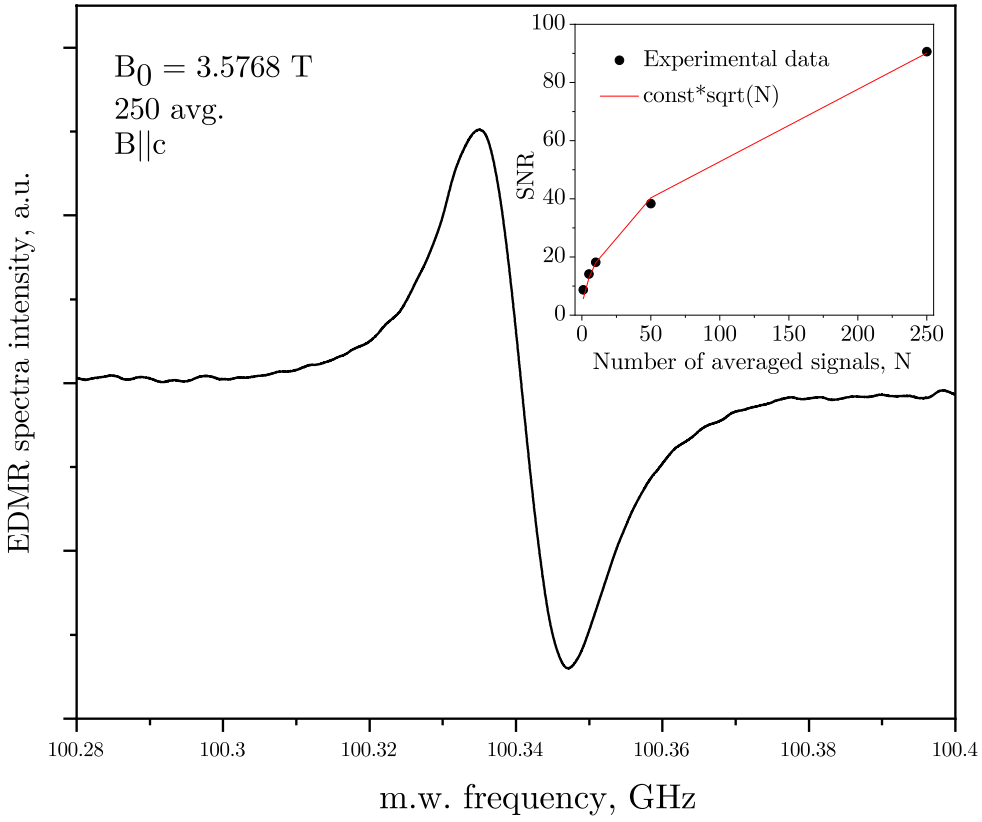

Figure 6.3: The frequency domain EDMR (FD EDMR) spectra measured in 15R SiC monocrystal with $(N_D - N_A) \approx 5 \cdot 10^{18}\,\mathrm{cm}^{-3}$ at $\nu = 100.28 - 100.4\,\mathrm{GHz}$, $B = 3.576891\,\mathrm{T}$ at $T = 7.5\,\mathrm{K}$, 250 averages, 2.048 seconds per sweep. The inner plot depicts the SNR to the number of averaged signals dependence. Acquisition of a single MD sweep takes about the same time as an accumulation of 250 FD sweeps.

In terms of frequency domain measurements, the THz FraScan setup can perform frequency sweeps while the magnetic field remains constant. The advantage of this technique is that it has a higher signal-to-noise ratio and requires less measurement time than the magnetic field sweep. Fig. 6.3 depicts the FD EDMR spectrum averaged 250 times with 2.048 seconds per sweep. The spectrum of 250 averages was recorded in $t \sim 8.5$ minutes, while the magnetic field domain measurement takes about the same amount of time with the single sweep and twice lower SNR. Performing the signal averaging of the magnetic field sweep EDMR spectra using superconducting magnets has certain disadvantages, such as the magnetic field shift and noticeable magnet inertia. To suppress the latest one, the stabilization delay time must be set before recording a new spectra and the magnetic field ramping rate (to sweep the magnetic field up and down) has to be the same. In the case of the frequency domain measurements the magnet is set to persistent mode on the desired magnetic field value.

Fig. 6.4 shows the m.w. power dependence of the EDMR signal intensity measured in 15R SiC monocrystal showing saturation above 40 mW. This power saturation effect takes place only when the incident m.w. power level is sufficient for populating the excited spin

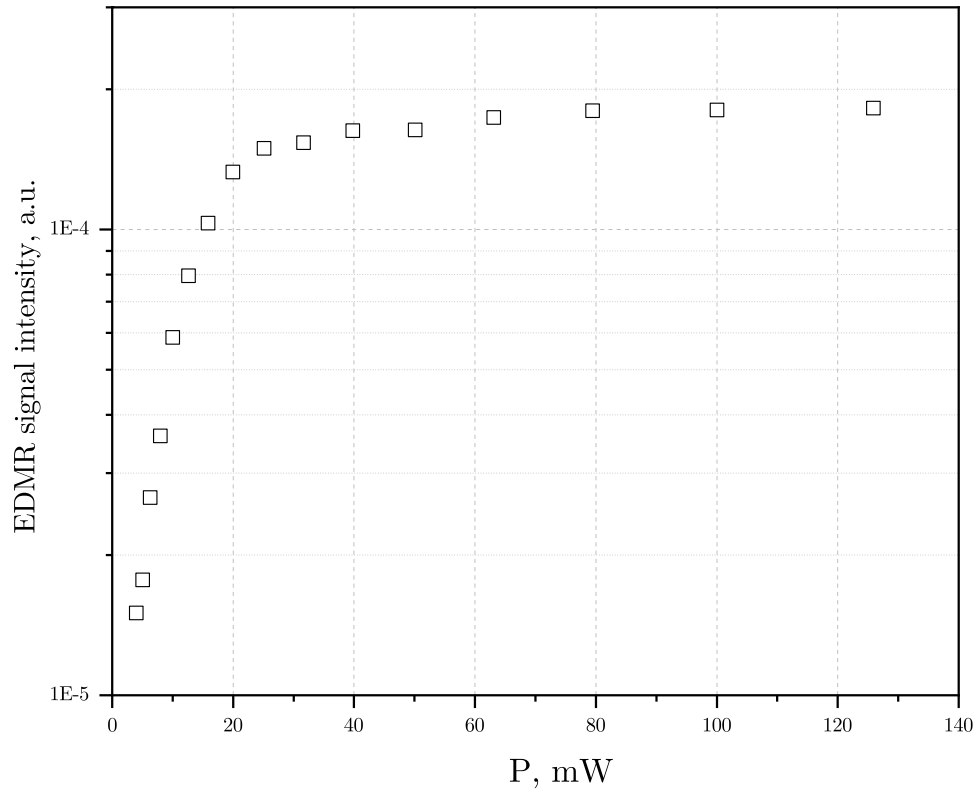

Figure 6.4: The m.w. power dependence of the EDMR signal intensity measured in 15R SiC monocrystal with $(N_D - N_A) \approx 5 \cdot 10^{18}\,\mathrm{cm}^{-3}$. $\nu = 100\,\mathrm{GHz}$, $T = 7.5\,\mathrm{K}$.

state of the spin system much faster than the system relaxes to its equilibrium population state due to the spin-lattice relaxation effects [129]. We can assume that the optimal minimum m.w. power required in such setups with non-resonant probe configuration to measure the magnetic field sweep EDMR begins at 20 mW. It should be noted that the output power of the the higher frequency m.w. sources (above 330 GHz) in our setup is below few mW.

Fig. 6.5 demonstrates the temperature dependence of EDMR spectra measured in 15R SiC monocrystal at $\nu = 100\,\mathrm{GHz}$, showing that the EDMR spectra were observed at $T < 12\,\mathrm{K}$ only. In general, the temperature dependence of an EDMR signal can give an information about the sample's recombination mechanisms and durability. We can assume that signal disappears at $T > 12\,\mathrm{K}$ because the hopping exchange interaction between nitrogen donors decreases.

The EDMR measurements under light illumination with laser diodes of the 403–636.7 nm wavelength did not show any enhancement in the EDMR signal intensity.

It is well known that in 15R SiC nitrogen N donors substitute five non-equivalent positions: three quasi-cubic k_1, k_2 and k_3 (N_{k1}, N_{k2}, N_{k3}) and two hexagonal h_1 and h_2 (N_{h1}, N_{h2}) with donor energy levels in the band gap at $\sim 99\,\mathrm{meV}$ for $N_{k1,k2,k3}$ and ~ 52 meV for N_{h1}, h_2. As a result, the 15R SiC monocrystals with $(N_D - N_A) \approx 5 \cdot 10^{16}\,\mathrm{cm}^{-3}$ reveal five triplet lines in the EPR spectra due to hyperfine interaction with ^{14}N nuclei

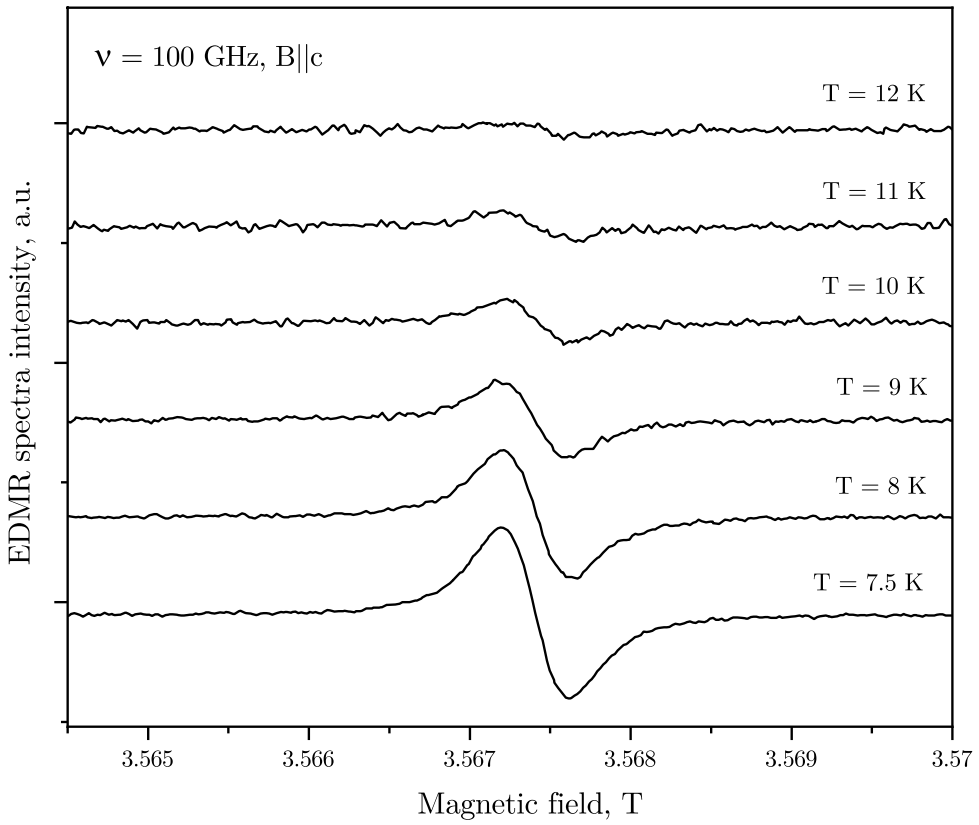

Figure 6.5: The temperature dependence of EDMR spectra measured in 15R SiC monocrystal with $(N_D - N_A) \approx 5 \cdot 10^{18}\,\mathrm{cm}^{-3}$ at $\nu = 100\,\mathrm{GHz}$.

($I = 1$, nat. ab. 99.6%) related to the center with $\mathrm{S} = \frac{1}{2}$ [130–132]. The isolated N donors in 15R SiC have the following spin Hamiltonian parameters [131, 132]:

- N_{k1} : $g_\perp = 2.0026(2)$, $g_\parallel = 2.0040(2)$, $A_{iso} = A_\parallel = A_\perp = 33.6\,\mathrm{MHz}$;
- N_{k2} : $g_\perp = 2.0030(2)$, $g_\parallel = 2.0037(2)$, $A_{iso} = 33.32\,\mathrm{MHz}$;
- N_{k3} : $g_\perp = 2.0030(2)$, $g_\parallel = 2.0038(2)$, $A_{iso} = 30.36\,\mathrm{MHz}$;
- N_{h1} : $g_\perp = 2.0028(2)$, $g_\parallel = 2.0035(2)$, $A_\perp \sim 1.1\,\mathrm{MHz}$, $A_\parallel \sim 2.1\,\mathrm{MHz}$;
- N_{h2} : $g_\perp = 2.0023(2)$, $g_\parallel = 2.0031(2)$, $A_\perp \sim 1.4\,\mathrm{MHz}$, $A_\parallel \sim 2.2\,\mathrm{MHz}$.

At $(N_D - N_A) \approx 5 \cdot 10^{18}\,\mathrm{cm}^{-3}$ the disappearance of $N_{h1,h2}$ donors having more shallow levels in the bandgap is expected along with the emergence of the single line due to exchange interaction between N donors.

From the EPR measurements at $\nu = 328.84\,\mathrm{GHz}$ in both orientations of the magnetic field with respect to the crystal c-axis, it was found that at $T < 20\,\mathrm{K}$, the 15R SiC samples reveal an intense line with $g_\perp = 2.0026(2)$, $g_\parallel = 2.0043(2)$ and a line triplet of low intensity due to $N_{k1,k2,k3}$ donors. The EDMR spectra measured at $\nu = 328.84\,\mathrm{GHz}$ and $T = 7.5\,\mathrm{K}$ show a similar single line with $g_\perp = 2.0026(2)$, $g_\parallel = 2.0043(2)$, and no traces of the N donors residing on the cubic sites were detected (see Fig. 6.6).

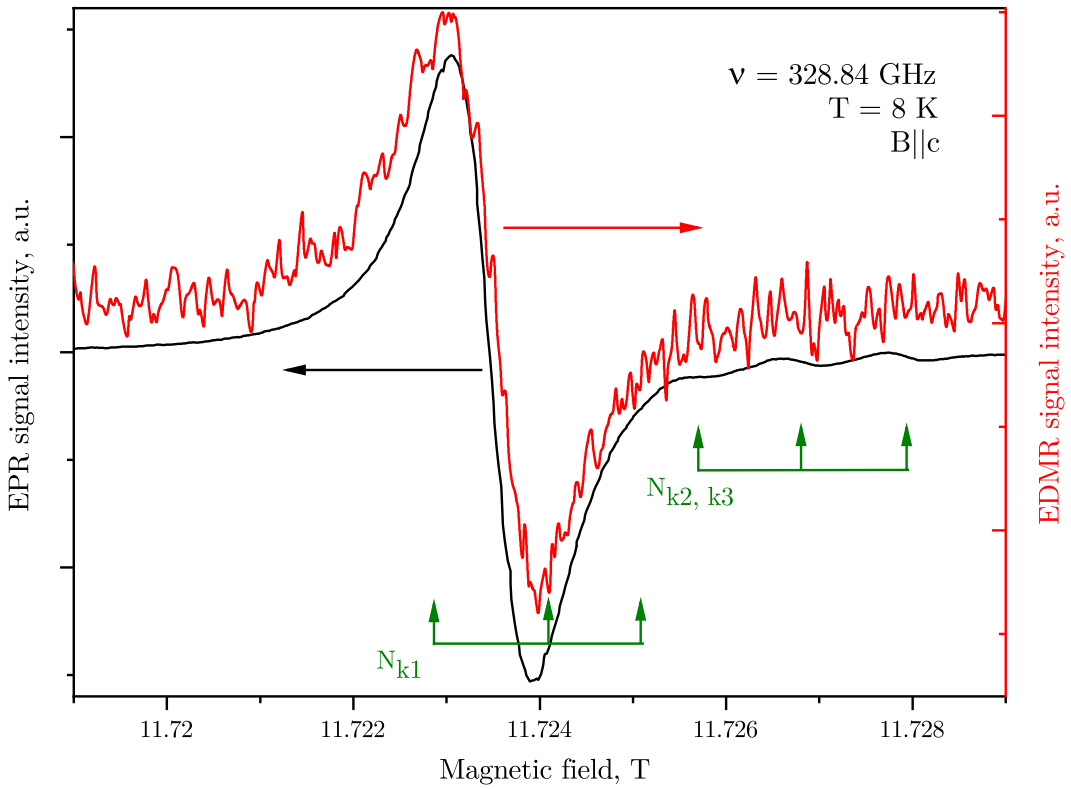

Figure 6.6: The EPR (solid black line) and EDMR (solid red line) spectra measured in 15R SiC monocrystal with $(N_D - N_A) \approx 5 \cdot 10^{18}\,\mathrm{cm}^{-3}$. $\nu = 328.84\,\mathrm{GHz}$, $T = 8\,\mathrm{K}$, $B \| c$. The EPR spectra were measured at $f_{mod} = 2.9\,\mathrm{KHz}$ and EDMR spectra at $f_{mod} = 771\,\mathrm{Hz}$, both at $B_{mod} = 2.5\,\mathrm{G}$.

In [133], the N atoms in the SiO_2–SiC interface regions of n-channel lateral 4H SiC metal-oxide-semiconductor field-effect transistors (MOSFETs) were studied by low-temperature EDMR. The authors reported an intense EDMR signal at $T < 20\,\mathrm{K}$ with C_{3V} symmetry having $g_\perp = 2.0008$, $g_\| = 2.0047$ assigned to N donors residing hexagonal site in 4H SiC (N_h). However, from an earlier pulsed electron-nuclear double resonance study of 4H SiC monocrystals with $(N_D - N_A) \approx 5 \cdot 10^{17}\,\mathrm{cm}^{-3}$ [134], it was unambiguously proved that N_h donors in 4H SiC have $g_\perp = 2.0006(1)$, $g_\| = 2.0065(1)$. At the same time, the high-field EPR study shows that no N_h line is observed in 4H SiC monocrystals with $(N_D - N_A) \approx 5 \cdot 10^{18}\,\mathrm{cm}^{-3}$, and the single line with $g_\perp = 2.0010(1)$, $g_\| = 2.0054(1)$ [135] caused by the hopping exchange of a donor electron between N atoms at hexagonal and cubic positions appears [136]. Therefore, the observed in [133] EDMR signal should be attributed to the hopping exchange interaction of N donors residing at h and k positions in 4H SiC.

We assume that the same hopping process between N donors is responsible for the appearance of the single line with $g_\perp = 2.0026(2)$, $g_\| = 2.0043(2)$ in EPR and EDMR spectra of 15R SiC monocrystal with $(N_D - N_A) \approx 5 \cdot 10^{18}\,\mathrm{cm}^{-3}$. Therefore, we may suppose that the observed single line in EPR and EDMR spectra is caused by a spin-dependent hop-

ping process due to the exchange interaction of N_{k1} and N_{h1} in 15R SiC. Measuring the EDMR spectra in the wide m.w. frequency range from 85 GHz to 328.84 GHz allowed us to determine that no overlapping lines were hidden in the spectrum [see Fig. 6.2].

At $T < 20\,\mathrm{K}$, a single EDMR signal associated with the S-line was detected [see Fig. 6.6], which was attributed to a spin-dependent hopping process generated by the exchange interaction between N donors lying in cubic and hexagonal locations in 15R SiC. Considering the g-factor value of this S-line, it could be the result of exchange interactions between N_{k1} and N_{h1} donors or N_{k1} and N_{k1} donors in 15R SiC.

This EDMR signal's intensity diminishes as the temperature rises. Fig. 6.7 depicts the influence of EDMR signal intensity on reciprocal temperature.

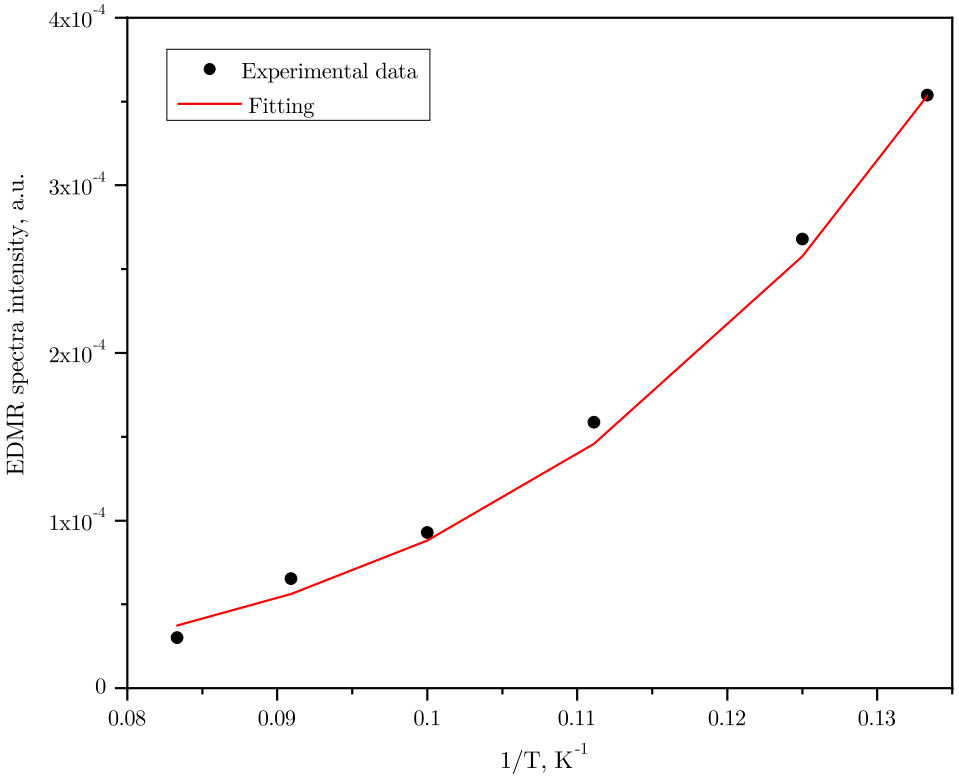

Figure 6.7: Temperature dependence of EDMR spectra intensity of S-line measured at $\nu = 100\,\mathrm{GHz}$, $B \parallel c$. The solid line is the result of the fitting with equation (6.4).

Following [75], the EPR-energy transfer mechanism corresponds to the presence of both singly occupied and doubly occupied states. In addition, a transition to an occupied state is only possible if the electron spins are antiparallel. In our 15R SiC samples, hopping occurs between N states that may be vacant or singly occupied.

On the opposite side of the spin-flip hopping mechanism, the relative decrease in resistivity is anticipated to be: $|\Delta\varrho_{EPR}/\varrho| \leq 10^{-2}$, whereas for the EPR energy transfer process, the relative decrease in resistivity should be: $|\Delta\varrho_{EPR}/\varrho| \leq -10^{-4}$. The measured spectra (not shown in the thesis) at $\nu = 9.702\,\mathrm{GHz}$ at $T = 7\,\mathrm{K}$ and applied voltage $U_s = = 3\,\mathrm{V}$ gives:

$$\frac{\Delta\varrho_{EPR}}{\varrho} = \frac{(\Delta U_s)_{EPR}}{U_s} = -4.1 \cdot 10^{-3}. \tag{6.1}$$

Hence, the EPR energy transfer process cannot be used to explain the EDMR signal found at low temperatures in 15R SiC samples.

Considering the m.w. absorption process that can occur at extremely low temperatures in the VRH regime that can lead to extra hopping in 6H SiC [32], the resulting energy separation between the occupied α site and the empty β site is equal to the energy of the photon: $\varepsilon_{\alpha\beta} = h\nu (\varepsilon_{\alpha\beta} \approx 3.89 \cdot 10^{-5}\,\text{eV}$ for $\nu = 9.4\,\text{GHz})$. The hopping probability of an electron jumping from a position α to a nearby position β can be expressed as a function of the distance between these positions ($R_{\alpha\beta}$) and their potential energy difference $\varepsilon_{\alpha\beta}$ [32, 137]:

$$W_{\alpha\beta}(R_{\alpha\beta}) = \nu_{ph} exp[-2\gamma R_{\alpha\beta} - \frac{\varepsilon_{\alpha\beta}}{k_B T}], \tag{6.2}$$

where ν_{ph} is the phonon distribution, $\gamma = 1/\gamma_B$ is the radius of the wavefunction of localization states. The case when $\varepsilon_{\alpha\beta}/k_B T << -2\gamma R_{\alpha\beta}$ corresponds to the nearest neighbour hopping (a carrier hops from one site to the next nearest, acquiring the necessary energy from a phonon along the way), when the case of $\varepsilon_{\alpha\beta}/k_B T > -2\gamma R_{\alpha\beta}$ corresponds to the VRH process occurred at the low temperatures.

In the VRH regime, it is known that the average energy distance $\varepsilon_{\alpha\beta}$ can be represented as [138]:

$$\varepsilon_{\alpha\beta} \approx (N(E_F) \cdot R_{\alpha\beta}^3 \cdot 4\pi/3)^{-1}, \tag{6.3}$$

where utilizing the estimated $N(E_F)$ value as $5.9 \cdot 10^{22}\,\text{eV}^{-1}\text{cm}^{-3}$ (for $\gamma_B = 13.9\,\text{Å}$) one can obtain the corresponding hopping distance as: $R_{\alpha\beta} \approx 47\,\text{Å} \sim 3 \cdot \gamma_B$.

Utilizing eq. (6.2), Fig. 6.8 depicts the theoretical dependency of the hopping probability $W_{\alpha\beta}$ on $R_{\alpha\beta}$ at $T = 20\,\text{K}$, 5 K and 1 K. At a hopping distance of $\sim 30\,\text{Å}$, the curve at $T = 1\,\text{K}$ corresponds to the highest value of $W_{\alpha\beta}$. We can therefore conclude that photon-induced hopping only contributes to the EDMR signal in our samples at temperatures below 1 K.

According to [32], the occurrence of EDMR spectra in the hopping regime may be due to the heating of the N donor electrons under EPR resonance conditions: the spin system absorbs m.w. energy, which is then transferred to the surroundings via spin-lattice relaxation, and the temperature of the crystal rises under resonance conditions. Therefore, if the m.w. energy is absorbed by the crystalline sample, it is transformed into heat, causing the sample's temperature to rise. In addition to the m.w. power absorbed, the specific heat must also be taken into account.

By applying the same method as in [32] for 6H SiC and assuming that the temperature dependence of the specific heat capacity for 15R SiC at low temperatures exposes the T^3

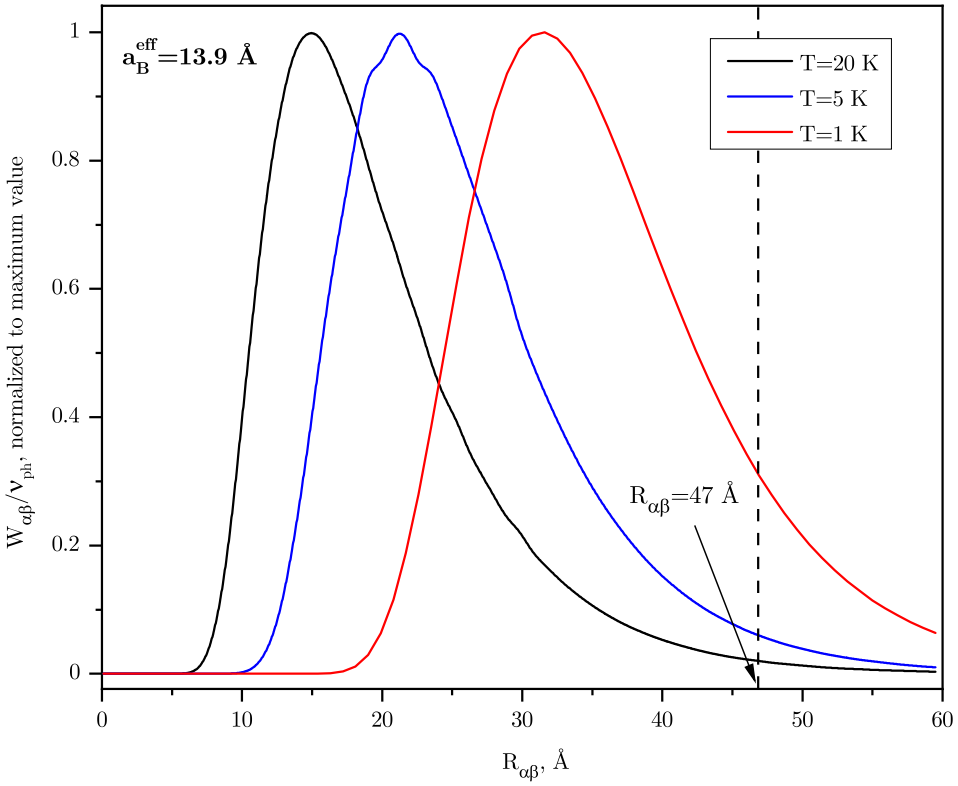

Figure 6.8: Theoretical estimation of hopping probability $W_{\alpha\beta}$ versus distance between donors $R_{\alpha\beta}$ at different temperatures ($T = 20\,\mathrm{K}$, $5\,\mathrm{K}$, and $1\,\mathrm{K}$) for 15R SiC monocrystal with $(N_D - N_A) \approx 5 \cdot 10^{18}\,\mathrm{cm}^{-3}$. The curves were normalized to their maximum value.

behavior [139], we can explain the observed temperature dependency of EDMR signal intensity in the VRH regime as [32]:

$$I_{EDMR} \propto T^{-17/4} exp((\frac{T_0}{T})^{1/4}). \tag{6.4}$$

Using eq. (6.4) and the T_0 value of 1.7 meV, we got a good agreement between the experimental results depicted in Fig. 6.7.

The EDMR signal amplitude increases linearly up to 25 mW and remains stable at higher m.w. power levels, as seen in Fig. 6.4. This behavior is compatible with an energy-transfer mechanism and a heating effect.

Similar to 6H SiC [32], it can be assumed that the EPR-induced temperature increase mechanism is responsible for the development of the EDMR signal in the VRH regime in 15R SiC monocrystals [see Fig. 3.16].

6.3. Summary

In this chapter we showed the proof of concept of the EDMR setup based on the sub-THz FraScan spectrometer, its capabilities and advantages. Despite the exceeding advantages of performing EDMR on higher frequencies and magnetic fields, the non-resonant probe

setups have certain limitations. The advantages of using FD EDMR over MD EDMR result in higher SNR and lower measurement time. The setup expands the range of measurement possibilities and paves the way for performing comprehensive EDMR studies. As the test samples in this setup, we used the 15R SiC monocrystal with a relatively high donors concentration $(N_D - N_A) \approx 5 \cdot 10^{18}\,\mathrm{cm}^{-3}$, which revealed a single EPR and EDMR line at a low temperature with $g_\perp = 2.0026(2)$, $g_\parallel = 2.0043(2)$. This signal is, most probably, caused by a spin-dependent hopping process due to the exchange interaction of nitrogen donors residing on cubic k_1 and hexagonal h_1 non-equivalent positions in the 15R SiC lattice.

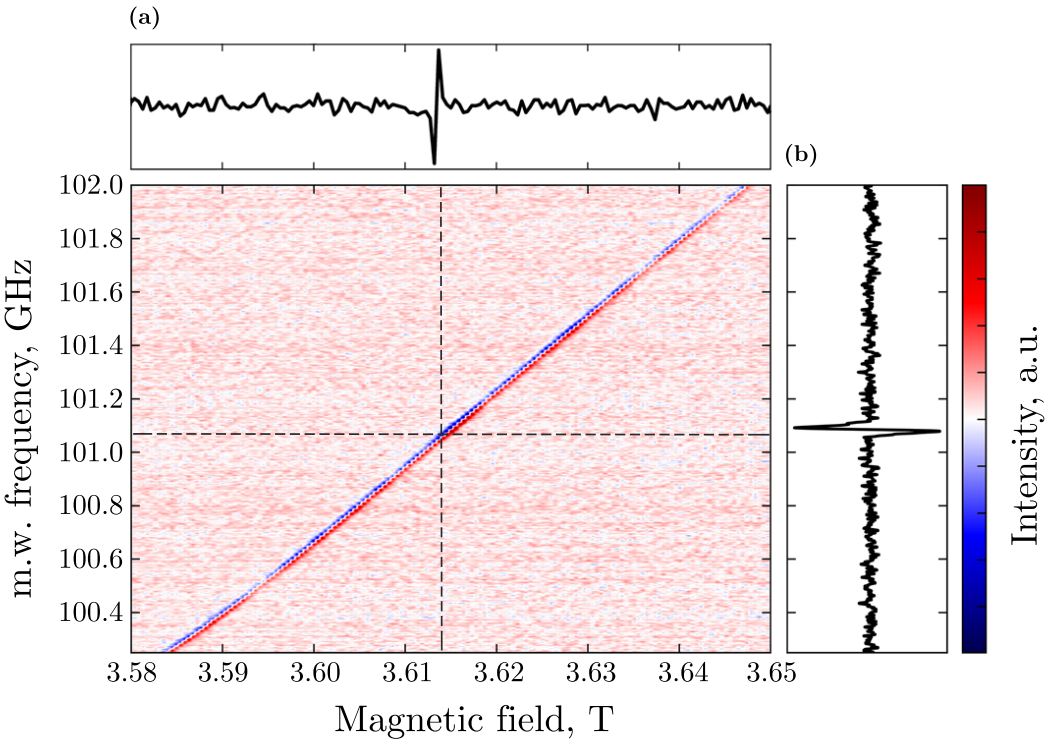

Figure 6.9: The frequency-field map of EDMR spectra measured in 15R SiC monocrystal with $(N_D - N_A) \approx 5 \cdot 10^{18}\,\mathrm{cm}^{-3}$ at $\nu = 100.2 - 102\,\mathrm{GHz}$, $B = 3.58 - 3.65\,\mathrm{T}$ and $T = 7.5\,\mathrm{K}$. Signal intensity values were omitted and shown in arbitrary units. The map resolution is 30 000 per 219 points. Dashed lines correspond to a frequency and a magnetic field value of (a) and (b) respectively. (a) – Single-frequency sweep spectra at $B = 3.615\,\mathrm{T}$. (b) – Single magnetic field sweep spectra at $\nu = 101.14\,\mathrm{GHz}$.

Regarding the prospects for the further EDMR technique development, we report on the first frequency-field EDMR map (FFM EDMR) spectra of 15R SiC monocrystal recorded at $\nu = 100.2 - 102\,\mathrm{GHz}$, $B = 3.58 - 3.65\,\mathrm{T}$ and $T = 7.5\,\mathrm{K}$ [Fig. 6.9]. The frequency sweep is 2.048 s long and the magnetic field sweep rate is $0.18\,\mathrm{mT/s}$. The map contains 30 000 frequency scan points for each of the 219 steps of the magnetic field sweep.

From Fig. 6.9 we can see the straight line across the map, the behavior of which can be described by eq. 3.1. Depending on the sample's defect complexity these two-dimensional

plots can qualitatively visualize recorded data in a wide range, helping to uniquely define the spin Hamiltonian parameters [52]. For instance, such plots can be useful when tracing the data of a frequency-dependent behavior of the sample's defect or evaluating the zero-field splitting.

Concerning this chapter, EDMR research on 15R SiC monocrystals utilizing a THz EDMR setup is proceeding and the results are being prepared for future publications.

7. Conclusions

The EDMR technique was successfully implemented in the THz FraScan spectrometer (located in CEITEC, Brno University of Technology, Czech Republic), to conclude the first aim acquired. The implementation procedure included the following steps:

- Fabrication of a custom sample holder that can accommodate samples with a diameter of up to 36 mm (10 mm x 10 mm x 3 mm, if the sample's light excitation is required with indicated in thesis working environment utilizing the signal terminal on top of the printed circuit board). The EDMR sample holder was manufactured from PEEK, a material commonly used in engineering. The sample holder was subjected to testing at temperatures as low as 3 K and magnetic fields up to 16 T, demonstrating its dependability in such harsh conditions. The sample holder is equipped with a 5 mm inner diameter smooth-wall waveguide, leaving a 5 mm m.w. aperture for the sample. The internal base of the sample holder consists of the optical fiber collimator holder, which transmits light to the broadband mirrors and, consequently, to the sample. The mirror holders are made of phosphorus-bronze sheet and can be angled and rotated for precise control of the light spot on the sample. This system's reliability has been demonstrated by the absence of a light spot alignment deviation during a 3 K – 300 K temperature change under the aforementioned extreme conditions.

- The problem with light propagation in the THz FraScan setup was resolved by utilizing multimodal optical fiber and designing custom optical fiber feedthrough (which was tested for vacuum pressures down to 10^{-4} mbar). The optical fiber feedthrough is built of a bronze body, an internal and external screws, and a PTFE nut positioned between them. The development of the custom optical fiber feedthrough was necessitated by the EPR probe head's specifications and the limited placement space for commercially available options.

- The detection scheme of the EDMR experiment on this setup was based on the phase-sensitive detection method, using the magnetic field modulation (produced by modulation coil of the THz EDMR sample holder). The biasing option (+5...-5 V) of the current preamplifier SR570 (Stanford Research Systems, CA, US) was used to apply the voltage to the sample. The output signal from SR570 was demodulated using the MLFI-500 (Zurich Instruments, Zurich, Switzerland) lock-in amplifier and recorded with home-written LabView software.

- Each essential component of the EDMR experiment was evaluated and calibrated using known samples with predetermined values.

To conclude the second aim acquired: the multifrequency EDMR study was carried out on a highly nitrogen-doped 15R SiC monocrystal with donor concentration $(N_D - N_A) \approx 5 \cdot 10^{18}\,\mathrm{cm}^{-3}$ as a proof-of-concept for our THz EDMR setup and to investigate each of its possibilities for performing EDMR at higher frequencies and magnetic fields. Particularly, the following measurements were done:

- The EDMR temperature dependence of 15R SiC was measured between 7.5 K and 12 K at 100 GHz, demonstrating that the single resonance line disappears at $T > 12\,\mathrm{K}$. Presumably, this may be caused by a decrease in the hopping exchange interaction between nitrogen donors. In general, the temperature dependence of an EDMR signal can reveal the recombination mechanisms occurring in the sample.

- The results of multifrequency EDMR measurements were obtained in this highly-doped monocrystal at the frequencies of 85–328.84 GHz. The resonance line originating from a spin $S = \frac{1}{2}$ system was detected. Even at the highest magnetic field of 11.7 T no splitting or shape distortion of the EDMR spectrum was observed. The EPR measurements at 328.84 GHz and $T = 7.5\,\mathrm{K}$ in both orientations (parallel and perpendicular to the c-axis of the monocrystal) revealed an intense single line with $g_\perp = 2.0026(2)$ and $g_\parallel = 2.0043(2)$ and a triplet line of low intensity attributable to $N_{k1,k2,k3}$ donors. The EDMR measurements at the same frequency and orientations revealed a similar single line with $g_\perp = 2.0026(2)$ and $g_\parallel = 2.0043(2)$, with no signs of N donors residing on the cubic sites.

- We hypothesize that the single line with $g_\perp = 2.0026(2)$, $g_\parallel = 2.0043(2)$ in the EPR and EDMR spectra of 15R SiC monocrystals with $(N_D - N_A) \approx 5 \cdot 10^{18}\,\mathrm{cm}^{-3}$ is the result of the hopping conduction process between N donors. The observed single line in EPR and EDMR spectra may therefore be attributed to a spin-dependent hopping mechanism resulting from the exchange contact between N_{k1} and N_{h1} in 15R SiC.

- The m.w. power dependence of the EDMR signal has been measured. Above 40 mW, the dependence indicates signal saturation. We can suppose that the minimum optimal power for such a non-resonant probe configuration to measure magnetic field sweep EDMR begins at 20 mW. It should be noted, that the 80 – 120GHz m.w. source has a power output of approximately 125 mW, whereas the m.w. power at the 328.84 GHz frequency is approximately 70 mW (due to different m.w. sources). In addition, the multipliers for frequencies above 330 GHz have even lower efficiency with the output power of several mW and lower.

- We demonstrated the possibility of measuring EDMR in the frequency domain. In our experiment, the duration of a single MD EDMR sweep was roughly ≈ 8.5 minutes.

We can perform FD EDMR with 250 averages in the same amount of time and with twice higher signal-to-noise ratio compared to the single sweep in magnetic field domain EDMR.

- We have obtained the first frequency-field EDMR map at $\nu = 100.2 - 102\,\mathrm{GHz}$, $B = = 3.58$ – $3.65\,\mathrm{T}$, and $T = 7.5\,\mathrm{K}$ as the most recent result. The magnetic field sweep rate was $0.18\,\mathrm{mT/s}$ and the frequency sweep duration was 2.048 seconds. The map includes 30 000 frequency scan points for each of the 219 magnetic field sweep steps. Depending on the defect complexity of the sample, these two-dimensional plots can qualitatively depict recorded data across a broad range, aiding in the definition of the spin Hamiltonian parameters. For example, such plots might be helpful while tracing the data of a frequency-dependent behavior of a sample's defect or examining the zero-field splitting.

To outline the future expansion of the THz EDMR system, we can list the advantages and difficulties experienced during this research. The ability to sweep the frequency (80–1100 GHz) over such a wide range is a significant advantage when tracing the frequency-dependent sample's behavior or performing rapid scan EPR. The capability to acquire frequency-field maps in the aforementioned range with magnetic fields up to 16 T offers a unique approach to investigate the 'big picture' in terms of EDMR for both known and unidentified samples in the temperature range of $300\,\mathrm{K}$ – $1.8\,\mathrm{K}$.

In terms of obstacles and limitations, we can emphasize the magnetic field sweep's disadvantages, such as magnet inertia, sweep lag, and magnetic field shift, which also are not unique to superconducting magnets. Using a sample with a well-known g-factor as a magnetic field calibration reference can be useful in the EPR spectrum acquisition. Thus, the magnetic field sweep can be acquired concurrently, and the magnetic field value can be determined with high precision. In the case of EDMR, the magnetic field sensor can be utilized in addition to the setting of the sweep rate (due to the magnet's hysteresis, the sweeping rate for recording the spectra and ramping the magnetic field up and down should be the same). In addition, this brings up the issue of MD EDMR signal accumulation. Due to the magnetic field shift, it is extremely difficult to obtain a suitable spectrum. However, to completely eliminate this issue, frequency domain EDMR can be used. The magnetic field value for the frequency sweep window calibration can be obtained by performing an EPR measurement on the reference sample. The magnetic field is then set to persistent mode, and the FD EDMR spectra can be obtained. The spectra are collected accurately in this scenario, and the measurement time is reduced, resulting in a greater signal-to-noise ratio.

Since EDMR is measured as a change in sample's current, it is essential to maintain a shielded, properly grounded, and consistent connection between the sample and other circuitry in the spectrometer so that the signal transmission line does not pick up unwanted noise or interference from other laboratory equipment.

Regarding the future of THz EDMR setup, the crystal rotator might be beneficial for EDMR measurements. With the crystal rotator the angular dependence can be acquired to get the g-tensor parameters. In addition, equipping the sample holder with a heater would improve the sample's temperature stability and the precision of measurements of temperature dependence. It can be readily installed on the underside of the PCB to increase thermal contact with the sample.

For the further outlook regarding the devices that could be possibly studied within THz EDMR setup, the most demanding devices under investigations are research solar cells. Following the limitations of the X-, Q- and W-band resonators dimensions for placing a working device can be challenging. However, the THz EDMR setup, described in this thesis, expands the volume for the sample due to non-resonant probe approach. Usually, the dimensions of a working area for research devices is around 1 mm x 1 mm. The expansion of the volume of an active research device under investigation would push the limits not only for the photovoltaic devices, but as well for the crystals. Cutting crystals of various materials for the dedicated space in the standardized resonator may be costly and challenging at times, because after separation, some may lose potential integrity and change intrinsic properties, particularly when subjected to high laser temperatures or damaged by saw vibrations.

In conclusion, taking into account the global electronics market expansion, the EDMR technique has many industrial applications, the details of which are obviously off-limits to the academic community.

8. References

1. APPLEYARD, R. Pioneers of Electrical Communication. *Electrical Communication* **6,** 63–77 (1927).
2. Hong, S. *Wireless: From Marconi's black-box to the audion* (MIT press, 2001).
3. Dieckmann, M. *The Problem of Tele-Vision* July 1909. doi:10 . 1038 / scientificamerican07241909-61supp.
4. Blanchard, Y. *Le radar, 1904-2004: Histoire d'un siècle d'innovations techniques et opérationnelles* (Ellipses, 2004).
5. Miao, G., Zander, J., Sung, K. W. & Slimane, S. B. *Fundamentals of mobile data networks* (Cambridge University Press, 2016).
6. Butler, J. *Wireless Networking in the Developing World: A Practical Guide to Planning and Building Low-cost Telecommunicaitons Infrastructure* (Limehouse Book Sprint Team, 2013).
7. Thomson, J. J. Discovery of the electron. *Philosophical Magazine* **44,** 93 (1897).
8. Fleming, J. A. *Memories of a scientific life* (Marshall, Morgan & Scott, 1934).
9. Hoddeson, L. The discovery of the point-contact transistor. *Historical Studies in the Physical Sciences* **12,** 41–76 (1981).
10. Papadopoulos, C. Solid-state electronic devices. *Undergraduate Lecture Notes in Physics, New York, NY: Springer New York* (2014).
11. Berlin, L. *The man behind the microchip: Robert Noyce and the invention of Silicon Valley* (Oxford University Press, 2005).
12. Desai, S. B., Madhvapathy, S. R., Sachid, A. B., Llinas, J. P., Wang, Q., Ahn, G. H., Pitner, G., Kim, M. J., Bokor, J., Hu, C., Wong, H.-S. P. & Javey, A. MoS₂ transistors with 1-nanometer gate lengths. *Science* **354,** 99–102. doi:10.1126/science.aah4698. eprint: https://www.science.org/doi/pdf/10.1126/science.aah4698 (2016).
13. Kumar, V., Yadav, S., Sandeep, D. N., Dhok, S. B., Barik, R. K. & Dubey, H. *5G Cellular: Concept, Research Work and Enabling Technologies* (eds Kolhe, M., Trivedi, M., Tiwari, S. & Singh, V.) International Conference on Data and Information Sciences (ICDIS), Indira Gandhi Natl Tribal Univ, Amarkantak, INDIA, NOV 14-18, 2017, 327–338. doi:10.1007/978-981-13-0277-0_27 (2019).

14. FOLL, H. *et al.* AGGLOMERATE VON ZWISCHENGITTERATOMEN (SWIRL-DEFEKTE) IN SILIZIUM IHRE BEDEUTUNG FUER GRUNDLAGEN-FORSCHUNG UND TECHNOLOGIE. (1976).

15. Kittel, C. *Solid state physics* (Shell Development Company, 1955).

16. Spaeth, J.-M., Niklas, J. R. & Bartram, R. H. *Structural Analysis of Point Defects in Solids* 375. ISBN: 978-3-642-84407-2. doi:10.1007/978-3-642-84405-8 (Springer Berlin Heidelberg, Berlin, Heidelberg, 1992).

17. *Best Research-Cell Efficiency Chart* https://www.nrel.gov/pv/cell-efficiency.html.

18. Akhtar, W., Schnegg, A., Veber, S., Meier, C., Fehr, M. & Lips, K. CW and pulsed electrically detected magnetic resonance spectroscopy at 263 GHz/12 T on operating amorphous silicon solar cells. *Journal of Magnetic Resonance* **257,** 94–101. ISSN: 1090-7807. doi:https://doi.org/10.1016/j.jmr.2015.05.012 (2015).

19. Kelly, A. & Knowles, K. M. *Crystallography and crystal defects* (John Wiley & Sons, 2020).

20. Schmidt, J. & Solomon, I. Modulation de la photoconductivité dans le silicium á basse température par résonance magnetique électronique des impuretés peu profondes. *Compt. Rend.* **169,** 263 (1966).

21. Wertz, J. E. & Bolton, J. R. in *Electron Spin Resonance* 378–390 (Springer, 1986).

22. Song, L., Liu, Z., Kaur, P., Esquiaqui, J. M., Hunter, R. I., Hill, S., Smith, G. M. & Fanucci, G. E. Toward increased concentration sensitivity for continuous wave EPR investigations of spin-labeled biological macromolecules at high fields. *JOURNAL OF MAGNETIC RESONANCE* **265,** 188–196. ISSN: 1090-7807. doi:10.1016/j.jmr.2016.02.007 (2016).

23. Chauhan, S. K., Kumar, R., Nadanasabapathy, S. & Bawa, A. Detection Methods for Irradiated Foods. *Comprehensive Reviews in Food Science and Food Safety* **8,** 4–16. doi:https://doi.org/10.1111/j.1541-4337.2008.00063.x. eprint: https://ift.onlinelibrary.wiley.com/doi/pdf/10.1111/j.1541-4337.2008.00063.x (2009).

24. Callens, F., Vanhaelewyn, G., Matthys, P. & Boesman, E. EPR of carbonate derived radicals: Applications in dosimetry, dating and detection of irradiated food. *APPLIED MAGNETIC RESONANCE* **14,** 235–254. ISSN: 0937-9347. doi:10.1007/BF03161892 (1998).

25. Polovka, M., Brezova, V. & Stasko, A. Antioxidant properties of tea investigated by EPR spectroscopy. *BIOPHYSICAL CHEMISTRY* **106,** 39–56. ISSN: 0301-4622. doi:10.1016/S0301-4622(03)00159-5 (2003).

26. Regulla, D. ESR spectrometry: a future-oriented tool for dosimetry and dating. *APPLIED RADIATION AND ISOTOPES* **62.** 6th International Symposium on ESR Dosimetry and Applications, Campos do Jordao, BRAZIL, OCT 12-16, 2003, 117–127. ISSN: 0969-8043. doi:10.1016/j.apradiso.2004.08.030 (2005).

27. Zoleo, A., Bortolussi, C. & Brustolon, M. Echo detected EPR as a tool for detecting radiation-induced defect signals in pottery. *RADIATION MEASUREMENTS* **46,** 676–679. ISSN: 1350-4487. doi:10.1016/j.radmeas.2011.06.012 (2011).

28. Falk, A. L., Buckley, B. B., Calusine, G., Koehl, W. F., Dobrovitski, V. V., Politi, A., Zorman, C. A., Feng, P. X. .-L. & Awschalom, D. D. Polytype control of spin qubits in silicon carbide. *NATURE COMMUNICATIONS* **4.** ISSN: 2041-1723. doi:10.1038/ncomms2854 (2013).

29. Atzori, M., Tesi, L., Morra, E., Chiesa, M., Sorace, L. & Sessoli, R. Room-Temperature Quantum Coherence and Rabi Oscillations in Vanadyl Phthalocyanine: Toward Multifunctional Molecular Spin Qubits. *JOURNAL OF THE AMERICAN CHEMICAL SOCIETY* **138,** 2154–2157. ISSN: 0002-7863. doi:10.1021/jacs.5b13408 (2016).

30. Martinez-Perez, M. J., Cardona-Serra, S., Schlegel, C., Moro, F., Alonso, P. J., Prima-Garcia, H., Clemente-Juan, J. M., Evangelisti, M., Gaita-Arino, A., Sese, J., van Slageren, J., Coronado, E. & Luis, F. Gd-Based Single-Ion Magnets with Tunable Magnetic Anisotropy: Molecular Design of Spin Qubits. *PHYSICAL REVIEW LETTERS* **108.** ISSN: 0031-9007. doi:10.1103/PhysRevLett.108.247213 (2012).

31. Kawachi, G., Graeff, C. F. O., Brandt, M. S. & Stutzmann, M. Carrier transport in amorphous silicon-based thin-film transistors studied by spin-dependent transport. *Phys. Rev. B* **54,** 7957–7964. doi:10.1103/PhysRevB.54.7957 (11 1996).

32. Grasa Molina, M. I. *EPR-induced charge transport in highly doped crystalline n-type silicone carbide* PhD thesis (Univ. Diss., 2020).

33. Xiao, M., Martin, I., Yablonovitch, E. & Jiang, H. W. Electrical detection of the spin resonance of a single electron in a silicon field-effect transistor. *Nature* **430,** 435–439. ISSN: 1476-4687. doi:10.1038/nature02727 (2004).

34. Meier, C., Behrends, J., Teutloff, C., Astakhov, O., Schnegg, A., Lips, K. & Bittl, R. Multi-frequency EDMR applied to microcrystalline thin-film silicon solar cells. *Journal of Magnetic Resonance* **234,** 1–9. ISSN: 1090-7807. doi:https://doi.org/10.1016/j.jmr.2013.06.002 (2013).

35. Schnegg, A., Behrends, J., Fehr, M. & Lips, K. Pulsed electrically detected magnetic resonance for thin film silicon and organic solar cells. *Phys. Chem. Chem. Phys.* **14,** 14418–14438. doi:10.1039/C2CP41258F (42 2012).

36. McCrory, D. J., Anders, M. A., Ryan, J. T., Shrestha, P. R., Cheung, K. P., Lenahan, P. M. & Campbell, J. P. Slow- and rapid-scan frequency-swept electrically detected magnetic resonance of MOSFETs with a non-resonant microwave probe within a semiconductor wafer-probing station. *Review of Scientific Instruments* **90,** 014708. doi:10.1063/1.5053665. eprint: https://doi.org/10.1063/1.5053665 (2019).

37. Sharov, F. V., Moxim, S. J., Haase, G. S., Hughart, D. R. & Lenahan, P. M. A Comparison of Radiation-Induced and High-Field Electrically Stress-Induced Interface Defects in Si/SiO_2 MOSFETs via Electrically Detected Magnetic Resonance. *IEEE Transactions on Nuclear Science* **69,** 208–215. doi:10.1109/TNS.2022.3150979 (2022).

38. Ashton, J. P., Manning, B. R., Barker, W. R. & Lenahan, P. M. Ultra-low field frequency-swept electrically detected magnetic resonance. *Journal of Applied Physics* **129,** 083903. doi:10.1063/5.0042484. eprint: https://doi.org/10.1063/5.0042484 (2021).

39. Cochrane, C. J., Anders, M., Mutch, M. & Lenahan, P. *Quanitative Electrically Detected Magnetic Resonance for Device Reliability Studies* in *2014 IEEE INTERNATIONAL INTEGRATED RELIABILITY WORKSHOP FINAL REPORT (IIRW)* IEEE International Integrated Reliability Workshop (IIRW), S Lake Tahoe, CA, OCT 12-16, 2014 (2014), 6–9. ISBN: 978-1-4799-7274-6.

40. Myers, K. J., Lenahan, P. M., Bittel, B. C. & Meric, I. *Exploring Negative Bias Temperature Instability in Tri-Gate MOSFETs Through Electrically Detected Magnetic Resonance* in *2019 IEEE INTERNATIONAL INTEGRATED RELIABILITY WORKSHOP (IIRW)* IEEE International Integrated Reliability Workshop (IIRW), CA, OCT 13-17, 2019 (2019), 114–117. ISBN: 978-1-7281-2203-8.

41. Stegner, A. R., Boehme, C., Huebl, H., Stutzmann, M., Lips, K. & Brandt, M. S. Electrical detection of coherent ^{31}P spin quantum states. *Nature Physics* **2,** 835–838. ISSN: 1745-2481. doi:10.1038/nphys465 (2006).

42. Morishita, H., Abe, E., Akhtar, W., Vlasenko, L. S., Fujimoto, A., Sawano, K., Shiraki, Y., Dreher, L., Riemann, H., Abrosimov, N. V., Becker, P., Pohl, H.-J., Thewalt, M. L. W., Brandt, M. S. & Itoh, K. M. Linewidth of Low-Field Electrically Detected Magnetic Resonance of Phosphorus in Isotopically Controlled Silicon. *Applied Physics Express* **4,** 021302. doi:10.1143/apex.4.021302 (2011).

43. McCamey, D. R., Tol, J. V., Morley, G. W. & Boehme, C. Electronic Spin Storage in an Electrically Readable Nuclear Spin Memory with a Lifetime > 100 Seconds. *Science* **330,** 1652–1656. doi:10.1126/science.1197931. eprint: https://www.science.org/doi/pdf/10.1126/science.1197931 (2010).

44. Liu, X., Popli, H., Kwon, O., Malissa, H., Pan, X., Park, B., Choi, B., Kim, S., Ehrenfreund, E., Boehme, C. & Vardeny, Z. V. Isotope Effect in the Magneto-Optoelectronic Response of Organic Light-Emitting Diodes Based on Donor–Acceptor Exciplexes. *Advanced Materials* **32,** 2004421. doi:https://doi.org/10.1002/adma.202004421. eprint: https://onlinelibrary.wiley.com/doi/pdf/10.1002/adma.202004421 (2020).

45. Hatanaka, S. & Kanemoto, K. Probing electron-hole pairs in polymer light emitting diodes using electrically- and electroluminescence-detected magnetic resonance techniques. *POLYHEDRON* **136.** 15th International Conference on Molecule-Based Magnets (ICMM), Sendai, JAPAN, SEP 04-08, 2016, 58–60. ISSN: 0277-5387. doi:10.1016/j.poly.2017.02.032 (2017).

46. Thorne, A. P., 5 (Springer, 1988).

47. Bloos, D., Kunc, J., Kaeswurm, L., Myers-Ward, R. L., Daniels, K., DeJarld, M., Nath, A., van Slageren, J., Gaskill, D. K. & Neugebauer, P. Contactless millimeter wave method for quality assessment of large area graphene. *2D Materials* **6,** 035028. doi:10.1088/2053-1583/ab1d7e (2019).

48. Laguta, O., Sojka, A., Marko, A. & Neugebauer, P. Rapid scan ESR: A versatile tool for the spin relaxation studies at (sub)THz frequencies. *Applied Physics Letters* **120,** 120502. doi:10.1063/5.0083010. eprint: https://doi.org/10.1063/5.0083010 (2022).

49. Laguta, O., Tuček, M., van Slageren, J. & Neugebauer, P. Multi-frequency rapid-scan HFEPR. *Journal of Magnetic Resonance* **296,** 138–142. ISSN: 1090-7807. doi:https://doi.org/10.1016/j.jmr.2018.09.005 (2018).

50. Schweiger, A. & Jeschke, G. *Principles of pulse electron paramagnetic resonance* (Oxford University Press on Demand, 2001).

51. Neugebauer, P., Bloos, D., Marx, R., Lutz, P., Kern, M., Aguilà, D., Vaverka, J., Laguta, O., Dietrich, C., Clérac, R. & van Slageren, J. Ultra-broadband EPR spectroscopy in field and frequency domains. *Phys. Chem. Chem. Phys.* **20,** 15528–15534. doi:10.1039/C7CP07443C (22 2018).

52. Sojka, A., Šedivý, M., Laguta, O., Marko, A., Santana, V. T. & Neugebauer, P. in *Electron Paramagnetic Resonance: Volume 27* 214–252 (The Royal Society of Chemistry, 2021). ISBN: 978-1-83916-171-1. doi:10.1039/9781839162534-00214.

53. Algasinger, M., Paye, J., Werner, F., Schmidt, J., Brandt, M. S., Stutzmann, M. & Koynov, S. Improved Black Silicon for Photovoltaic Applications. *Advanced Energy Materials* **3,** 1068–1074. doi:https://doi.org/10.1002/aenm.201201038. eprint: https://onlinelibrary.wiley.com/doi/pdf/10.1002/aenm.201201038 (2013).

54. Abragam, A. & Bleaney, B. *Electron Paramagnetic Resonance of Transition Ions* ISBN: 9780198512509 (Clarendon P., 1970).

55. Queisser, H., Spaeth, J. & Overhof, H. *Point Defects in Semiconductors and Insulators: Determination of Atomic and Electronic Structure from Paramagnetic Hyperfine Interactions* ISBN: 9783642556166 (Springer Berlin Heidelberg, 2012).

56. Murphy, D. M. in *Metal Oxide Catalysis* 1–50 (John Wiley & Sons, Ltd, 2008). doi:https://doi.org/10.1002/9783527626113.ch1. eprint: https://onlinelibrary.wiley.com/doi/pdf/10.1002/9783527626113.ch1.

57. Abraham, R. J., Fisher, J. & Loftus, P. *Introduction to NMR spectroscopy* (Wiley New York, 1998).

58. Zavoisky, E. Spin-magnetic resonance in paramagnetics. *J. Phys. USSR* **3,** 211–245 (1945).

59. Lancaster, G. Electron Paramagnetic Resonance (A Review). *JOURNAL OF MATERIALS SCIENCE* **2,** 489–495. ISSN: 0022-2461. doi:10.1007/BF00562955 (1967).

60. HANEMAN, D. REVIEW OF ELECTRON-PARAMAGNETIC RESONANCE INVESTIGATIONS OF SEMICONDUCTOR SURFACES. *JAPANESE JOURNAL OF APPLIED PHYSICS,* 371–380. ISSN: 0021-4922 (1974).

61. Salikhov, K. M. Electron paramagnetic resonance applications: promising developments at the E K Zavoisky Kazan Physical-Technical Institute of the Russian Academy of Sciences. *PHYSICS-USPEKHI* **59,** 588–594. ISSN: 1063-7869. doi:10.3367/UFNe.2016.02.037760 (2016).

62. Van Slageren, J. in *EPR SPECTROSCOPY: APPLICATIONS IN CHEMISTRY AND BIOLOGY* (eds Drescher, M. & Jeschke, G.) 199–234 (2012). doi:10.1007/128_2011_303.

63. Getzlaff, M. *Fundamentals of magnetism* (Springer Science & Business Media, 2007).

64. Morrish, A. H. *The physical principles of magnetism* (2001).

65. Lenahan, P. M. & Dressendorfer, P. V. Hole traps and trivalent silicon centers in metal/oxide/silicon devices. *Journal of Applied Physics* **55,** 3495–3499. ISSN: 0021-8979. doi:10.1063/1.332937 (10 1984).

66. Feigl, F. J., Fowler, W. & Yip, K. L. Oxygen vacancy model for the E_1' center in SiO_2. *Solid State Communications* **14,** 225–229. ISSN: 0038-1098. doi:https://doi.org/10.1016/0038-1098(74)90840-0 (1974).

67. Lenahan, P., Mele, J., Conley, J., Lowry, R. & Woodbury, D. Predicting radiation response from process parameters: Verification of a physically based predictive model. *IEEE Transactions on Nuclear Science* **46,** 1534–1543. doi:10.1109/23.819118 (1999).

68. Spaeth, J.-M. & Overhof, H. in *Point Defects in Semiconductors and Insulators: Determination of Atomic and Electronic Structure from Paramagnetic Hyperfine Interactions* 265–308 (Springer Berlin Heidelberg, Berlin, Heidelberg, 2003). ISBN: 978-3-642-55615-9. doi:10.1007/978-3-642-55615-9_7.

69. Boehme, C. & Malissa, H. in *eMagRes* 83–100 (John Wiley & Sons, Ltd, 2017). ISBN: 9780470034590. doi:https://doi.org/10.1002/9780470034590.emrstm1525. eprint: https://onlinelibrary.wiley.com/doi/pdf/10.1002/9780470034590.emrstm1525.

70. Graeff, C., Kawachi, G., Brandt, M., Stutzmann, M. & Powell, M. Spin-dependent transport in amorphous silicon thin-film transistors. *Journal of Non-Crystalline Solids* **198-200,** 1117–1120. ISSN: 00223093. doi:10.1016/0022-3093(96)00059-2 (1996).

71. Lepine, D. J. Spin-Dependent Recombination on Silicon Surface. *Phys. Rev. B* **6,** 436–441. doi:10.1103/PhysRevB.6.436 (2 1972).

72. Kaplan, D., Solomon, I. & Mott, N.F. Explanation of the large spin-dependent recombination effect in semiconductors. *J. Physique Lett.* **39,** 51–54. doi:10.1051/jphyslet:0197800390405100 (1978).

73. Stich, B., Greulich-Weber, S. & Spaeth, J.-M. Electrical detection of electron paramagnetic resonance: New possibilities for the study of point defects. *Journal of Applied Physics* **77,** 1546–1553. doi:10.1063/1.358906. eprint: https://doi.org/10.1063/1.358906 (1995).

74. Rong, F., Buchwald, W., Poindexter, E., Warren, W. & Keeble, D. Spin-dependent Shockley-read recombination of electrons and holes in indirect-band-gap semiconductor p-n junction diodes. *Solid-State Electronics* **34,** 835–841. ISSN: 0038-1101. doi:https://doi.org/10.1016/0038-1101(91)90229-R (1991).

75. Kamimura, H. & F. Mott, N. The Variable Range Hopping Induced by Electron Spin Resonance in n-Type Silicon and Germanium. *Journal of the Physical Society of Japan* **40,** 1351–1358. doi:10.1143/JPSJ.40.1351. eprint: https://doi.org/10.1143/JPSJ.40.1351 (1976).

76. Kishimoto, N. & Morigaki, K. Resistivity Decrease Due to Electron Spin Resonance in the Metallic Region of Heavily Phosphorus-Doped Silicon. *Journal of the Physical Society of Japan* **42,** 137–145. doi:10.1143/JPSJ.42.137. eprint: https://doi.org/10.1143/JPSJ.42.137 (1977).

77. Boehme, C. & Lips, K. Theory of time-domain measurement of spin-dependent recombination with pulsed electrically detected magnetic resonance. *PHYSICAL REVIEW B* **68.** ISSN: 1098-0121. doi:10.1103/PhysRevB.68.245105 (2003).

78. Tennahewa, T. H., Hosseinzadeh, S., Atwood, S. I., Popli, H., Malissa, H., Lupton, J. M. & Boehme, C. *Spin relaxation dynamics of radical-pair processes at low magnetic fields* 2022. doi:10.48550/ARXIV.2207.07086.

79. Hoehne, F., Dreher, L., Suckert, M., Franke, D. P., Stutzmann, M. & Brandt, M. S. Time constants of spin-dependent recombination processes. *PHYSICAL REVIEW B* **88.** ISSN: 1098-0121. doi:10.1103/PhysRevB.88.155301 (2013).

80. Franke, D. P., Hoehne, F., Vlasenko, L. S., Itoh, K. M. & Brandt, M. S. Spin-dependent recombination involving oxygen-vacancy complexes in silicon. *PHYSICAL REVIEW B* **89.** ISSN: 2469-9950. doi:10.1103/PhysRevB.89.195207 (2014).

81. Dreher, L., Hoehne, F., Morishita, H., Huebl, H., Stutzmann, M., Itoh, K. M. & Brandt, M. S. Pulsed low-field electrically detected magnetic resonance. *PHYSICAL REVIEW B* **91.** ISSN: 1098-0121. doi:10.1103/PhysRevB.91.075314 (2015).

82. Suzuki, T. Simultaneous detection of electrically detected magnetic resonance and electron spin resonance using composite modulation. *Review of Scientific Instruments* **90,** 073102. doi:10.1063/1.5093215. eprint: https://doi.org/10.1063/1.5093215 (2019).

83. Cochrane, C. J. & Lenahan, P. M. *A Means to Study Reliability Based Defects in Fully Processed Devices Utilizing Zero-Field Spin Dependent Transport* in *2012 IEEE INTERNATIONAL INTEGRATED RELIABILITY WORKSHOP FINAL REPORT* IEEE International Integrated Reliability Workshop (IIRW), S Lake Tahoe, CA, OCT 14-18, 2012 (2012), 45–47.

84. Cochrane, C. J. & Lenahan, P. M. Zero-field detection of spin dependent recombination with direct observation of electron nuclear hyperfine interactions in the absence of an oscillating electromagnetic field. *JOURNAL OF APPLIED PHYSICS* **112.** ISSN: 0021-8979. doi:10.1063/1.4770472 (2012).

85. Cochrane, C. J. & Lenahan, P. M. *Zero/low field SDR and SDT used for atomic scale probes of NBTI and TDDB* in *2013 IEEE INTERNATIONAL INTEGRATED RELIABILITY WORKSHOP FINAL REPORT (IRW)* IEEE International Integrated Reliability Workshop (IIRW), South Lake Tahoe, CA, OCT 13-17, 2013 (2013), 88–89. ISBN: 978-1-4799-0350-4.

86. Cochrane, C. J. & Lenahan, P. M. Spin counting in electrically detected magnetic resonance via low-field defect state mixing. *APPLIED PHYSICS LETTERS* **104.** ISSN: 0003-6951. doi:10.1063/1.4867507 (2014).

87. Fukuda, K. & Asakawa, N. Development of multi-frequency ESR/EDMR system using a rectangular cavity equipped with waveguide window. *Review of Scientific Instruments* **87,** 113106. doi:10.1063/1.4967712. eprint: https://doi.org/10.1063/1.4967712 (2016).

88. Lang, V., Lo, C. C., George, R. E., Lyon, S. A., Bokor, J., Schenkel, T., Ardavan, A. & Morton, J. J. L. Electrically detected magnetic resonance in a W-band microwave cavity. *Review of Scientific Instruments* **82,** 034704. doi:10.1063/1.3557395. eprint: https://doi.org/10.1063/1.3557395 (2011).

89. McCrory, D. J., Anders, M. A., Ryan, J. T., Shrestha, P. R., Cheung, K. P., Lenahan, P. M. & Campbell, J. P. Wafer-Level Electrically Detected Magnetic Resonance: Magnetic Resonance in a Probing Station. *IEEE Transactions on Device and Materials Reliability* **18,** 139–143. doi:10.1109/TDMR.2018.2817341 (2018).

90. Ashton, J. P. & Lenahan, P. M. Multiple-photon transitions in electrically detected magnetic resonance measurements of 4H-SiC transistors. *Phys. Rev. B* **102,** 020101. doi:10.1103/PhysRevB.102.020101 (2 2020).

91. Sojka, A., Šedivý, M., Lagiň, A., Gabriš, A., Láznička, T., Santana, V. T., Laguta, O. & Neugebauer, P. Sample Holders for Sub-THz Electron Spin Resonance Spectroscopy. *IEEE Transactions on Instrumentation and Measurement* **71,** 1–12. doi:10.1109/TIM.2022.3164135 (2022).

92. Behrends, J., Schnegg, A., Fehr, M., Lambertz, A., Haas, S., Finger, F., Rech, B. & Lips, K. Electrical detection of electron spin resonance in microcrystalline silicon pin solar cells. English. *PHILOSOPHICAL MAGAZINE* **89,** 2655–2676. ISSN: 1478-6435. doi:10.1080/14786430903008472 (2009).

93. Behrends, J. *Spin-dependent transport and recombination in solar cells studied by pulsed electrically detected magnetic resonance* PhD thesis (2010), 53.

94. Smith, G. M., Lesurf, J. C. G., Mitchell, R. H. & Riedi, P. C. Quasi-optical cw mm-wave electron spin resonance spectrometer. *Review of Scientific Instruments* **69,** 3924–3937. doi:10.1063/1.1149200. eprint: https://doi.org/10.1063/1.1149200 (1998).

95. Grinberg, O. & Berliner, L. J. *Very High Frequency (VHF) ESR/EPR* (Springer Science & Business Media, 2013).

96. Van Tol, J., Brunel, L.-C. & Wylde, R. J. A quasioptical transient electron spin resonance spectrometer operating at 120 and 240 GHz. *Review of Scientific Instruments* **76,** 074101. doi:10.1063/1.1942533. eprint: https://doi.org/10.1063/1.1942533 (2005).

97. Barra, A. L., Hassan, A. K., Janoschka, A., Schmidt, C. L. & Schuenemann, V. Broad-band quasi-optical HF-EPR spectroscopy: Application to the study of the ferrous iron center from a rubredoxin mutant. *APPLIED MAGNETIC RESONANCE* **30,** 385–397. ISSN: 0937-9347. doi:10.1007/BF03166208 (2006).

98. Schnegg, A., Behrends, J., Lips, K., Bittl, R. & Holldack, K. Frequency domain Fourier transform THz-EPR on single molecule magnets using coherent synchrotron radiation. *PHYSICAL CHEMISTRY CHEMICAL PHYSICS* **11,** 6820–6825. ISSN: 1463-9076. doi:10.1039/b905745e (2009).

99. Dreiser, J., Schnegg, A., Holldack, K., Pedersen, K. S., Schau-Magnussen, M., Nehrkorn, J., Tregenna-Piggott, P., Mutka, H., Weihe, H., Bendix, J. & Waldmann, O. Frequency-Domain Fourier-Transform Terahertz Spectroscopy of the Single-Molecule Magnet (NEt4)[Mn-2(5-Brsalen)(2)(MeOH)(2)Cr(CN)(6)]. *CHEMISTRY-A EUROPEAN JOURNAL* **17,** 7492–7498. ISSN: 0947-6539. doi:10.1002/chem.201100581 (2011).

100. Telser, J., van Slageren, J., Vongtragool, S., Dressel, M., Reiff, W., Zvyagin, S., Ozarowski, A. & Krzystek, J. High-frequency/high-field EPR spectroscopy of the high-spin ferrous ion in hexaaqua complexes. *MAGNETIC RESONANCE IN CHEMISTRY* **43,** S130–S139. ISSN: 0749-1581. doi:10.1002/mrc.1689 (2005).

101. Vasin, A. V., Kalabukhova, E. N., Lukin, S. N., Savchenko, D. V., Lysenko, V. S., Nazarov, A. N., Rusavsky, A. V. & Koshka, Y. *High-frequency electron paramagnetic resonance study of the as deposited and annealed carbon-rich hydrogenated amorphous silicon-carbon films* in *SILICON CARBIDE 2008 - MATERIALS, PROCESSING AND DEVICES* (eds Dudley, M., Johnson, C., Powell, A. & Ryu, S.) **1069.** Conference on Silicon Carbide - Materials, Processing and Devices held at the 2008 MRS Spring Meeting, San Francisco, CA, MAR 25-27, 2008 (2008), 175+. ISBN: 978-1-60511-039-4.

102. Dinse, K.-P., van Tol, J., Ozarowski, A. & Corzilius, B. Multi-Frequency EPR and DC Conductivity of Itinerant Spins in Single-Wall Carbon Nanotubes. *APPLIED MAGNETIC RESONANCE* **37,** 595–603. ISSN: 0937-9347. doi:10.1007/s00723-009-0084-5 (2010).

103. Lang, V., Murphy, J. D., Falster, R. J. & Morton, J. J. L. Spin-dependent recombination in Czochralski silicon containing oxide precipitates. *Journal of Applied Physics* **111,** 013710. doi:10.1063/1.3675449. eprint: https://doi.org/10.1063/1.3675449 (2012).

104. Lo, C. C., Lang, V., George, R. E., Morton, J. J. L., Tyryshkin, A. M., Lyon, S. A., Bokor, J. & Schenkel, T. Electrically Detected Magnetic Resonance of Neutral Donors Interacting with a Two-Dimensional Electron Gas. *Phys. Rev. Lett.* **106,** 207601. doi:10.1103/PhysRevLett.106.207601 (20 2011).

105. Castro, F., Silva, G., Santos, L., Faria, R., Nüesch, F., Zuppiroli, L. & Graeff, C. Electrically detected magnetic resonance of organic and polymeric light emitting diodes. *Journal of Non-Crystalline Solids* **338-340.** Proceedings of the 20th International Conference on Amorphous and Microcrystalline Semiconductors, 622–625. ISSN: 0022-3093. doi:https://doi.org/10.1016/j.jnoncrysol.2004.03.055 (2004).

106. Goldsmith, P. F. in *Quasioptical Systems: Gaussian Beam Quasioptical Propogation and Applications* 187–228 (1998). doi:10.1109/9780470546291.ch8.

107. Neugebauer, P. *Development of Heterodyne High Field / High Frequency Electron Paramagnetic Resonance Spectrometer at 285 GHz* Theses (Université Joseph-Fourier - Grenoble I, 2010).

108. Grutzner, J. in *Encyclopedia of Analytical Science (Second Edition)* (eds Worsfold, P., Townshend, A. & Poole, C.) 2nd ed., 211–237 (Elsevier, Oxford, 2005). ISBN: 978-0-12-369397-6. doi:https://doi.org/10.1016/B0-12-369397-7/00405-2.

109. Dunsmore, J. P. *Handbook of microwave component measurements: with advanced VNA techniques* (John Wiley & Sons, 2020).

110. Trumbull, R. B., Yang, J.-S., Robinson, P. T., Di Pierro, S., Vennemann, T. & Wiedenbeck, M. The carbon isotope composition of natural SiC (moissanite) from the Earth's mantle: New discoveries from ophiolites. *LITHOS* **113,** 612–620. ISSN: 0024-4937. doi:10.1016/j.lithos.2009.06.033 (2009).

111. TAIROV, Y. GROWTH OF BULK SIC. *MATERIALS SCIENCE AND ENGINEERING B-SOLID STATE MATERIALS FOR ADVANCED TECHNOLOGY* **29.** European-Materials-Research-Society 1994 Spring Meeting, Symposium E; High Temperature Electronics - Materials, Devices and Applications, STRASBOURG, FRANCE, MAY 24-27, 1994, 83–89. ISSN: 0921-5107. doi:10.1016/0921-5107(94)04048-9 (1995).

112. Pons, M., Anikin, M., Chourou, K., Dedulle, J., Madar, R., Blanquet, E., Pisch, A., Bernard, C., Grosse, P., Faure, C., Basset, G. & Grange, Y. State of the art in the modelling of SiC sublimation growth. *MATERIALS SCIENCE AND ENGINEERING B-SOLID STATE MATERIALS FOR ADVANCED TECHNOLOGY* **61-2.** 2nd European Conference on Silicon Carbide and Related Materials (ECSCRM 98), MONTPELLIER, FRANCE, SEP 02-04, 1998, 18–28. ISSN: 0921-5107. doi:10.1016/S0921-5107(98)00439-5 (1999).

113. Liu, T., Xu, Z., Rommel, M., Wang, H., Song, Y., Wang, Y. & Fang, F. Raman Characterization of Carrier Concentrations of Al-implanted 4H-SiC with Low Carrier Concentration by Photo-Generated Carrier Effect. *Crystals* **9.** ISSN: 2073-4352. doi:10.3390/cryst9080428 (2019).

114. Bechstedt, F., Kackell, P., Zywietz, A., Karch, K., Adolph, B., Tenelsen, K. & Furthmuller, J. Polytypism and properties of silicon carbide. *PHYSICA STATUS SOLIDI B-BASIC SOLID STATE PHYSICS* **202,** 35–62. ISSN: 0370-1972. doi:10.1002/1521-3951(199707)202:1<35::AID-PSSB35>3.0.CO;2-8 (1997).

115. Cheung, R. *Silicon carbide microelectromechanical systems for harsh environments* (World Scientific, 2006).

116. WOZNIAK, K. & PAZIEWSKA, D. STUDIES ON PRODUCTION OF LIGHTNING-ROD SILICON-CARBIDE OF INCREASED ELECTROCONDUCTIVITY. *PRZEMYSL CHEMICZNY* **57,** 419–421. ISSN: 0033-2496 (1978).

117. Kashyap, A. S., Sandvik, P., McMahon, J., Bolotnikov, A., Erlbaum, J. & Andarawis, E. *Silicon Carbide Transient Voltage Suppressor for Next Generation Lightning Protection* in *2014 IEEE WORKSHOP ON WIDE BANDGAP POWER DEVICES AND APPLICATIONS (WIPDA)* IEEE Workshop on Wide Bandgap Power Devices and Applications (IEEE WiPDA), Knoxville, TN, OCT 13-15, 2014 (2014), 146–149. ISBN: 978-1-4799-5493-3.

118. Bergogne, D., Hammoud, A., Tournier, D., Buttay, C., Amieh, Y., Bevilacqua, P., Zaoui, A., Morel, H. & Allard, B. *Electro-thermal behaviour of a SiC JFET stressed by lightning-induced overvoltages* in *EPE: 2009 13TH EUROPEAN CONFERENCE ON POWER ELECTRONICS AND APPLICATIONS, VOLS 1-9* 13th European Conference on Power Electronics and Applications (EPE 2009), Barcelona, SPAIN, SEP 08-10, 2009 (2009), 2730–2737. ISBN: 978-1-4244-4432-8.

119. Casady, J. & Johnson, R. Status of silicon carbide (SiC) as a wide-bandgap semiconductor for high-temperature applications: A review. *SOLID-STATE ELECTRONICS* **39,** 1409–1422. ISSN: 0038-1101. doi:10.1016/0038-1101(96)00045-7 (1996).

120. Wang, Y., Bai, F., Jian, Y., Xu, C. & Wang, Z. Heat transfer enhancement of an electric air heating furnace by inserting silicon carbide ceramic foam panels. *EXPERIMENTAL THERMAL AND FLUID SCIENCE* **38,** 127–133. ISSN: 0894-1777. doi:10.1016/j.expthermflusci.2011.12.001 (2012).

121. Ozpineci, B., Chinthavali, M. & Tolbert, L. *A 55 kW three-phase automotive traction inverter with SIC schottky diodes* in *2005 IEEE VEHICLE POWER AND PROPULSION CONFERENCE (VPPC)* IEEE Vehicle Power and Propulsion Conference (VPPC), Chicago, IL, SEP 07-09, 2005 (2005), 541–546. ISBN: 0-7803-9280-9. doi:10.1109/VPPC.2005.1554611.

122. Narumanchi, S., Mihalic, M., Kelly, K. & Eesley, G. *Thermal interface materials for power electronics applications* in *2008 11TH IEEE INTERSOCIETY CONFERENCE ON THERMAL AND THERMOMECHANICAL PHENOMENA IN ELECTRONIC SYSTEMS, VOLS 1-3* 11th Intersociety Conference on Thermal and Thermomechanical Phenomena in Electronic Systems, Orlando, FL, MAY 28-31, 2008 (2008), 395+. ISBN: 978-1-4244-1700-1. doi:10.1109/ITHERM.2008.4544297.

123. Katsis, D., Geil, B., Griffin, T., Koebke, G., Kaplan, S., Ovrebo, G. & Bayne, S. *Silicon carbide power semiconductor module development for a high temperature 10kW AC drive* in *CONFERENCE RECORD OF THE 2005 IEEE INDUSTRY APPLICATIONS CONFERENCE, VOLS 1-4* 40th Annual Meeting of the IEEE-Industry-Applications-Society, Hong Kong, PEOPLES R CHINA, OCT 02-06, 2005 (2005), 399–403. ISBN: 0-7803-9208-6.

124. Kimoto, T. Material science and device physics in SiC technology for high-voltage power devices. *JAPANESE JOURNAL OF APPLIED PHYSICS* **54.** ISSN: 0021-4922. doi:10.7567/JJAP.54.040103 (2015).

125. Johnson, B. C., Castelletto, S., Ohshima, T. & Umeda, T. *Fabrication Of Single Photon Centres In Silicon Carbide* in *2012 CONFERENCE ON OPTOELECTRONIC AND MICROELECTRONIC MATERIALS AND DEVICES (COMMAD 2012)* Conference on Optoelectronic and Microelectronic Materials and Devices (COMMAD), Univ Melbourne, Sch Phys, Melbourne, AUSTRALIA, DEC 11-14, 2012 (2012), 217+.

126. Widmann, M., Niethammer, M., Makino, T., Rendler, T., Lasse, S., Ohshima, T., Ul Hassan, J., Son, N. T., Lee, S.-Y. & Wrachtrup, J. Bright single photon sources in lateral silicon carbide light emitting diodes. *APPLIED PHYSICS LETTERS* **112.** ISSN: 0003-6951. doi:10.1063/1.5032291 (2018).

127. Radulaski, M., Widmann, M., Niethammer, M., Zhang, J. L., Lee, S.-Y., Rendler, T., Lagoudakis, K. G., Son, N. T., Janzen, E., Ohshima, T., Wrachtrup, J. & Vuckovic, J. Scalable Quantum Photonics with Single Color Centers in Silicon Carbide. *NANO LETTERS* **17,** 1782–1786. ISSN: 1530-6984. doi:10.1021/acs.nanolett.6b05102 (2017).

128. Tairov, Y. & Tsvetkov, V. Investigation of growth processes of ingots of silicon carbide single crystals. *Journal of Crystal Growth* **43,** 209–212. ISSN: 0022-0248. doi:https://doi.org/10.1016/0022-0248(78)90169-0 (1978).

129. Poole, C. P. & Farach, H. A. *Theory of Magnetic Resonance* 2nd ed. (Wiley-Interscience, New York, 1987).

130. Götz, W., Schöner, A., Pensl, G., Suttrop, W., Choyke, W. J., Stein, R. & Leibenzeder, S. Nitrogen donors in 4H-silicon carbide. *Journal of Applied Physics* **73,** 3332–3338. doi:10.1063/1.352983. eprint: https://doi.org/10.1063/1.352983 (1993).

131. Kalabukhova, E. N., Kabdin, N. N., Lukin, S. N., Mokhov, E. N. & Shanina, B. D. ESR spectra of nonequivalent nitrogen sites in 15R SiC. *Sov. Phys. Solid State* **31,** 378 (1989).

132. Savchenko, D., Kalabukhova, E., Shanina, B., Pöppl, A., Yukhymchuk, V., Lančok, J., Ubyivovk, E. & Mokhov, E. EPR, ESE, and pulsed ENDOR study of the nitrogen donors in 15R SiC grown under carbon-rich conditions. *physica status solidi (b)* **252,** 566–572. doi:https://doi.org/10.1002/pssb.201451452. eprint: https://onlinelibrary.wiley.com/doi/pdf/10.1002/pssb.201451452 (2015).

133. Umeda, T., Esaki, K., Kosugi, R., Fukuda, K., Ohshima, T., Morishita, N. & Isoya, J. Behavior of nitrogen atoms in SiC-SiO_2 interfaces studied by electrically detected magnetic resonance. *Applied Physics Letters* **99,** 142105. doi:10.1063/1.3644156. eprint: https://doi.org/10.1063/1.3644156 (2011).

134. Kalabukhova, E. N., Lukin, S., Savchenko, D., Mitchel, W., Greulich-Weber, S., Gerstmann, U., Pöppl, A., Hoentsch, J., Rauls, E., Rozentzveig, Y., Mokhov, E., Syväjärvi, M. & Yakimova, R. EPR, ESE and Pulsed ENDOR Study of Nitrogen Related Centers in 4H-SiC Wafers Grown by Different Technologies. *Materials Science Forum* **556-557,** 355–358. ISSN: 1662-9752. doi:10.4028/www.scientific.net/MSF.556-557.355 (2007).

135. Gerstmann, U., Rauls, E., Greulich-Weber, S., Kalabukhova, E. N., Savchenko, D., Pöppl, A. & Mauri, F. Nitrogen Donor Aggregation in 4H-SiC: g-Tensor Calculations. *Materials Science Forum* **556-557,** 391–394. ISSN: 1662-9752. doi:10.4028/www.scientific.net/MSF.556-557.391 (2007).

136. KALABUKHOVA, E., LUKIN, S., SHANINA, B., ARTAMONOV, L. & MOKHOV, E. HOPPING CONDUCTION EFFECTS IN THE ESR-SPECTRA OF HEAVILY NITROGEN-DOPED 4HSIC. Russian. *FIZIKA TVERDOGO TELA* **32,** 818–825. ISSN: 0367-3294 (1990).

137. Miller, A. & Abrahams, E. Impurity Conduction at Low Concentrations. *Phys. Rev.* **120,** 745–755. doi:10.1103/PhysRev.120.745 (3 1960).

138. Mott, N. *Conduction in non-crystalline materials* (1987).

139. Xu, W.-W., Xia, F., Chen, L., Wu, M., Gang, T. & Huang, Y. High-temperature mechanical and thermodynamic properties of silicon carbide polytypes. English. *JOURNAL OF ALLOYS AND COMPOUNDS* **768,** 722–732. ISSN: 0925-8388. doi:10.1016/j.jallcom.2018.07.299 (2018).

9. Author publications and outputs

Publications

1. **A. Solodovnyk**, D. Savchenko, O. Laguta and P. Neugebauer: Multifrequency Electrically Detected Magnetic Resonance Setup based on a sub-THz FraScan Spectrometer. Submitted to *IEEE Transactions on Instrumentation and Measurement*.

Conferences

1. 07/2021 – EUROMAR, virtual participation. – Poster contribution.
2. 11/2019 – 8th EFEPR School, Brno, Czech Republic. – Organiser and poster contribution.
3. 06/2019 – Magneto-optical and THz Spectroscopy conference, Masłonskie, Poland. – Oral presentation.
4. 05/2019 – SPP1601 Young Researchers Workshop, Munich, Germany. – Poster contribution.
5. 10/2018 – PETER (Plasmon Enhanced Terahertz Electron Paramagnetic Resonance) Summer School, Brno, Czech Republic. – Poster contribution.
6. 09/2018 – V International School for Young Scientists, Magnetic Resonance and Magnetic Phenomena in Chemical and Biological Physics. St. Petersburg, Russian Federation. – Poster and oral presentation.
7. 07/2018 – ICN+T in Brno, Czech Republic. – Poster contribution.

List of abbreviations

A/D	Analog/digital
BNC	Bayonet Neill–Concelman
BUT	Brno University of Technology
C	Cubic
CEITEC	Central European Institute of Technology
CW	Continuous wave
DC	Direct current
EDMR	Electrically detected magnetic resonance
EM	Electromagnetic
ENDOR	Electron nuclear double resonance
EPR	Electron paramagnetic resonance
FD EDMR	Frequency domain electrically detected magnetic resonance
FET	Field Effect Transistor
FFM EDMR	Frequency-field electrically detected magnetic resonance map
FFT	Fast Fourier transform
FTIR	Fourier-transform infrared spectroscopy
GPS	Global Positioning System
GSM	Global System for Mobile Communications
H	Hexagonal
HF EPR	High field / High frequency electron paramagnetic resonance
HFS	Hyperfine Structure

LIST OF ABBREVIATIONS

IDE	Interdigitated Electrodes
IV	Current/voltage
KSM	Kaplan-Solomon-Mott
m.w.	Microwave
MD EDMR	Magnetic field domain electrically detected magnetic resonance
MEH-PPV	Poly[2-methoxy-5-(2'-ethylhexyloxy)-1,4-phenylene vinylene]
MM	Multimodal
MOSFET	Metal Oxide Semiconductor Field Effect Transistor
MRI	Magnetic resonance imaging
NMR	Nuclear magnetic resonance
OLED	Organic Light-Emitting Diode
PCB	Printed circuit board
PEEK	Polyether ether ketone
PSD	Phase-sensitive detection
PTFE	Polytetrafluoroethylene
QO	Quasi-Optics
R	Rhombohedral
RADAR	Radio detection and ranging
RF	Radio frequency
SH	Sample Holder
SiC	Silicon Carbide
SMA	SubMiniature version A
SMM	Single molecule magnet
SNR	Signal-to-noise ratio
SRH	Shockley-Read-Hall
TE	Transverse Electric
UV	Ultraviolet

VNA	Vector Network Analyzer
VRH	Variable-range hopping
VTI	Variable temperature insert
Wi-Fi	Wireless Fidelity
ZFS	Zero-field splitting

Appendices

Appendix A: PCB for EDMR Sample Holder

The scheme of a printed circuit board is shown in Fig. 9.1.

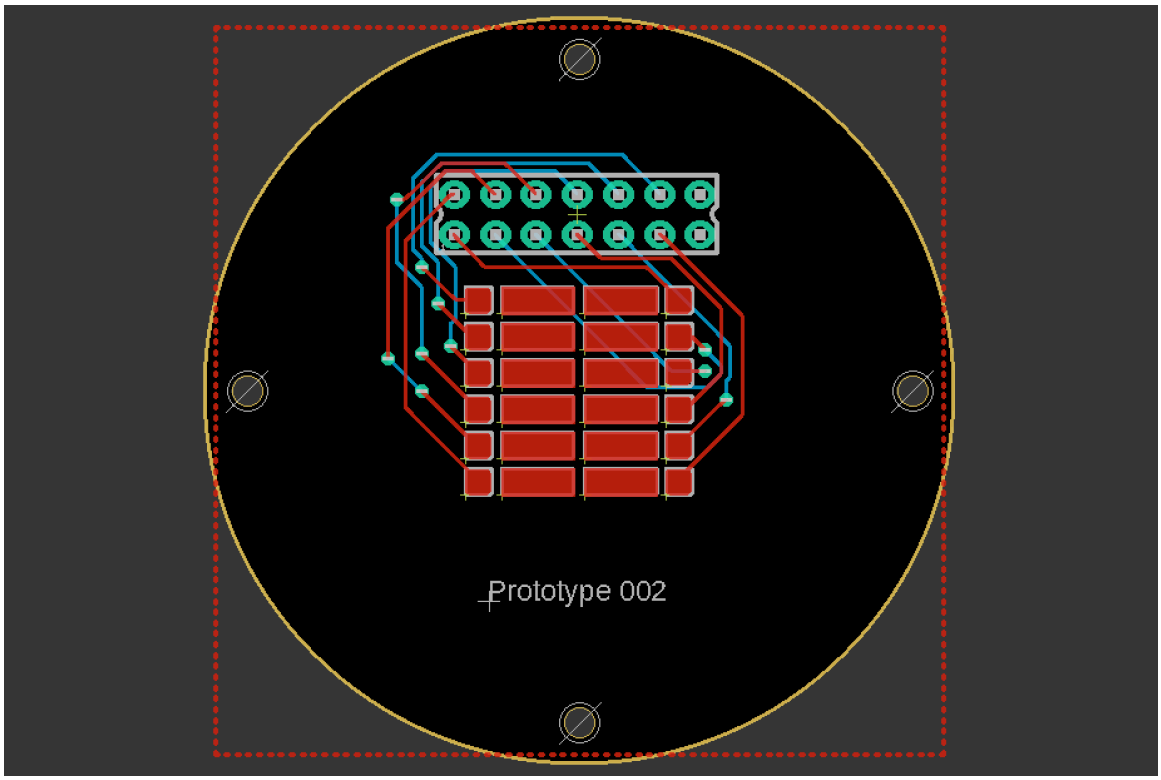

Figure 9.1: The outlay of the printed circuit board for the EDMR sample holder.

The circuit board contains precise dimensions and can be modified according to dedicated EDMR experiment. Taking into account the constrained dimensions, it is possible to rearrange the contact pads and change the signal terminal type. Eagle software (Autodesk, Inc., USA) was used to create the PCB, which has the capability to work with the components library. Consequently, when selecting the dedicated signal terminal from the components shop, the component's availability can be verified within the Eagle library or directly on the website of the component manufacturer. PCB fabrication was ordered at JLCPCB GmbH (Krefeld, Germany).

Appendix B: LabView program for the THz FraScan spectrometer operation for the MD measurements

Figure 9.2: The printscreen of the main tab of the LabView program, developed by Ing. Matúš Šedivý. See the text for the description.

In Fig. 9.2, the primary 'measurement' tab is presented. The window has input fields for the spectral data storage location and sample information (1). The second section (2) contains the experiment's controls. The timing of the experiment and additional real-time indications are detailed in section (3). The acquired spectra are displayed in section (4), where the signal channel (X, Y) can be selected. The script part (5) allows the experiment to be compiled with changing parameters for each subsequent MD scan. Section (6) depicts the temperature indications, which are read from the magnet, the VTI space, and the sample holder. Section (7) depicts the condition of the magnetic field. In the final part (8), the status of connected instrumentation is indicated.

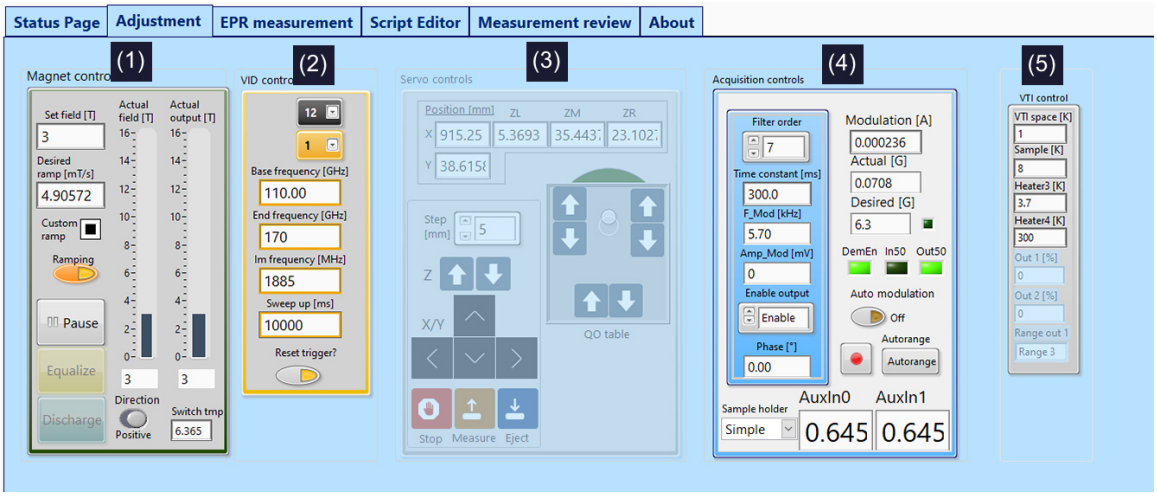

Figure 9.3: The printscreen of the settings tab of the LabView program. See the text for the description.

Fig. 9.3 depicts the cropped to main features 'adjustments' tab. The section (1) contains the magnetic field configurations. The specifications of the microwave source are depicted in section (2). The third section is responsible for adjusting the position of the moving table. The acquisition parameters section (4) sets the parameters for the lock-in amplifier and magnetic field modulation. The change in temperature of the VTI space within the magnet is attributable to section (5).